A Quantum Graph Approach to Metamaterial Design

by

Tristan M. Lawrie

Student Number: 20210167

Supervisor Name: Gregor Tanner

School: Mathematical Sciences

Year: 2024

A thesis submitted in partial fulfillment of the requirements for the degree of

Doctor of Philosophy

To my father...

Acknowledgements

I would not have been able to complete this thesis without the support and guidance of many individuals and institutions, to whom I will be eternally grateful. First and foremost, I wish to express my deepest gratitude to my supervisor, Professor Gregor Tanner, for his unwavering patience and care. From my worst days to my best, Gregor provided both stability and inspiration throughout my time at the University of Nottingham. He offered not only professional guidance through the scientific challenges that naturally arise during a PhD but also invaluable personal support through the many hurdles I encountered along the way. At every stage, Gregor stood by my side. Thank you.

I would also like to extend my heartfelt thanks to my co-supervisor, Professor Dimitrios Chronopoulos, for his guidance and constructive feedback in the early stages of my PhD, and to Professor Stephen Creagh for his valuable input throughout the years. I am also deeply grateful to Professor Gabriele Gradoni, who consistently made a special effort to include me in research and conferences, both in Nottingham and internationally. I am greatly appreciative of the mentorship and collaboration provided by Professor Sven Gnutzmann and Professor Luke Bennetts. Finally, I would like to thank Professor Martin Richter, who has continually gone out of his way to involve me in the research group and has been a great friend throughout the years.

I extend my gratitude to the many institutions that have hosted and supported me throughout my PhD, including the Isaac Newton Institute at the University of Cambridge, the London Mathematical Society at the University of Bath, The Metamaterials Network at the University of Exeter, the University of Bristol, the University of Otago, the University of Adelaide, Macquarie University, the University of Newcastle, and ENSTA University Paris.

Special thanks go to the University of Nottingham and the University of Adelaide

for their financial support through the Adelaide-Nottingham Alliance, which funded our research on wave energy harvesting. I am also grateful to the Defence Science and Technology Laboratory for supporting our work on the inverse design of metamaterials using quantum graph theory. I am particularly thankful to the RISE-6G research group for their financial backing and for including me in the AT-AP-RASC conference in Gran Canaria and the RISE-6G conference at the University of Cambridge.

On a personal note, I would like to thank my family and friends. Throughout my life, my father has been my hero, always encouraging me to pursue science with passion. Your love and support have made all of this possible. To my stepmother, I remember when I was 15, you told me I should become a scientist—thank you; this thesis is a testament to your encouragement. To my darling Megan, you have given me love and support every day, even when I didn't deserve it. This is as much your success as it is mine; I love you. Finally, I am deeply grateful to the doctors and nurses at the Queen's Medical Centre, whose names I cannot remember, and to Alex Medcalf for her care and support during my recovery. Without all of you, I would not be here to write this thesis.

Above all else, I give thanks to the Lord Jesus Christ, King of Kings. I pray, dear reader, he guides you through whatever battle you are facing.

This is My command:

be strong and courageous.

Never be afraid or discouraged,

I will remain with you

wherever you go.

Joshua 1:9

Publication List

- Lawrie, T., Tanner, G. and Chronopoulos, D., 2022. A quantum graph approach to metamaterial design. Scientific Reports, 12(1), p.18006.
- Lawrie, T., Gnutzmann, S. and Tanner, G., 2023. Closed form expressions for the Green's function of a quantum graph—a scattering approach. Journal of Physics A: Mathematical and Theoretical, 56(47), p.475202.
- Lawrie, T., Tanner, G. and Chaplain, G.J., 2023. Engineering Metamaterial Interface Scattering Coefficients via Quantum Graph Theory. Acta Physica Polonica: A, 144(6).
- Lawrie, T., Starkey, T.A., Tanner, G., Moore, D.B., Savage, P. and Chaplain, G.J., 2024. Application of quantum graph theory to metamaterial design: Negative refraction of acoustic waveguide modes. Physical Review Materials, 8(10), p.105201.
- Lawrie, T., Tanner, G. and Chaplain, G., 2024. A Non-diffracting Resonant Angular Filter. arXiv preprint arXiv:2410.17329.
- Wu, W., Malik, M.K., Cantero-Chinchilla, S., Lawrie, T., Yan, W.J., Tanner, G., Remenyte-Prescott, R. and Chronopoulos, D., 2022. Guided waves-based damage identification in plates through an inverse Bayesian process. Ultrasonics, 125, p.106773.
- Tian, Z., Bennett, J., Yang, J., Lawrie, T., Elmadih, W., Bardalai, A., Gerada, C., Zhu, J. and Chronopoulos, D., 2022. Experimental investigation of mechanical, acoustic and hybrid metamaterial designs for enhanced and multiband electric motor noise dissipation. Engineering Structures, 271, p.114945.
- Meng, H., Elmadih, W., Jiang, H., Lawrie, T., Chen, Y. and Chronopoulos, D., 2021. Broadband vibration attenuation achieved by additively manufactured

3D rainbow hollow sphere foams. Applied Physics Letters, 119(18).

Abstract

Since the turn of the century, metamaterials have garnered significant attention for their ability to exhibit exotic properties such as cloaking and perfect lensing. This has led to a growing need for reliable mathematical models capable of describing these materials' complex behaviors. While various modeling techniques exist for studying and engineering metamaterials, this thesis introduces a novel approach based on the scattering formalism of quantum graph theory. The flexibility and mathematical simplicity of this framework make it an ideal tool for designing metamaterials with unique band structures and for exploring complex multi-layer configurations. This thesis begins by extending quantum graph theory's scattering formalism to study wave propagation in complex periodic and finite quantum systems. Green's functions on quantum graphs are developed using a scattering approach, offering a powerful method for analyzing wave behavior on both closed and open graphs. Next, we apply this formalism to study acoustic metamaterials modeled as networks of interconnected waveguides, confirming the model's predictions through both simulations and experiments. Finally, the thesis explores the design of an angular Fourier filter using a periodic quantum graph with beyond-nearest-neighbor connections, demonstrating that quantum graphs can be used to model resonant wave transmission at discrete angles. The results were verified using COMSOL simulations in the acoustic regime, showing excellent agreement between theory, simulation, and experiment. This work establishes quantum graph theory as a new paradigm for metamaterial design, offering a versatile and intuitive framework for modeling wave behavior and guiding the development of future metamaterial technologies.

Contents

1 Introduction and Literature Review

This literature review begins by introducing the historical development of metamaterials, highlighting several key applications that have shaped the field. We will then explore various modeling techniques employed in metamaterial research, with a primary focus on lattice-based models, discussing their advantages and current limitations. With that as motivation, we will introduce the quantum graph theory literature, demonstrating how this field offers innovative approaches and potential advancements in the modeling and design of metamaterials.

1.1 Metamaterials

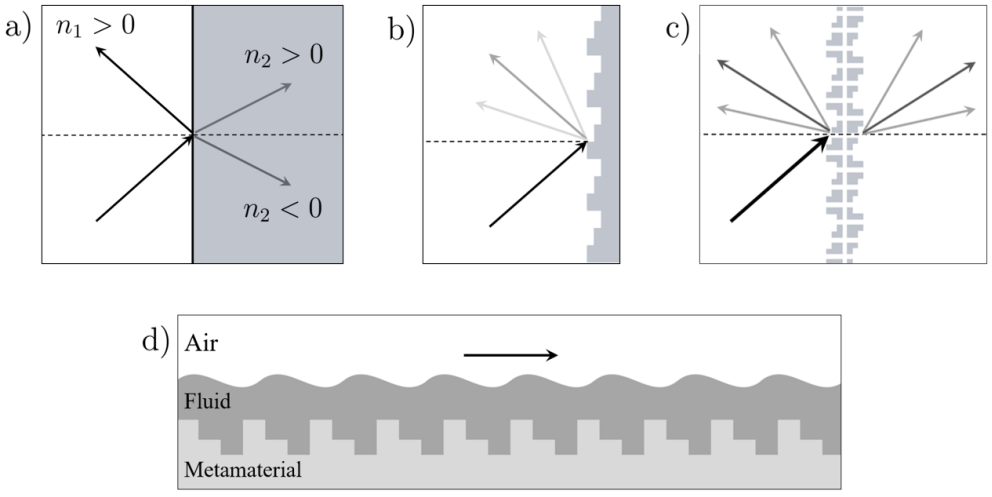

Figure 1: Illustration of different kinds of metamaterials. a) Illustrates how the choice of refractive index n_j between material 1 and 2 affects the transmission angle. b) Illustrates a reflective metasurface designed to reflect incident waves at custom angles. c) Illustrates a metamaterial filter, designed to reflect and transmit waves at custom angles. d) Illustrates a metamaterial applied to fluid mechanics, where the submerged metamaterial is designed to adjust the wave speed.

A metamaterial is an artificial structure engineered to exhibit unique and extraordinary physical properties, enabling precise control over electromagnetic and me-

chanical waves [1, 2, 3]. Its history began with Veselago's groundbreaking paper in 1968, where he investigated the wave properties of a material with simultaneously negative values of permeability and permittivity [4]. Such a material would possess a negative refractive index, resulting in electromagnetic waves having anti-parallel phase and group velocities. Consequently, Snell's law, the Doppler effect, and the Vavilov–Cherenkov effect are reversed. This change of refractive index is illustrated in Figure 1 a). These intriguing results were considered purely theoretical, as no such material was known to exist. That changed at the turn of the century when Pendry's revolutionary work demonstrated a practical application of such a "double negative" material. In his study [5], Pendry showed that a material with a negative refractive index in a medium with an equal and opposite index could perfectly focus light, overcoming the diffraction limit of traditional lenses. To realize such material properties, Pendry proposed a periodic arrangement of unit cells made from wires and C-shaped metal elements or "split-ring resonators" illustrated in Figure 2 a). This arrangement results in an effective negative refractive index over a certain frequency range. Smith later experimentally validated this [6], and the phenomenon has since been demonstrated in various domains [7, 8, 9, 10, 11].

Metamaterials function due to the interplay between the wavelength and the scale of the unit cell [2]. For wavelengths of the order of, or less than, that of the unit cell, the waves undergo Bragg scattering [12], interacting directly with each resonant element. However, in the long-wavelength regime, the material appears continuous, with properties owing to the underlying structure. These exotic wave effects arise from the structure's periodicity and the unit cell's resonant properties. Periodicity gives rise to spectral or band gaps, which have been extensively studied in photonic crystals [13, 14]. Band gaps represent frequencies at which energy propagation is forbidden. The presence of band gaps forces what would typically be high-frequency effects into the low-frequency regime, which can be utilized for controlling and manipulating light [15, 16, 17, 18, 19]. Additionally, the opening of band gaps can be

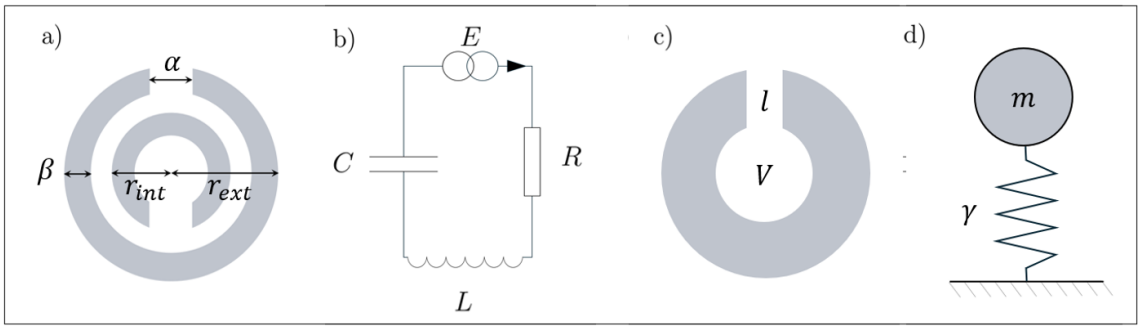

Figure 2: a) Illustrates a metallic split-ring resonator engineered to give negative μ at resonant frequencies. b) Illustrates the transmission line model equivalent with electrical parameters of Resistance R, inductance L, and capacitance C. c) Illustrates the acoustic Helmholtz resonator with internal volume V and neck length l. d) Illustrates the spring-mass equivalent with free parameters of mass m and spring constant γ.

achieved through the construction of subwavelength resonant elements [20] or phase modulators [21], which can be either active or passive [22, 21]. In the examples above, the resonant properties of the split-ring resonator depend on the gap width α and the dimensions of the rings β, r—illustrated in Figure 2 a). The capacitance of the resonator is determined by the gap width, while the inductance is determined by the radius and width of the rings, thus allowing one to tune the resonant frequency. An equivalent circuit design is illustrated in Figure 2 b). Naturally, there are a great number of alternative unit cells that can be designed, and these have found numerous applications in improved imaging resolution [23], communication across large distances [24], and complex environments [25, 26].

The presence of subwavelength resonant elements allows for a broad range of wave properties, even in non-periodic structures. Perhaps the most exotic proposed effect in the field of metamaterial research is cloaking or invisibility. Cloaking can be achieved using metamaterials by engineering material properties that bend electromagnetic waves around an object, rendering it undetectable at certain frequencies

[27]. Typical modeling techniques use transformation optics [28, 29, 30] to determine the material properties required at various locations within the cloak. This formulation applies across different wave regimes [31, 32].

Metamaterial research is not, however, restricted to electromagnetism. Due to the similarities in the governing equations that model wave transport in parallel fields, metamaterials have found numerous applications in acoustics [33, 34], elastodynamics [35, 36, 37], hydrodynamics [38], and quantum mechanics [39]. In acoustics and elastics, periodic metamaterials also exhibit spectral or band gaps [40, 41, 42, 43], as in phononic crystals [13]. The band gaps can be engineered through the presence of subwavelength resonant elements [44, 45] or unique scattering geometries [46, 47]. A commonly used example is the Helmholtz resonator illustrated in Figure 2 c), where the resonances are determined by a cavity of volume V connected by a channel of length l. The air within the cavity oscillates as if it were a mass and spring, as illustrated in Figure 2 d) with equivalent parameters of mass m and spring constant γ.

As in the electromagnetic case, the manipulation of these resonant elements can similarly give rise to a wide range of non-trivial wave effects, such as attenuation [48, 49], absorption [50, 51, 52, 53], damping [54], isolation [55], focusing [56, 57], self-collimation [58, 59], phase control [60], imaging [61, 62, 63], and detection [64].

In the context of elastic waves, the concept analogous to the negative refractive index found in optics is a negative effective mass. It is possible to design resonant unit cell configurations that give rise to negative effective mass over some frequency domain, as well as to engineer non-reciprocal wave propagation [65, 66]. A key application of this work is in seismic wave control [67]. Seismic metamaterials [68] and barriers [69] are designed to manipulate seismic waves, providing protection against earthquakes by directing or dampening incident waves. Various unit cell configurations have been investigated both theoretically [70, 71, 72, 73] and experimentally [35] in order to

redirect seismic energy. Similar to optics, the exotic property of wave cloaking can also be formulated and demonstrated in the acoustic and elastic regimes [74, 75, 76, 77], where this effect is achievable over a broad frequency range [75, 78, 79], as well as in different media [80, 81].

Much like engineering effective refractive index or mass, one can also engineer effective mechanical material properties, like the Poisson's ratio [82] and stiffness [83, 84]. Such mechanical metamaterials [85] are engineered to have unique properties under different loading conditions [86, 87, 88], for custom deformation, impact [51], and failure mechanisms [89, 90, 86].

Hydrodynamic metamaterials allow for the manipulation of water waves by building on principles from metamaterial and phononic crystal research. Both theoretical and experimental investigations, such as those conducted in [91], have demonstrated that non-trivial wave effects can be achieved through engineered structures submerged below the water surface, as illustrated in Figure 1 d). It has been shown that different submerged geometries, such as periodically structured ridges [92], pillars [93], partially or fully submerged boundaries [38, 94], and floating bodies [95], can give rise to an array of non-trivial wave effects. These engineered devices have allowed for negative refraction [38], and for custom reflective properties for applications in coastal protection [96], and energy harvesting through graded boundaries [94].

Outside of the domain of oscillatory wave equations, metamaterials have found applications in thermodynamics [97]. Thermal metamaterials are engineered to control and manipulate heat flow in ways that are not possible with natural materials. The manipulation of heat flow is achieved through engineered material compositions and geometries [98, 99]. One can determine the required material geometry through transformation thermodynamics [100, 101], as well as other methods [102], which can be used to achieve thermal cloaking both theoretically [103] and experimentally [97, 100]. Other applications include heat flux shielding and focusing [104, 102].

Metasurfaces, a category of metamaterials, are engineered to exhibit non-trivial scattering properties and are illustrated in Figure 1 b) and c). For an overview, see [105], and for a general formalism, see [106]. These structures have revolutionized wavefront manipulation, enabling precise control over reflection and transmission angles for various advanced applications. A few key functionalities include frequency-selective, absorbing, polarizing, beam-forming, and focusing surfaces, as well as allowing for holograms. Frequency-selective and absorbing surfaces [107] allow for the isolation or exclusion of waves in single or multiple frequency bands [108, 109, 110, 111, 112], across a wide range of angles [113, 114]. These functionalities are crucial for modern telecommunication systems [108, 115, 116, 25, 26, 21].

The ability of metasurfaces to create holograms and complex wavefronts was demonstrated by Ni et al. [117], showing potential applications in augmented reality and data storage. Reconfigurable and tunable metasurfaces, reviewed by Chen et al. [118], use materials like liquid crystals and MEMS to adapt to dynamic operational requirements, enhancing their utility in communication systems and adaptive optics. Additionally, acoustic metasurfaces utilizing coiled waveguides [33] expand the scope of metasurfaces into sound manipulation. In reflection-specific contexts, materials engineered for anomalous reflection [119] are critical for wireless communication through complex environments [21]. Emerging technologies, such as the Quantum Optimisation of reconfigurable Surfaces [25] and reconfigurable intelligent surfaces in wireless environments [26], underscore the transformative potential of metasurfaces in shaping the future of communication and signal processing.

Metasurfaces have also gained significant attention for their ability to manipulate electromagnetic waves, particularly in the context of transmission applications. These planar structures, composed of sub-wavelength-spaced elements, enable precise control over wavefronts by tailoring their optical transfer functions (OTFs). A key area of interest is the design of metasurfaces as Fourier filters, which selectively

transmit or block specific frequency components of an input signal, facilitating advanced signal processing tasks.

Fourier filters are indispensable in various domains, including optics, acoustics, and electronics, where they operate in the frequency domain to modify the spectral content of signals. Metasurfaces designed as Fourier filters utilize structured arrays of elements to achieve specific OTFs, enabling operations such as differentiation and integration. Davis et al. [120] demonstrated the use of metasurfaces with asymmetric OTFs for optical signal processing, highlighting their potential in performing complex mathematical operations on incident light. Similarly, Kildishev et al. [121] and Zhao et al. [122] discussed the advancements in planar photonics with metasurfaces, emphasizing their role in enhancing imaging systems and communication networks.

In optical communications, metamaterial Fourier filters play a crucial role by enabling selective transmission and filtering of optical signals, thereby improving network performance. Su et al. [123] discussed the fabrication and applications of optical metasurfaces, noting their ability to reduce signal degradation and enhance data integrity. The ability to dynamically tune metasurface responses, as reviewed by Zhang et al. [124], further broadens their applicability in reconfigurable and tunable systems. Silva et al. [125] illustrated the use of metamaterials for performing mathematical operations, including optical computation of the Laplace operator using phase-shifted Bragg gratings [126]. These capabilities are essential for developing adaptive optical filtering systems.

The field of metamaterials continues to advance rapidly, uncovering a wealth of complex phenomena and enabling innovative applications. Alongside this, advancements in precision manufacturing techniques, such as 3D printing, have facilitated the development of intricate designs tailored for specific functionalities, including vibration attenuation in 3D-printed structures [127, 128]. These developments un-

derscore the growing need for robust mathematical models capable of efficiently and accurately predicting wave transport in both natural and engineered materials. The following section explores various modelling techniques employed to analyse wave propagation in complex systems, with a particular focus on lattice-based structures.

1.2 Modelling Techniques

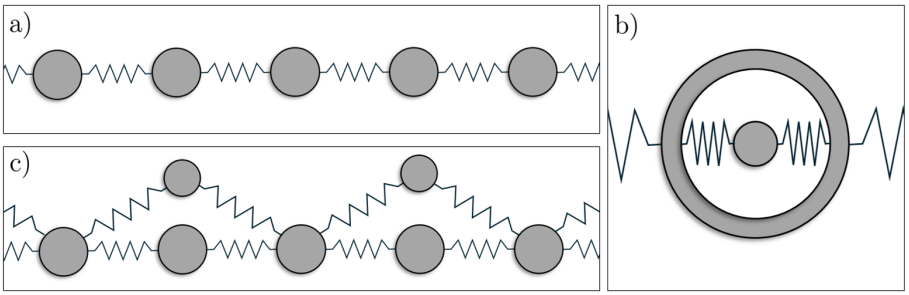

Figure 3: a) shows an array of masses coupled to their nearest neighbour by springs. b) shows an array of masses coupled both to their nearest neighbour as well as its beyond nearest neighbour via an additional mass. c) shows a hidden spring mass configuration within a given mass of an array that allows for resonant conditions.

Modeling periodic systems via lattices is exceptionally useful due to its mathematical simplicity and explanatory power - see [129] for an introduction and overview. Not only can lattices approximate a continuum in the long-wavelength regime as demonstrated by Kaplunov and Craster [130], but they also possess and allow for unique properties, such as flat bands [131], and configurations, such as beyond-nearest-neighbour connections [132, 133, 134, 135, 136, 137], which add additional degrees of freedom for potential metamaterial properties. Indeed, lattices have found a great number of applications in mechanical [138], elastodynamic, and acoustic research [139].

One of the first and most fundamental models in this context is the Kronig-Penney model, presented in 1931 [140]. This model describes the scattering of electrons in a one-dimensional periodic potential, allowing for the analysis of electronic band

structures in crystalline solids. By providing a simple yet powerful analytic formulation, the Kronig-Penney model enables researchers to gain intuitions about how the potential affects the wave properties of a lattice. This model can be used to engineer a lattice to exhibit a variety of properties by merely adjusting the periodic potential. A lattice version of the Kronig-Penney model was introduced by Exner in 1995 [141]. This approach, seen as an early version of periodic quantum graph theory, retains the simplicity of the original Kronig-Penney model while extending it to higher dimensions in a straightforward manner. This method overcomes some of the limitations of traditional scattering techniques and provides a powerful tool for understanding wave behavior in periodic systems.

Another significant lattice-based model is the spring-mass model [142], which describes a lattice of arbitrary dimension formed of masses coupled by springs. This model is particularly useful for studying mechanical waves in materials. It allows for a straightforward formulation to model a material's properties based on the chosen lattice topology, masses, and spring constants. The spring-mass model is extensively used in the study of metamaterials, especially in the contexts of acoustics and elasticity [143, 144]. By permitting multiple masses within a unit cell [145], this model can account for complex scattering effects, leading to resonant material characteristics [65, 66]. However, the spring-mass model has its shortcomings. Modeling open systems that can be excited externally is difficult without using Green's functions, leading to tedious mathematics when considering the scattering properties of interfaces between meshes or defects.

In the electromagnetic regime, the transmission line model [146] offers a different approach. This model describes wave scattering through transmission lines, which can be arranged to form a mesh in multiple dimensions. It is extensively used in microwave engineering and RF circuit design. The transmission line model allows for the modeling of material properties as a function of lattice topology and electrical

parameters such as resistance, inductance, and capacitance. Including resonant unit cell circuitry enables the study of non-trivial wave effects [147, 11, 148]. A key advantage of this model is its ability to model open systems through the introduction of leads, allowing for direct analytical expressions for scattering at boundaries and defects. However, the transmission line model is rooted in classical electromagnetism and is not easily applicable to acoustics or elasticity, limiting its utility in other areas of metamaterial study.

Finite element analysis (FEA) [149] is by far the most successful numerical technique for investigating the wave properties of materials and metamaterials [150]. FEA has been applied across a wide array of wave regimes, including acoustics, elasticity, and electromagnetism. The technique involves dividing a CAD structure into simple elements connected at nodes, forming a mesh. Each element is analysed using equations that describe its behavior in response to some forcing. The results from all elements are then assembled to approximate the overall response of the entire structure. FEA has proven to reproduce experimental results with great accuracy, with the precision of the model improving as the mesh is refined. However, FEA is computationally intensive and provides little to no mathematical intuition about the effects being computed.

Despite the strengths of numerical methods like FEA, there is a need to find a middle ground between analytical and numerical models. Researchers seek a model that is applicable to arbitrary scalar fields, mathematically simple in N-dimensions, and capable of studying open systems and analyzing non-trivial resonant elements and boundaries, while also being able to reproduce continuum solutions in some limit. For this, quantum graph theory offers a promising approach. Quantum graph theory uses the framework of graph theory to model quantum mechanical systems, providing a way to bridge the gap between discrete and continuous models and offering insights into the wave behavior of complex and periodic systems in a mathematically

tractable manner.

1.3 Quantum Graph Theory

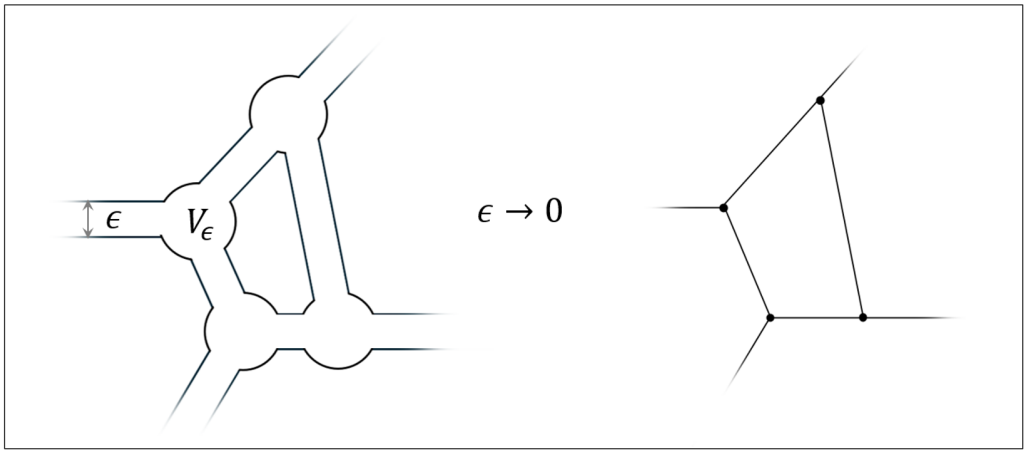

Figure 4: Illustrates how a network of thin channels of width ϵ, connected by junctions of volume V_ϵ converge to a simple graph structure in the thin channel limit.

Quantum graphs, defined as metric graphs endowed with differential operators, have a long history in mathematics, physics, and both theoretical chemistry and biology [151, 152, 153, 154, 155, 156, 157, 158]. The theory describes networks constructed from vertices connected by one-dimensional edges (bonds), which allow for wave propagation [159]. This theory can be viewed as the limiting case of networks formed of channels, such as waveguides, where the differential operator on the manifold converges to the one-dimensional graph operator in the thin channel limit $\epsilon \to 0$ [160, 161, 162], as illustrated in Figure 4. This perspective is crucial for studying wave propagation in thin, often mesoscopic or nanoscale network domains [160]. Within such systems, wave transport on the network depends on the chosen topology, edge lengths or metric, and the choice of vertex matching conditions. In the case of thin channels connected by junctions, as shown in Figure 4, the vertex matching conditions depend on the volume V_ϵ, which models different matching conditions based on the rate of convergence, as shown in [163]. The most general vertex matching conditions were first derived by Kostrykin and Schrader

[164], with different vertex conditions leading to a variety of spectral properties [165, 166, 167, 168, 169, 170]. Typically, the metric is considered static; however, early work on graph solutions with time-varying edge lengths [171] offers promising avenues for diverse applications. The model's simplicity allows for a rigorous treatment of spectral theory topics usually related to the study of self-adjoint partial differential operators, as introduced in [172].

The theory has been applied to the study of waveguides, previously investigated in the acoustic setting by Adams, Craster, and Guenneau [173, 174] who analyzed Bloch waves in periodic multilayered acoustic waveguides, as well as quantum wires and cables [175, 176, 177]. The graph topology and junctions are carefully chosen to design devices with customizable group velocities [178] and quantum switching capabilities [179, 180]. Such proposed wave devices have been designed for customizable frequency transmission properties [181, 182, 166, 183] for a broad range of applications, including quantum computing [184, 185]. This was demonstrated for integrated photonic networks [186] and in the study of spectral control of network lasers [187, 188]. The theory has found applications in superconductivity in finite disordered networks [189, 190] and demonstrated Anderson localization [191, 192, 193, 194, 195]. Furthermore, the theory has been applied to quantum walks [196, 197], quantum search algorithms [198] and quantum chaos [199, 200]. Quantum chaos has been experimentally demonstrated in networks of microwave coaxial cables [201, 202, 203]. In Chemistry and Biology, the theory can be used to study nerve impulse transmission [158] and model various protein [204, 205] and molecular structures [206, 207]. Beyond operators that provide oscillatory wave solutions, quantum graphs have also been used to model heat flow in networks [208, 209].

The spectrum of finite [210] and infinite [211] periodic quantum graphs depends on the chosen lattice topology. Various lattice topologies have been investigated, including ladder [212], square periodic [213], hexagonal [214, 215, 216, 217], and Cairo

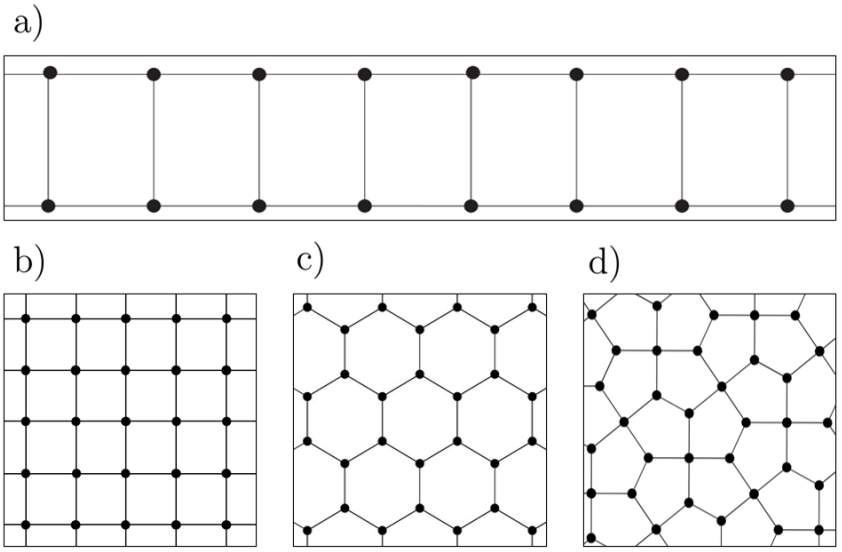

Figure 5: Illustrates four periodic graph structures. a) shows a ladder graph. b) shows a square periodic graph. c) shows a hexagonal periodic graph. d) shows a Cairo lattice graph.

lattices [218], which resemble the street tiling found in Cairo, Egypt. These different graph topologies are illustrated in Figure 5. Natural applications of spectral analysis of periodic structures can be found in photonic [219] and phononic crystals [220], as well as in the study of carbon nanotubes [206, 221]. The graphs' periodicity opens spectral or band gaps [222, 223], which can be manipulated by the choice of vertex matching conditions. This was previously investigated by Kuchment et al. [211], where vertex scattering conditions were made frequency-dependent by the "decoration" (attachment) of subgraphs. These decorations allowed for resonant conditions, much like the subwavelength resonant elements found in metamaterial research. Pavel et al. demonstrated that the spectrum of the graph Hamiltonian converges to the corresponding Schrödinger operator on Euclidean space in the continuum limit [224, 225], proving the lattice representation as an ideal model for studying wave transport in complex systems. This procedure was also applied to the heat equation [226].

A particular formalism of interest for this work is the scattering approach to quantum

graph theory, introduced by Kottos and Smilansky in 1997 [227]. In this approach, graph vertices are treated as point scatterers that map incident waves to outgoing waves on connected edges, from which stationary solutions (energy eigenstates) are constructed. One advantage of the scattering approach is that eigenvalue conditions can be written in terms of a secular equation involving the determinant of a unitary matrix of finite dimension N, where N typically equals twice the number of edges on the graph. Similarly, the scattering matrix of open quantum graphs can be given in terms of a closed-form expression involving finite-dimensional matrices of size N [228, 229]. This simplicity allows one to express the Green's function in a closed form [230], instead of a rather complicated sum over trajectories [229, 231].

Given the rich mathematical history and the broad array of applications, quantum graph theory stands out as an ideal model for studying metamaterials. The scattering approach, with its simplified eigenvalue conditions, further enhances the utility of quantum graph theory. The theory's flexibility in accommodating different topologies and vertex matching conditions allows for precise modeling of both finite and infinite periodic systems. This is particularly evident in its ability to manipulate spectral or band gaps through lattice topology and vertex matching conditions, with the inclusion of resonance, as is significant in its application to photonic and phononic crystals. With that, we propose a quantum graph approach to metamaterial design.

1.4 Thesis Structure

This thesis is structured as follows: Chapter 2 introduces the fundamentals of quantum graph theory, explaining how to construct quantum graphs and the role of boundary conditions in shaping wave propagation in finite closed, open, and infinite periodic quantum graphs. Chapter 3 presents a detailed exploration of Green's functions on quantum graphs, providing a framework for analysing wave behaviour

on both closed and open graph systems via a novel three-step procedure that allows the Green's function to be expressed in closed form. This formulation is then extended to a square periodic quantum graph, where the lattice Green's function for edge excitation is shown for the first time. Chapter 4 applies quantum graph theory to the modelling of metamaterials, demonstrating non-resonant negative refraction, which is then compared to both numerical simulations and experiment in the acoustic regime. Chapter 5 focuses on the design and analysis of Fourier filters using the scattering language of quantum graph theory, demonstrating the transmission properties of non-local vertex connections. Finally, Chapter 6 summarises the main findings of the thesis and highlights the potential for future work in quantum graph-based metamaterial design.

2 Constructing Quantum Graphs

To construct a quantum graph we first consider a metric graph $\mathcal{G}(\mathcal{V}, \mathcal{E}, L)$. Here, $\mathcal{E}$ is the set of edges, $\mathcal{V}$ the set of vertices, and $L = \{\ell_e : e \in \mathcal{E}\}$ is the graph metric containing a set of real positive edge lengths $\ell_e > 0$. Edges with finite length will be called bonds $\mathcal{B}$ and edges with infinite length will be called leads $\mathcal{L}$. Naturally, one may write the edge set as a union $\mathcal{E} = \mathcal{L} \cup \mathcal{B}$. With the number of leads being $N_{\mathcal{L}} = |\mathcal{L}|$ and the number of bonds being $N_{\mathcal{B}} = |\mathcal{B}|$, giving the total edge number as $N_{\mathcal{E}} = N_{\mathcal{B}} + N_{\mathcal{L}}$. For each bond $e \in \mathcal{B}$ we use a coordinate $z_e \in [0, \ell_e]$ with some arbitrary yet fixed choice of direction. Note the use of standard coordinate notation (x, y) is preserved for the Euclidean space the graph is embedded in which will be come relevant later. The graph coordinate defines a position on an edge such that $z_e = 0$ and $z_e = \ell_e$ correspond to the vertices connected by the bond. For a lead $e \in \mathcal{L}$ coordinates $z_e \in [0, \infty)$ are defined such that $z_e = 0$ corresponds to the vertex where the lead is attached. A point on the graph is a pair $\mathbf{z} = (e, z_e)$ of an edge and a coordinate.

The metric graph is turned into a quantum graph by the addition of a self-adjoint differential operator $\hat{H}$ together with a set of boundary conditions on the graph vertices. The self-adjointness in physical terms ensures conservation of the probability current at the vertex. For this we consider the Hilbert space $L^2(\mathcal{G}) \equiv \bigoplus_{e \in E} L^2([0, \ell_e])$ of square integrable complex-valued functions $\mathbf{\Phi}(\mathbf{z}) = \{\phi_e(z_e)\}_{e \in \mathcal{E}}$. The most frequently studied operators of interest act as follows:

The negative Laplacian,

$$\phi_e(z_e) \to -\frac{d^2}{dz_e^2}\phi_e(z_e), \tag{1}$$

the Schödinger operator

$$\phi_e(z_e) \to \left(-\frac{d^2}{dz_e^2} + V_e(z_e)\right)\phi_e(z_e), \tag{2}$$

the more general magnetic Schödinger operator

$$\phi_e(z_e) \to \left[\left(\frac{1}{i}\frac{d}{dz_e} - A_e(z_e)\right)^2 + V_e(z_e)\right]\phi_e(z_e). \tag{3}$$

Here $A_e(z_e)$ is the vector potential associated with an imposed magnetic field and $V_e(z_e)$ is the standard scalar potential. The operator is made complete by restricting the domain of the operator in Hilbert space to piecewise differentiable functions that satisfy matching conditions at each vertex v that preserve the self-adjointness of the operator. Put simply, we choose functions that are differentiable on each piece of the chosen domain.

The most general vertex matching conditions that preserve self-adjointness, and therefore energy flux, were first derived by Kostrykin and Schrader [164]. To briefly summarise their findings, let us define the set of edges attached to v as $\mathcal{S}^{(v)}$ that defines a star of degree (the number of connected edges) $d^{(v)}$, with $d^{(v)} = |\mathcal{S}^{(v)}|$. We consider the edge coordinate to be $z_e = 0$ for all $e \in \mathcal{S}^{(v)}$. Matching conditions at the vertex v may be written in the most general form by

$$\boldsymbol{A}^{(v)}\boldsymbol{\Phi}^{(v)}(0) + \boldsymbol{B}^{(v)}\boldsymbol{\Phi}^{(v)'}(0) = 0. \tag{4}$$

Where $\boldsymbol{\Phi}^{(v)}$ and $\boldsymbol{\Phi}^{(v)'}$ are the vectors of all square integrable complex-valued functions on the edges in $\mathcal{S}^{(v)}$ and its spacial derivative respectively. Note that the gradient is taken on each edge in the direction of increasing z_e, giving the e^{th} vector element $\left[\boldsymbol{\Phi}^{(v)'}\right]_e = d\phi_e(z_e)/dz_e$ for all $e \in \mathcal{S}^{(v)}$. Here $\boldsymbol{A}^{(v)}$ and $\boldsymbol{B}^{(v)}$ are two complex valued square matrices of dimension $d^{(v)}$ which preserve self-adjointness if and only if the two following conditions are satisfied:

1. *The set of equations need to be independent, resulting in the matrix* $\left(\boldsymbol{A}^{(v)}, \boldsymbol{B}^{(v)}\right)$ *having full rank.*

2. *The product* $\boldsymbol{A}^{(v)}\boldsymbol{B}^{(v)\dagger} = \boldsymbol{B}^{(v)}\boldsymbol{A}^{(v)\dagger}$ *is a hermitian matrix.*

Here the matrix $\left(\boldsymbol{A}^{(v)}, \boldsymbol{B}^{(v)}\right)$ is simply a rectangular $d^{(v)} \times 2d^{(v)}$ matrix formed by horizontally stacking $\boldsymbol{A}^{(v)}$ and $\boldsymbol{B}^{(v)}$.

The self-adjointness of the chosen operator implies a unitary evolution in time, such that $\boldsymbol{\Phi}(\mathbf{z}, t) = e^{-i\omega t}\boldsymbol{\Psi}(\mathbf{z})$ gives $|\boldsymbol{\Phi}(\mathbf{z}, t)|^2 = |\boldsymbol{\Psi}(\mathbf{z})|^2$. Here ω represents the real valued frequency and we choose the convention that it is strictly positive. From this the stationary solution satisfies the homogeneous eigen-problem

$$\left(\hat{H} - k^2\right)\boldsymbol{\Psi}(\mathbf{z}) = \mathbf{0} \ , \tag{5}$$

where k represents the wave number. The relationship between k and ω depends on the physical system being modelled. For quantum mechanics the time evolution is given by the operator $i\partial/\partial t$ with free space quadratic dispersion $k^2 \propto \omega$. While in classical mechanics the time evolution is given by the operator $\partial^2/\partial t^2$ with linear free space dispersion $k \propto \omega$. Note any dimensional constant is set to unity.

For this work we consider problems governed by the operator defined by the negative Laplacian as in equation (1), representing some arbitrary scalar field. This choice makes the formulation applicable to a broad class of problems, such as in acoustics, optics or indeed single particle quantum mechanics where $A_e(z_e) = V_e(z_e) = 0$. This choice of operator gives the governing equation of this work, as the Helmholtz wave equation,

$$\left[\left(\hat{H} - k^2\right)\boldsymbol{\Psi}(\mathbf{z})\right]_e = -\left(\frac{d^2}{dz_e^2} + k^2\right)\psi_e(z_e) = 0 \ . \tag{6}$$

The wave function is expressed as a superposition of counter propagating plane waves,

$$\begin{aligned}
\psi_e(z_e) =& a_{e_-}^{\text{in}} e^{-ikz_e} + a_{e_+}^{\text{out}} e^{ikz_e} \\
=& a_{e_-}^{\text{out}} e^{-ik(z_e - \ell_e)} + a_{e_+}^{\text{in}} e^{ik(z_e - \ell_e)} \\
=& a_{e_-}^{\text{in}} e^{-ikz_e} + a_{e_+}^{\text{in}} e^{ik(z_e - \ell_e)} \ .
\end{aligned} \tag{7}$$

Here, $a_{e\pm}^{\text{in/out}}$ is the complex wave amplitude on edge e propagating in the direction of increasing $(+)$ or decreasing $(-)$ z_e, heading in or out of a vertex. If e is a lead only the amplitudes $a_{e\pm}^{\text{in/out}}$ at $z_e = 0$ are used.

2.1 Vertex Scattering

The following scattering formalism was first introduced in 1997 [227] and describes how the vertex matching conditions can be expressed as a vertex scattering matrix $\boldsymbol{\Sigma}^{(v)}$ that performs the mapping,

$$\mathbf{a}^{(v),\text{out}} = \boldsymbol{\Sigma}^{(v)}\mathbf{a}^{(v),\text{in}} \tag{8}$$

Above $\mathbf{a}^{(v),\text{in/out}}$ are $d^{(v)}$ dimensional vectors that collect all incoming/outgoing amplitudes of plane waves on the edges $e \in \mathcal{S}^{(v)}$. By decomposing the wave function in (6) into counter propagating vectors of incoming and outgoing wave amplitudes as in (7), it is trivial to show the most general scattering matrix according to the matching conditions defined in (4) takes the form,

$$\boldsymbol{\Sigma}^{(v)}(k) = -\left(\boldsymbol{A}^{(v)} + ik\boldsymbol{B}^{(v)}\right)^{-1}\left(\boldsymbol{A}^{(v)} - ik\boldsymbol{B}^{(v)}\right). \tag{9}$$

For real k this is a well-defined unitary matrix due to the conditions on $\boldsymbol{A}^{(v)}$ and $\boldsymbol{B}^{(v)}$ which requires that $\boldsymbol{A}^{(v)} - ik\boldsymbol{B}^{(v)}$ is invertible. Note however that neither $\boldsymbol{A}^{(v)}$ nor $\boldsymbol{B}^{(v)}$ need to be invertible by themselves (in general neither is) and one needs to take care at for instance at $k = 0$ that it remains well defined in the limit.

2.1.1 Special Cases of Vertex Scattering

While one is free to define any scattering matrix at a vertex, provided the above conditions are met, we consider for this work a few special cases - namely Kirchhoff-Neumann, Dirichlet and δ-type boundary conditions, as outlined in [172]. For these

matching conditions the edge solutions must satisfy the following relations:

1. Kirchhoff-Neumann matching conditions

$$\psi_e(0) = \psi_{e'}(0) \quad \text{and} \quad \sum_{e \in \mathcal{S}^{(v)}} \frac{\partial \psi_e}{\partial z_e}(0) = 0 \tag{10}$$

2. Dirichlet matching conditions

$$\psi_e(0) = 0 \tag{11}$$

3. δ-type matching conditions

$$\psi_e(0) = \psi_{e'}(0) \quad \text{and} \quad \sum_{e \in \mathcal{S}^{(v)}} \frac{\partial \psi_e}{\partial z_e}(0) = \lambda^{(v)} \psi_{e'}(0). \tag{12}$$

To derive the scattering matrices of each of the conditions above, we consider the vertex of δ-type and choose the coupling parameter $\lambda^{(v)}$ appropriately to reproduce both Kirchhoff-Neumann and Dirichlet matching conditions. For this, consider the conditions in equation (12) and sum over the function on all $d^{(v)}$ edges in the star of the vertex,

$$\sum_{e \in \mathcal{S}^{(v)}} a_{e_+}^{out} + \sum_{e \in \mathcal{S}^{(v)}} a_{e_-}^{in} = d^{(v)} \psi_{e'}(0), \tag{13}$$

similarly, the same can be done for the derivative,

$$\sum_{e \in \mathcal{S}^{(v)}} a_{e_+}^{out} - \sum_{e \in \mathcal{S}^{(v)}} a_{e_-}^{in} = \frac{\lambda^{(v)}}{ik} \psi_{e'}(0). \tag{14}$$

By combining equation (13) and (14) we can solve for $\psi_{e'}(0)$ in terms of the incoming wave amplitudes,

$$\psi_{e'}(0) = \frac{2ik}{ikd^{(v)} - \lambda^{(v)}} \sum_{e \in \mathcal{S}^{(v)}} a_{e_-}^{in}, \tag{15}$$

which naturally leads to the outgoing solutions on an arbitrary edge e' being related to all other incoming wave amplitudes on e,

$$a^{out}_{e'_+} = \frac{2ik}{ikd^{(v)} - \lambda^{(v)}} \sum_{e \in \mathcal{S}^{(v)}} a^{in}_{e_-} - a^{in}_{e'_-}. \tag{16}$$

This gives $d^{(v)}$ simultaneous equations, which we use to construct the vertex scattering matrix,

$$\mathbf{\Sigma}^{(v)}(k) = \frac{2ik}{ikd^{(v)} - \lambda^{(v)}} \mathbb{E}_{d^{(v)}} - \mathbb{I}. \tag{17}$$

where $\mathbb{I}$ is the identity matrix and $\mathbb{E}_{d^{(v)}}$ is the matrix of dimension $d^{(v)}$ with all entries equal to one. By choice of $\lambda^{(v)}$, it is easy to arrive at the other scattering conditions given by (10) and (11),

$$\lambda^{(v)} = \begin{cases} 0, & \text{Neumann-Kirchhoff,} \\ \infty, & \text{Dirichlet.} \end{cases} \tag{18}$$

Notice that for Neumann-Kirchhoff matching conditions the k dependence drops out, and for Dirichlet matching conditions communication between the edges at the vertex is forbidden. The role that $\lambda^{(v)}$ plays in the scattering at a vertex is illustrated in several examples in Figure 6 a) - e).

Now that we have formulated the scattering condition at a single vertex, one may combine all vertex scattering matrices into a single (directed) edge scattering matrix $\mathbf{\Sigma}$, such that

$$\mathbf{a}^{\text{out}} = \mathbf{\Sigma}\, \mathbf{a}^{\text{in}}. \tag{19}$$

Here $\mathbf{a}^{\text{in/out}}$ is a $2N_B + N_L$ dimensional vector that collects all the incoming/outgoing amplitudes for all graph bonds and leads. The scattering matrix elements are expressed in terms of the individual vertex scattering matrices $\mathbf{\Sigma}^{(v)}$ such that (ordering

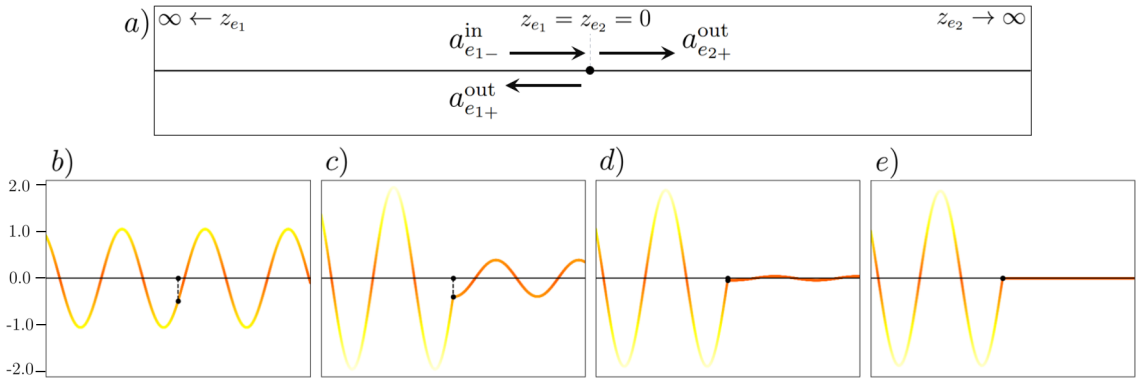

Figure 6: These diagrams illustrate the role of the parameter $\lambda^{(v_1)}$ in the scattering of waves at a given vertex as defined by equation 17. a) Shows the set up and illustrates a single vertex of degree 2, with both attached edges e_1 and e_2 being leads, with the choice of coordinate labelled. Additionally the incident wave $a^{\text{in}}_{e_{1-}}$ is labelled along with both the reflected and transmitted waves $a^{\text{out}}_{e_{1+}}$ and $a^{\text{out}}_{e_{2+}}$. b) Shows the resulting real component of the wave function for $\lambda^{(v_1)} = 0$, representing Kirchhoff-Neumann boundary conditions. c) $\lambda^{(v_1)} = 5$. d) $\lambda^{(v_1)} = 50$. Finally d) shows $\lambda^{(v_1)} = \infty$, representing Dirichlet boundary conditions.

the directed edges in appropriate way)

$$\mathbf{\Sigma} = \mathbf{\Pi} \begin{pmatrix} \mathbf{\Sigma}^{(1)} & 0 & \dots & 0 \\ 0 & \mathbf{\Sigma}^{(2)} & \dots & 0 \\ \vdots & \vdots & \ddots & \vdots \\ 0 & 0 & \dots & \mathbf{\Sigma}^{(N_{\mathcal{V}})} \end{pmatrix} = \mathbf{\Pi}\, \hat{\mathbf{\Sigma}} \tag{20}$$

Here, $\mathbf{\Pi}$ is a permutation matrix, that appropriately re-orders the diagonal scattering matrix to act correctly on the matrices stacked to form $\mathbf{a}^{\text{in/out}}$ in equation (19).

2.2 The Harmonics of a Finite Closed Quantum Graph

Having now understood and illustrated how waves scatter at a given vertex, the eigen-solutions of a closed or compact quantum graph are now derived. For this we

consider a graph formed of bonds only. In this case $\mathbf{a}^{\text{in/out}} \equiv \mathbf{a}_{\mathcal{B}}^{\text{in/out}}$, where $\mathbf{a}_{\mathcal{B}}^{\text{in/out}}$ is a vector of length $2N_{\mathcal{B}}$ that collects the wave amplitudes on every bond $\mathcal{B}$ of the graph. Naturally the bond wave amplitudes can be mapped to one another by the square $2N_B$ dimensional matrix $\mathbf{P}(k)$ that takes account of the phase difference between wave amplitudes across all bonds.

$$\mathbf{a}_{\mathcal{B}}^{\text{in}} = \mathbf{P}(k)\ \mathbf{a}_{\mathcal{B}}^{\text{out}}, \tag{21}$$

with matrix elements vv' given by the condition,

$$[\mathbf{P}(k)]_{vv'} = \begin{cases} e^{ik\ell_e}, & \text{if vertex } v \text{ and } v' \text{ are connected by edge } e, \\ 0, & \text{otherwise.} \end{cases} \tag{22}$$

The two relations (19) and (21) combine to give the $2N_{\mathcal{B}}$ dimensional quantum map $\mathbf{U}(k) = \mathbf{P}(k)\mathbf{\Sigma}(k)$ which performs the mapping,

$$\mathbf{a}_{\mathcal{B}}^{\text{in}} = \mathbf{U}(k)\ \mathbf{a}_{\mathcal{B}}^{\text{in}}. \tag{23}$$

Non-trivial solutions to (23) exist for wave numbers k for which the quantum map $\mathbf{U}$ has a unit eigenvalue, that is, for wave numbers that satisfy the secular equation

$$\xi(k) \equiv \det\left(\mathbb{I} - \mathbf{U}(k)\right) = 0\ . \tag{24}$$

The positive (discrete) spectrum of the quantum graph corresponds one-to-one to the zeros of $\xi(k_n)$ with $k_n > 0$ [227, 164]. The corresponding eigenstates can be obtained from (23) and (19). To understand this formalism better, let us consider a few simple examples.

2.2.1 Worked Example - The Interval Graph

Consider the simple problem of an interval graph $\mathcal{G}(\mathcal{V}, \mathcal{E}, L)$ formed of two vertices $\mathcal{V} = \{v_1, v_2\}$ with enforced Dirichlet boundary conditions, connected by a single edge $\mathcal{E} = \{e_1\}$ with metric $L = \{\ell_1\}$ - As illustrated in Figure 7.

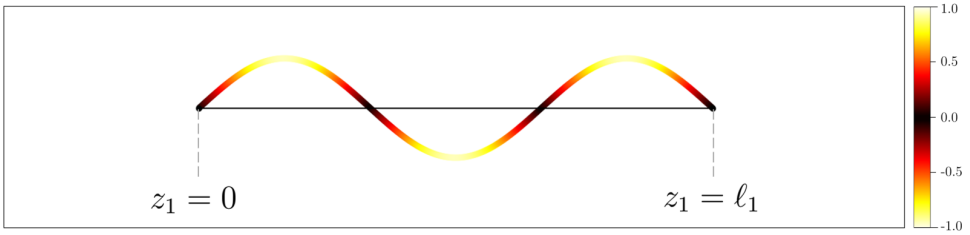

Figure 7: Shows a plot of the $n = 3$ eigen function solution of the interval graph with enforced Dirichlet boundary conditions at each vertex.

Here the edge propagation matrix, given by condition (22), takes the form

$$\boldsymbol{P}(k) = \begin{pmatrix} 0 & e^{ik\ell_1} \\ e^{ik\ell_1} & 0 \end{pmatrix}, \tag{25}$$

while the scattering matrix, defined in (17) with $\lambda^{(v_1)} = \lambda^{(v_2)} = \infty$ takes the form,

$$\boldsymbol{\Sigma} = \begin{pmatrix} -1 & 0 \\ 0 & -1 \end{pmatrix}. \tag{26}$$

By substitution of (25) and (26) into (24), it is trivial to show analytically that the eigen-solutions are given by

$$k_n = n\frac{2\pi}{\ell_1} \quad \text{for} \quad n \in \mathbb{N}, \tag{27}$$

with wave amplitudes given by determining the eigen vector of equation (23) - plotted in Figure 7.

2.2.2 Worked Example - A Star Graph

Consider now a star graph $\mathcal{G}(\mathcal{V}, \mathcal{E}, L)$ formed of four vertices $\mathcal{V} = \{v_1, v_2, v_3, v_4\}$ connected by three edges $\mathcal{E} = \{e_1, e_2, e_3\}$ with metric $L = \{\ell_1, \ell_2, \ell_3\}$. All three edges are connected at a central vertex v_1 with enforced Kirchhoff-Neumann boundary conditions, while all other vertices $v_{j\neq 1}$ have Dirichlet boundary conditions.

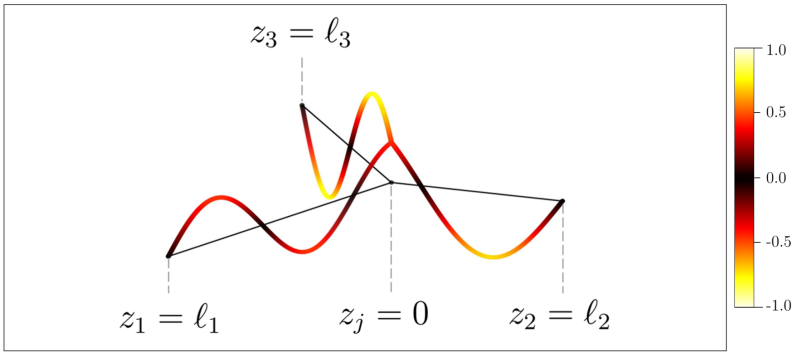

Figure 8: Shows a plot of the $n = 5$ eigen function solution of a compact star graph with enforced Dirichlet boundary conditions at the vertex of degree $d^{(v)} = 1$ and Kirchhoff-Neumann for $d^{(v)} = 3$.

Here the propagation matrix, as defined in (22), is given by

$$\boldsymbol{P}(k) = \begin{pmatrix} 0 & e^{ik\ell_1} & 0 & 0 & 0 & 0 \\ e^{ik\ell_1} & 0 & 0 & 0 & 0 & 0 \\ 0 & 0 & 0 & e^{ik\ell_2} & 0 & 0 \\ 0 & 0 & e^{ik\ell_2} & 0 & 0 & 0 \\ 0 & 0 & 0 & 0 & 0 & e^{ik\ell_3} \\ 0 & 0 & 0 & 0 & e^{ik\ell_3} & 0 \end{pmatrix}. \tag{28}$$

While the scattering matrix, defined in (17) for $\lambda^{(v_1)} = 0$ and $\lambda^{(v_{j\neq 1})} = \infty$, takes the

form,

$$\mathbf{\Sigma} = \begin{pmatrix} -\frac{1}{3} & 0 & \frac{2}{3} & 0 & \frac{2}{3} & 0 \\ 0 & -1 & 0 & 0 & 0 & 0 \\ \frac{2}{3} & 0 & -\frac{1}{3} & 0 & \frac{2}{3} & 0 \\ 0 & 0 & 0 & -1 & 0 & 0 \\ \frac{2}{3} & 0 & \frac{2}{3} & 0 & -\frac{1}{3} & 0 \\ 0 & 0 & 0 & 0 & 0 & -1 \end{pmatrix}. \tag{29}$$

By substitution of (28) and (29) into (24), the discrete set of solutions k_n can be determined by the zeros of $\xi(k_n) = 0$. This process is performed numerically with wave amplitudes given by solving (23) and plotted in Figure 8.

Let us now consider the continuous spectrum of solutions that exist for graphs that include leads, the so called open quantum graph.

2.3 The Spectrum of an Open Quantum Graph

Next let us consider the positive energy states for open quantum graphs. Generically these consist of an $N_{\mathcal{L}}$-fold degenerate continuum of scattering states. Physically the $N_{\mathcal{L}}$-fold degeneracy is obvious from the ability to choose $N_{\mathcal{L}}$ independent incoming plane waves along the leads. To describe the scattering states let us write the unitary edge scattering matrix in block form

$$\mathbf{\Sigma}(k) = \begin{pmatrix} \mathbf{\Sigma}(k)_{\mathcal{L}\mathcal{L}} & \mathbf{\Sigma}(k)_{\mathcal{L}\mathcal{B}} \\ \mathbf{\Sigma}(k)_{\mathcal{B}\mathcal{L}} & \mathbf{\Sigma}(k)_{\mathcal{B}\mathcal{B}} \end{pmatrix} = \begin{pmatrix} \mathbb{I} & 0 \\ 0 & \mathbf{\Pi} \end{pmatrix} \hat{\mathbf{\Sigma}}(k) \tag{30}$$

where the block-indices $\mathcal{B}$ and $\mathcal{L}$ refer to $2N_{\mathcal{B}}$ directed bonds and $N_{\mathcal{L}}$ leads. The second equality is expressed explicitly in terms of the matrix $\hat{\mathbf{\Sigma}}(k)$ defined in (20) which is formed of the block-diagonal arrangement of each vertex scattering matrix up to permutations defined by $\mathbf{\Pi}$ on all bond amplitudes. Let us also introduce the unitary quantum map for an open graph also expressed in block form

$$\mathbf{U}(k) \equiv \begin{pmatrix} \mathbf{U}(k)_{\mathcal{L}\mathcal{L}} & \mathbf{U}(k)_{\mathcal{L}\mathcal{B}} \\ \mathbf{U}(k)_{\mathcal{B}\mathcal{L}} & \mathbf{U}(k)_{\mathcal{B}\mathcal{B}} \end{pmatrix} = \begin{pmatrix} \mathbf{\Sigma}(k)_{\mathcal{L}\mathcal{L}} & \mathbf{\Sigma}(k)_{\mathcal{L}\mathcal{B}} \\ \mathbf{P}(k)\mathbf{\Sigma}(k)_{\mathcal{B}\mathcal{L}} & \mathbf{P}(k)\mathbf{\Sigma}(k)_{\mathcal{B}\mathcal{B}} \end{pmatrix} . \tag{31}$$

The scattering states are spanned by the N_L-dimensional vector $\mathbf{a}^{\text{in}}_{\mathcal{L}}$ of incoming plane wave amplitudes on the leads. The outgoing amplitudes $\mathbf{a}^{\text{out}}_{\mathcal{L}}$ and the incoming amplitudes on the directed bonds $\mathbf{a}^{\text{in}}_{\mathcal{B}}$ then result from solving the set of linear equations

$$\begin{pmatrix} \mathbf{a}(k)^{\text{out}}_{\mathcal{L}} \\ \mathbf{a}(k)^{\text{in}}_{\mathcal{B}} \end{pmatrix} = \begin{pmatrix} \mathbf{U}(k)_{\mathcal{L}\mathcal{L}} & \mathbf{U}(k)_{\mathcal{L}\mathcal{B}} \\ \mathbf{U}(k)_{\mathcal{B}\mathcal{L}} & \mathbf{U}(k)_{\mathcal{B}\mathcal{B}} \end{pmatrix} \begin{pmatrix} \mathbf{a}^{\text{in}}_{\mathcal{L}} \\ \mathbf{a}(k)^{\text{in}}_{\mathcal{B}} \end{pmatrix} \tag{32}$$

which follows again from (19) and (21). Solving these equations, one obtains for the outgoing amplitudes on the leads

$$\mathbf{a}(k)^{\text{out}}_{\mathcal{L}} = \boldsymbol{\sigma}(k)\mathbf{a}^{\text{in}}_{\mathcal{L}} \tag{33}$$

where the unitary graph scattering matrix is given as

$$\boldsymbol{\sigma}(k) = \mathbf{U}(k)_{\mathcal{LL}} + \mathbf{U}_{\mathcal{LB}} \left[\mathbb{I} - \mathbf{U}_{\mathcal{BB}}(k)\right]^{-1} \mathbf{U}(k)_{\mathcal{BL}} \ . \tag{34}$$

The plane wave amplitudes on the directed bonds can be expressed as

$$\mathbf{a}(k)_{\mathcal{B}}^{\text{in}} = \boldsymbol{\rho}(k)\mathbf{a}_{\mathcal{L}}^{\text{in}} \tag{35}$$

with the rectangular $2N_{\mathcal{B}} \times N_{\mathcal{L}}$ matrix

$$\boldsymbol{\rho}(k) = \left[\mathbb{I} - \mathbf{U}_{\mathcal{BB}}(k)\right]^{-1} \mathbf{U}(k)_{\mathcal{BL}} \ . \tag{36}$$

The scattering matrix $\boldsymbol{\sigma}(k)$ is related to the matrix $\boldsymbol{\rho}(k)$ via

$$\boldsymbol{\sigma}(k) = \mathbf{U}(k)_{\mathcal{LL}} + \mathbf{U}(k)_{\mathcal{LB}} \ \boldsymbol{\rho}(k) \ . \tag{37}$$

One may rightfully question whether the matrix $\mathbb{I} - \mathbf{U}(k)_{\mathcal{BB}}$ can always be inverted as required in equations (34) and (36). This is related to the existence of bound states in the continuum (a pure point spectrum in mathematical terms). In the absence of such bound states $\mathbf{U}(k)_{\mathcal{BB}}$ does not have a unit eigenvalue and the expression is valid for all wave numbers $k > 0$. We will return to the discussion of this expression in the presence of bound states, also known as perfect scars, later in section 3.3.1. For now we will consider some examples of the spectrum of open quantum graphs and comment on the instances where the matrix may not be well defined.

2.3.1 Worked Example - Open Star Graph

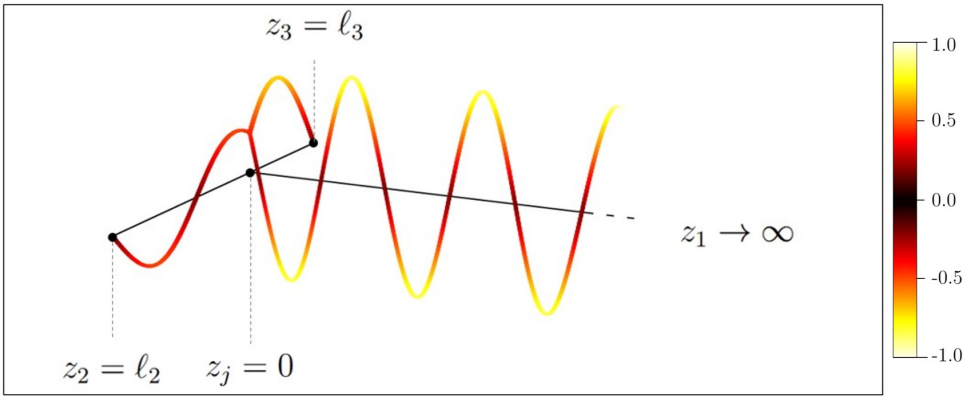

Figure 9: A 3-star with one lead consists of a central vertex v_1 connecting three edges $\mathcal{E} = \{e_1, e_2, e_3\}$. Here, e_1 is a lead and the other two edges $e_j \neq 1$ are bonds of lengths ℓ_2 and ℓ_3 ending at vertices v_2 and v_3.

Consider the quantum graph $\mathcal{G}(\mathcal{V}, \mathcal{E}, L)$ that represents an open T-junction as illustrates in Figure 9. Here there are three vertices $\mathcal{V} = \{v_1, v_2, v_3\}$ and three edges $\mathcal{E} = \{e_1, e_2, e_3\}$ with metric $L = \{\infty, \ell_2, \ell_3\}$. We choose the coordinates such that $z_j = 0$ for $j = 1, 2, 3$ at the central vertex v_1 with $z_j = \ell_j$ at vertices $v_j, j = 2, 3$. We enforce Kirchhoff-Neumann boundary conditions at the central vertex v_1 as defined by (17) for $\lambda^{(v_1)} = 0$ and Dirichlet boundary conditions for all other vertices, as defined by (17) for $\lambda^{(v_j)} = \infty$ for $j = 2, 3$. This graph has scattering properties defined by the quantum map,

$$\mathbf{U}(k) = \left(\begin{array}{c|cccc} -\frac{1}{3} & 0 & 0 & \frac{2}{3} & \frac{2}{3} \\ \hline \frac{2e^{ik\ell_2}}{3} & 0 & 0 & -\frac{e^{ik\ell_2}}{3} & \frac{2e^{ik\ell_2}}{3} \\ \frac{2e^{ik\ell_3}}{3} & 0 & 0 & \frac{2e^{ik\ell_3}}{3} & -\frac{e^{ik\ell_3}}{3} \\ 0 & -e^{ik\ell_2} & 0 & 0 & 0 \\ 0 & 0 & -e^{ik\ell_3} & 0 & 0 \end{array}\right) \equiv \begin{pmatrix} \mathbf{U}_{\mathcal{LL}} & \mathbf{U}_{\mathcal{LB}} \\ \mathbf{U}(k)_{\mathcal{BL}} & \mathbf{U}(k)_{\mathcal{BB}} \end{pmatrix}. \quad (38)$$

Computing the scattering matrix in the scattering approach require that one inverts the matrix $\mathbb{I} - \mathbf{U}(k)_{\mathcal{BB}}$ which is given as,

$$\frac{\mathbb{I}}{\mathbb{I} - \mathbf{U}(k)_{\mathcal{BB}}} = \frac{1}{D}\begin{pmatrix} 3 - e^{2ik\ell_3} & -2e^{ik(\ell_2+\ell_3)} & -(1+e^{2ik\ell_3})e^{ik\ell_2} & 2e^{ik\ell_2} \\ -2e^{ik(\ell_2+\ell_3)} & 3 - e^{2ik\ell_2} & 2e^{ik\ell_3} & -(1+e^{2ik\ell_2})e^{ik\ell_3} \\ -(3 - e^{2ik\ell_3})e^{ik\ell_2} & 2e^{ik(2\ell_2+\ell_3)} & 3 - e^{2ik\ell_3} & -2e^{2ik\ell_2} \\ 2e^{ik(\ell_2+2\ell_3)} & -(3 - e^{2ik\ell_2})e^{ik\ell_3} & -2e^{2ik\ell_3} & 3 - e^{2ik\ell_2} \end{pmatrix}, \tag{39}$$

where

$$D = 3 - e^{2ik\ell_2} - e^{2ik\ell_3} - e^{2ik(\ell_2+\ell_3)} \ . \tag{40}$$

Note that for $e^{2ik\ell_2} = e^{2ik\ell_3} = 1$, one has $D = 0$ making the inverse not well defined. This can only happen if the bond lengths are rationally related, then giving rise to a set of bound states in the continuum that vanish on the lead and are a sinusoidal wave along the two bonds with a node on the vertex v_1. The scattering states are then given by

$$\psi_{e_1}(z_1) = e^{-ikz_1} + \boldsymbol{\sigma}(k)e^{ikz_1}, \tag{41a}$$

$$\psi_{e_2}(z_2) = \boldsymbol{\rho}(k)_{2_+1}e^{ik(z_2-\ell_2)} + \boldsymbol{\rho}(k)_{2_-1}e^{-ikz_2} \tag{41b}$$

$$\psi_{e_3}(z_3) = \boldsymbol{\rho}(k)_{3_+1}e^{ik(z_3-\ell_3)} + \boldsymbol{\rho}(k)_{3_-1}e^{-ikz_3} \tag{41c}$$

where

$$\boldsymbol{\rho}(k) = \frac{\mathbb{I}}{\mathbb{I} - \mathbf{U}(k)_{\mathcal{BB}}}\mathbf{U}(k)_{\mathcal{BL}} = \frac{2}{D}\begin{pmatrix} e^{ik\ell_2}\left(1 - e^{2ik\ell_3}\right) \\ e^{ik\ell_3}\left(1 - e^{2ik\ell_2}\right) \\ -e^{2ik\ell_2}\left(1 - e^{2ik\ell_3}\right) \\ -e^{2ik\ell_3}\left(1 - e^{2ik\ell_2}\right) \end{pmatrix} \tag{42}$$

and

$$\boldsymbol{\sigma}(k) = \mathbf{U}_{\mathcal{L}\mathcal{L}} + \mathbf{U}_{\mathcal{L}\mathcal{B}}\boldsymbol{\rho}(k) = \frac{\bar{D}}{D}e^{2ik(\ell_2+\ell_3)} \ . \tag{43}$$

Where $\bar{D}$ represents the complex conjugate of D. Assuming the condition $D \neq 0$, the scattering states are then given as

$$\psi_{e_1}(z_1) = e^{-ikz_1} + \frac{\bar{D}}{D}e^{ik(z_1+2\ell_2+2\ell_3)}, \tag{44a}$$

$$\psi_{e_2}(z_2) = \frac{2(1-e^{2ik\ell_2})(1-e^{2ik\ell_3})}{D}\frac{\sin(k(\ell_2-z_2))}{\sin(k\ell_2)}, \tag{44b}$$

$$\psi_{e_3}(z_3) = \frac{2(1-e^{2ik\ell_2})(1-e^{2ik\ell_3})}{D}\frac{\sin(k(\ell_3-z_3))}{\sin(k\ell_3)} \ . \tag{44c}$$

These solutions are plotted in Figure 9. The scattering matrix is continuous due to $1 + \boldsymbol{\sigma}(k) = \frac{2(1-e^{2ik\ell_2})(1-e^{2ik\ell_3})}{D}$. It is straight forward to check that the scattering states also behave well near $e^{2ik\ell_2} = e^{2ik\ell_3} = 1$.

2.4 Spectrum of a Periodic Quantum Graph

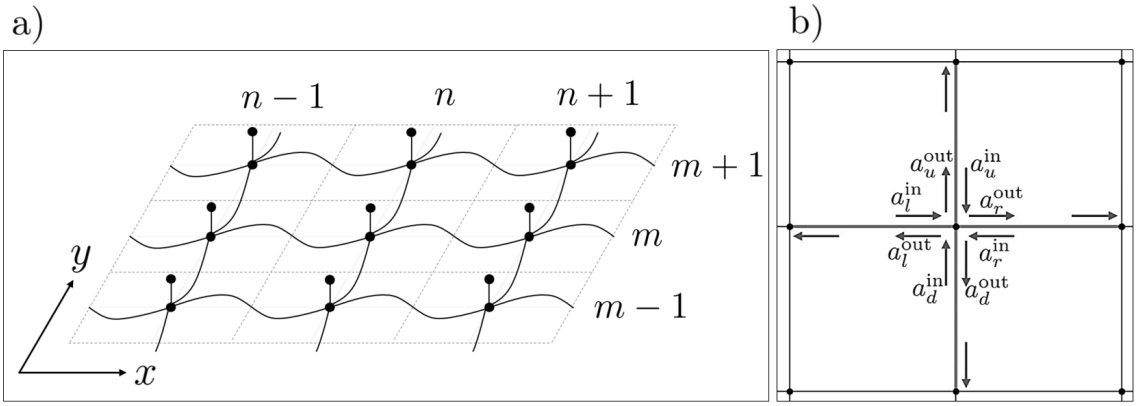

Figure 10: a) Illustrates a square periodic quantum graph, constructed of vertices connected by edges of variable length. The unit cell is further decorated by an additional sub-graph emerging out of the plane. b) Shows a top-down view of a given unit cell with the wave amplitudes $a_e^{\text{in/out}}$ illustrated around a given vertex.

In this section, we extend the theory of scattering on quantum graphs formulated in section 2.2 to include periodic quantum graphs. Consider an infinite square periodic arrangement of vertices embedded in a 2D Euclidean space with period ℓ. The space has horizontal and vertical continuous coordinates x and y, while the vertices are positioned on a discrete grid with coordinates n and m. Each vertex is connected to its neighboring vertices to the left (l), right (r), down (d), and up (u) by finite edges. Although the graph contains an infinite number of edges and vertices, we only concern ourselves with a finite set within the unit cell. Where the unit cell is the smallest repeating structure that forms the lattice.

Let us define the set of edges attached to a given vertex as $\mathcal{S} = \{l, r, d, u\}$, which forms the star of the vertex. The edges that make up this star are assigned the metric $\mathcal{L} = \{\ell_x, \ell_x, \ell_y, \ell_y\}$. Note that this metric does not necessarily equal the vertex period ℓ, allowing for space-coiled channels, as illustrated in Figure 10. For each edge $e \in \mathcal{S}$, we introduce an edge coordinate that exists within the domains $z_{nm,l} \in [0, \ell_x]$, $z_{nm,r} \in [0, \ell_x]$, $z_{nm,d} \in [0, \ell_y]$ and $z_{nm,u} \in [0, \ell_y]$, with $z_{nm,e} = 0$ at the vertex.

As before, we endow each edge with a differential operator, chosen to be the 1D Laplacian, leading to the Helmholtz wave equation:

$$\left(\frac{d^2}{dz_{nm,e}^2} + k^2\right)\psi_{nm,e}(z_{nm,e}) = 0. \tag{45}$$

Here, $\psi_{nm,e}$ is the wave function at vertex nm on edge e, which has a general solution as a superposition of counter-propagating plane waves:

$$\psi_{nm,e}(z_{nm,e}) = a_{nm,e}^{\text{out}} \mathrm{e}^{ikz_{nm,e}} + a_{nm,e}^{\text{in}} \mathrm{e}^{-ikz_{nm,e}}. \tag{46}$$

In this expression, $a_{nm,e}^{\text{out/in}}$ represent the complex wave amplitudes on edge e around vertex nm. As there are an infinite number of unknown wave amplitudes to solve

for, we exploit the periodicity of the structure to reduce the problem's dimension to $2|\mathcal{S}|$. This is achieved by applying Bloch's theorem [13], a method first introduced in the context of quantum wires by [232] and later expanded upon in [141].

Bloch's Theorem: *In a periodic potential or structure, the wavefunction* $\psi(\mathbf{r})$ *of a particle or wave can be expressed as the product of a plane wave and a periodic function. Specifically,*

$$\psi_{\boldsymbol{\kappa}}(\mathbf{r}) = e^{i\boldsymbol{\kappa}\cdot\mathbf{r}} u_{\boldsymbol{\kappa}}(\mathbf{r}), \tag{47}$$

where $\boldsymbol{\kappa}$ *is the wave vector,* $e^{i\boldsymbol{\kappa}\cdot\mathbf{r}}$ *is a plane wave, and* $u_{\boldsymbol{\kappa}}(\mathbf{r})$ *is an envelope function that has the same periodicity as the underlying lattice:*

$$u_{\boldsymbol{\kappa}}(\mathbf{r}) = u_{\boldsymbol{\kappa}}(\mathbf{r} + \mathbf{R}), \tag{48}$$

where $\mathbf{r} = (x, y)^T$ *is the position vector, and* $\mathbf{R} = (n\ell, m\ell)^T$ *is the lattice vector.*

The periodicity of the structure enforces a unitary spatial evolution of the wave function over the period ℓ:

$$|\psi_{nm,e}(\ell)|^2 = |\psi_{nm,e}(0)|^2. \tag{49}$$

In quantum mechanics, this implies that the probability distribution associated with the particle's position is identical in each unit cell of the periodic structure. Consequently, the solution in one unit cell can be expressed in terms of those in neighboring cells, up to a phase factor known as the Bloch phase, parameterized by the length scale ℓ.

For the entire structure, the wave function at a given vertex can be related to the

solutions at neighboring vertices:

$$\begin{aligned}
\psi_{nm,l}(\ell_x) &= \mathrm{e}^{-i\kappa_x \ell}\psi_{nm,r}(0),\\
\psi_{nm,r}(\ell_x) &= \mathrm{e}^{i\kappa_x \ell}\psi_{nm,l}(0),\\
\psi_{nm,d}(\ell_y) &= \mathrm{e}^{-i\kappa_y \ell}\psi_{nm,u}(0),\\
\psi_{nm,u}(\ell_y) &= \mathrm{e}^{i\kappa_y \ell}\psi_{nm,d}(0),
\end{aligned} \tag{50}$$

where κ_x and κ_y represent the quasi-momenta in the x and y directions.

Using Bloch's theorem, the problem dimension reduces to $2|\mathcal{S}|$, with the unknowns now being the wave amplitudes in the vicinity of a given vertex. Consequently, we drop the unnecessary indexing nm, simplifying the notation: $a^{\text{out/in}}_{nm,e} \to a^{\text{out/in}}_{e}$ and $z_{nm,e} \to z_e$. The general solution in equation (46) then becomes:

$$\psi_{nm,e}(z_e) = \mathrm{e}^{i(\kappa_x n + \kappa_y m)\ell}\left(a^{\text{out}}_e \mathrm{e}^{ikz_e} + a^{\text{in}}_e \mathrm{e}^{-ikz_e}\right). \tag{51}$$

To determine the remaining $2|\mathcal{S}|$ unknown wave amplitudes and thus the eigenfunction solutions of the quantum graph, we use the scattering theory introduced in Section 2.2. The equations in (50) relate the outgoing wave amplitudes $\mathbf{a}^{\text{out}} = (a^{\text{out}}_l, a^{\text{out}}_r, a^{\text{out}}_d, a^{\text{out}}_u)^T$ to the incoming wave amplitudes $\mathbf{a}^{\text{in}} = (a^{\text{in}}_l, a^{\text{in}}_r, a^{\text{in}}_d, a^{\text{in}}_u)^T$ as:

$$\mathbf{a}^{\text{in}} = \boldsymbol{P}(k, \kappa_x, \kappa_y)\mathbf{a}^{\text{out}}, \tag{52}$$

where

$$\boldsymbol{P} = \begin{pmatrix}
0 & \mathrm{e}^{i(k\ell_x - \kappa_x \ell)} & 0 & 0\\
\mathrm{e}^{i(k\ell_x + \kappa_x \ell)} & 0 & 0 & 0\\
0 & 0 & 0 & \mathrm{e}^{i(k\ell_y - \kappa_y \ell)}\\
0 & 0 & \mathrm{e}^{i(k\ell_y + \kappa_y \ell)} & 0
\end{pmatrix}. \tag{53}$$

The full system is then determined by the choice of vertex boundary conditions,

which define the vertex scattering matrix $\boldsymbol{S}$, performing the mapping:

$$\mathbf{a}^{\text{out}} = \boldsymbol{S}(k)\mathbf{a}^{\text{in}}. \tag{54}$$

Here, $\boldsymbol{S}$ can represent a general scattering matrix, not limited to single-vertex boundary conditions. It can also be defined by a lead scattering matrix $\boldsymbol{S}(k) = \boldsymbol{\sigma}(k)$, as in Equation (34), to represent some unit cell substructure, which will be considered in subsequent sections.

By substituting equation (54) into equation (53), we derive an eigenvalue condition involving the quantum map $\boldsymbol{U} = \boldsymbol{P}\boldsymbol{S}$:

$$\left[\mathbb{I} - \boldsymbol{U}(k, \kappa_x, \kappa_y)\right] \mathbf{a}^{\text{in}} = \mathbf{0}. \tag{55}$$

The dispersion curves are obtained from the secular equation:

$$\det\left[\mathbb{I} - \boldsymbol{U}(k, \kappa_x, \kappa_y)\right] = 0. \tag{56}$$

The remaining unknown wave amplitudes $\mathbf{a}^{\text{out}}$ can then be found by applying equation (54) to the eigenvector $\mathbf{a}^{\text{in}}$ from equation (55).

In the following section, we examine the simplest example of a square periodic quantum graph with Kirchhoff-Neumann vertex boundary conditions and then analyze the lattice spectrum in the presence of vertex resonances.

2.4.1 Worked Example - A Square Lattice

To begin, we consider the simplest graph configuration illustrated in Figure 11a). In this case, the edge metric is set equal to the lattice spacing, $\ell_x = \ell_y = \ell$, and the vertex boundary conditions are chosen to be Kirchhoff-Neumann. The vertex scattering matrix for this configuration is given by $\boldsymbol{S} = \boldsymbol{\Sigma}$, as defined in equation

(17) for $\lambda = 0$:

$$\boldsymbol{S}_{pq} = \frac{1}{2} - \delta_{pq}. \tag{57}$$

Substituting $\boldsymbol{S}$ into equation (56), the spectrum of the quantum graph given as:

$$2\cos(k\ell) = \cos(\kappa_x \ell) + \cos(\kappa_y \ell). \tag{58}$$

This result is well-known; in fact, the dispersive properties of any simply connected, square-periodic quantum graph in dimension D, with Kirchhoff-Neumann boundary conditions, can be expressed as:

$$\cos(k\ell) = \frac{1}{D}\sum_{j=1}^{D} \cos(\kappa_j \ell), \tag{59}$$

as shown in [232, 141]. Equation (58) is referred to as the "free space solution" as in the limit of small edge lengths, $0 < \ell \ll 1$, it is straightforward to show, via series expansion, that this equation reproduces the dispersive properties of free space:

$$\kappa^2 \approx \kappa_x^2 + \kappa_y^2, \tag{60}$$

where $\kappa = k/\sqrt{2}$ is a rescaled frequency term, with the factor $\sqrt{2}$ begin given by the dimension of the problem. For further details, see [224].

Figure 11 presents various representations of the spectrum derived from equation (58). Each representation offers unique insights into the system's properties. The resulting surface, or band, is shown in Figure 11b) and is periodic in $\boldsymbol{\kappa}$-space over the Brillouin Zone (BZ), defined as $BZ \in [-\frac{\pi}{\ell}, \frac{\pi}{\ell}]^2$. The shape of the band depends on the square-periodic graph topology and the chosen scattering matrix. In the long-wavelength regime (small values of k), the surface approximates a cone around the Γ-point, thereby reproducing the circularly dispersive nature of free space as described by equation (60). As the wavelength decreases (i.e., as k increases), the

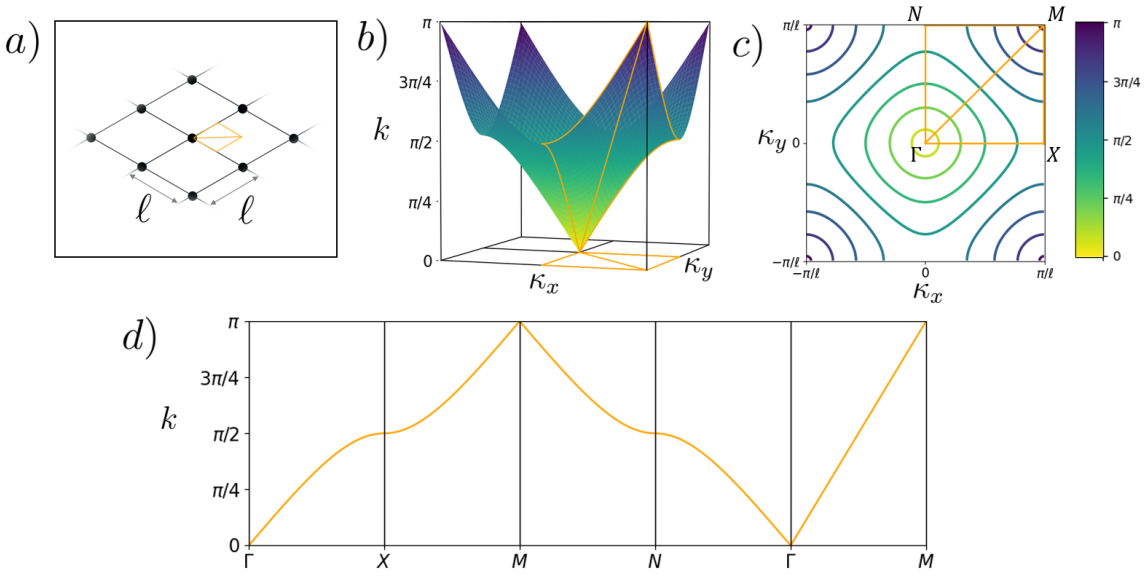

Figure 11: a) Illustrates the neighborhood of a vertex within a 2D square periodic quantum graph with period ℓ. b) Shows the band diagram over a frequency domain of $k \in [0, \pi/\ell]$. c) Displays a contour plot within the Brillouin Zone, with the points of symmetry Γ, X, M, and N labeled and connected by an orange line. d) Represents the momentum solutions between the points of symmetry within the Brillouin Zone.

lattice topology becomes more apparent, resulting in the diamond-shaped contours visible in the iso-frequency contour representation in Figure 11c).

Figure 11d) displays the momentum solutions between the high-symmetry points Γ, X, N, and M within the Brillouin Zone. This method of representation predates modern computational techniques and was traditionally used in solid-state physics for its trivial solvability and its clarity in depicting both group and phase velocity information along lines of symmetry. However, a key drawback of this historical approach is the potential loss of information regarding non-trivial wave effects that may occur between these lines of symmetry [233].

To construct the lattice solutions, consider a single frequency $k = 1/\ell$, which corresponds to a discrete ring of $\boldsymbol{\kappa} = (\kappa_x, \kappa_y)^T$ solutions on an iso-frequency contour. By selecting a specific point on this contour, one can construct the full wave solutions

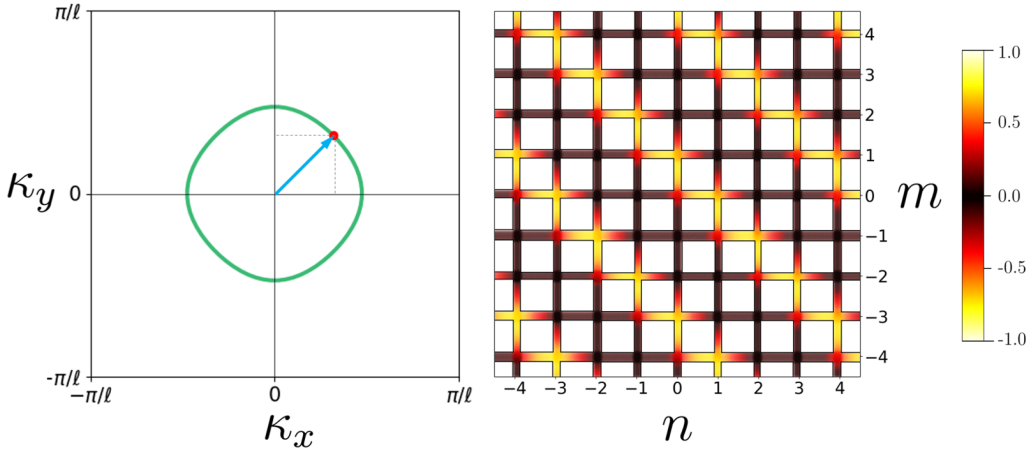

Figure 12: Left, the Iso-frequency contour of Figure 11b) at $k = 1/\ell$ with wave vector $\boldsymbol{\kappa} = (\frac{1}{\ell}, \frac{1}{\ell})^T$ emphasised with the blue arrow. Right, the resulting real component of the eigen function solution $\psi_{nm,e}(z_e; k, \kappa_x, \kappa_y)$

using the corresponding eigenfunction from equation (55), as illustrated in Figure 12.

2.4.2 Wave Function Visualization - Plotting Solutions

As a brief interlude, it is worth mentioning how the solutions were plotted, as shown in Figure 12. The wave functions on the graph were visualized by solving the eigenvalue equation in (55), where the dispersion relation $\kappa_x(k, \kappa_y)$ is implicitly defined by the determinant condition in equation (56). This approach reduces the problem to two variables, k and κ_y. The associated eigenvector $\mathbf{a}^{\text{in}}(k, \kappa_y)$ is computed either analytically or numerically, depending on the complexity of the problem, and the associated outgoing wave amplitudes $\mathbf{a}^{\text{out}}(k, \kappa_y)$ are determined by equation (54). This provides the complete set of wave amplitudes at the vertex. The eigenvector is then evolved along the graph bonds and across all vertices using the general solution of the graph differential operator, as described in equation (51), yielding the wave amplitude at every point on the graph.

To plot this data, a matrix of spatial coordinates and the corresponding real part

of the wave function was constructed in Python. Each wave function value was assigned a specific color, and a scatter plot was generated to represent the wave function in space. This procedure was applied to all wave function plots throughout this thesis.

2.4.3 Vertex Resonances - Engineering Band Gaps

This section acts as a key point of motivation for applying quantum graph theory to metamaterial design. We introduce a non-trivial vertex scattering matrix using the method from Section 2.3, drawing inspiration from Kuchment et al. [211]. The introduction of a vertex decoration leads to a frequency-dependent scattering matrix with resonances at specific frequencies, which are understood as the poles of an inverse operator. These poles result in spectral or band gaps in the secular equation (56), creating frequency ranges where wave propagation is forbidden. As discussed in the introduction, the formation of band gaps shifts what would traditionally be high-frequency effects into the low-frequency domain, enabling the existence of (meta)materials with non-trivial wave properties.

To demonstrate this, consider the vertex decoration illustrated in Figure 13a). This decoration acts as a sub-wavelength resonant element, consisting of a single edge of length ℓ_{res} that scatters waves between the four edge directions $\{l, r, d, u\}$. In this example, the scattering matrix that governs the interactions between all four edges is a 4×4 frequency-dependent matrix $\boldsymbol{S} = \boldsymbol{\sigma}_{res}$, with elements pq given by:

$$[\boldsymbol{\sigma}_{res}(k, \ell_{res})]_{pq} = \frac{1}{2 + \frac{1}{2i}\tan(k\ell_{res})} - \delta_{pq}. \tag{61}$$

This matrix is derived following the method in Section 2.3 with Equation (34). The transmission coefficient is $t_{res}(k, \ell_{res}) = \left[2 + \frac{1}{2i}\tan(k\ell_{res})\right]^{-1}$, which exhibits zeros at $k_n = \frac{(2n+1)\pi}{2\ell_{res}}$. Figure 13b) shows the transmission amplitude $T_{res}(k, \ell_{res}) = |t_{res}(k, \ell_{res})|^2$ and reflection amplitude $R_{res}(k, \ell_{res}) = |r_{res}(k, \ell_{res})|^2$ for various values

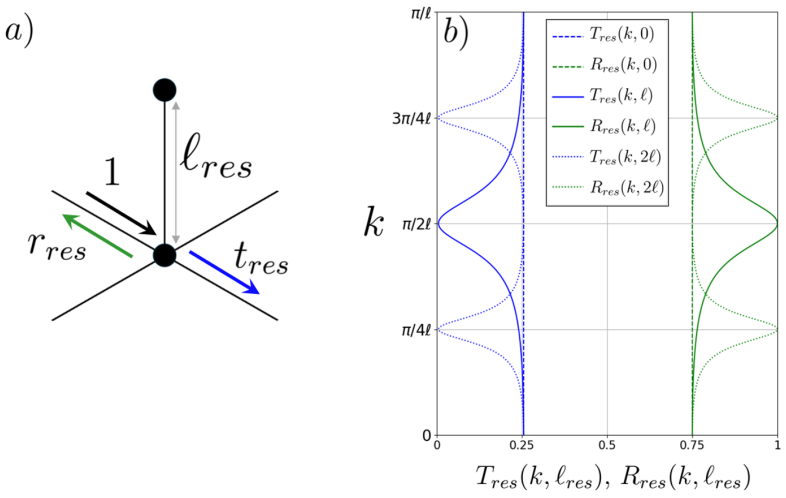

Figure 13: a) Shows a decorated vertex that forms the unit cell of the lattice. The decoration is a single edge of length ℓ_{res}, representing a sub-wavelength resonator. Illustrated is an incident wave of amplitude 1 that scatters into a green reflected wave of amplitude r_{res} and a blue transmitted wave of amplitude t_{res}. b) Shows both the transmission amplitude $T_{res}(k,\ell_{res}) = |t_{res}(k,\ell_{res})|^2$ and reflection amplitude $R_{res}(k,\ell_{res}) = |r_{res}(k,\ell_{res})|^2$ for various resonator lengths.

of ℓ_{res}. It is evident that at these resonant frequencies, transmission is forbidden, i.e., $T_{res}(k_n,\ell_{res}) = 0$. For $\ell_{res} = 0$, the scattering coefficients reduce to those of the Kirchhoff-Neumann case in equation (57).

The spectrum of the entire graph is then obtained by substituting this modified scattering matrix $\boldsymbol{S}$ into the secular equation (56), resulting in:

$$2\cos(k\ell) - \frac{1}{2}\sin(k\ell)\tan(k\ell_{res}) = \cos(\kappa_x\ell) + \cos(\kappa_y\ell). \tag{62}$$

The resulting band diagram for $\ell_{res} = \ell$ is plotted in Figure 14. In Figure 14a), we illustrate the neighborhood of a vertex in a 2D square periodic quantum graph, including a vertex decoration of length $\ell_{res} = 1$. Figures 14b) and 14c) display contour plots of the first and second bands within the Brillouin Zone, with the points of symmetry Γ, X, N, and M labeled and connected by an orange line.

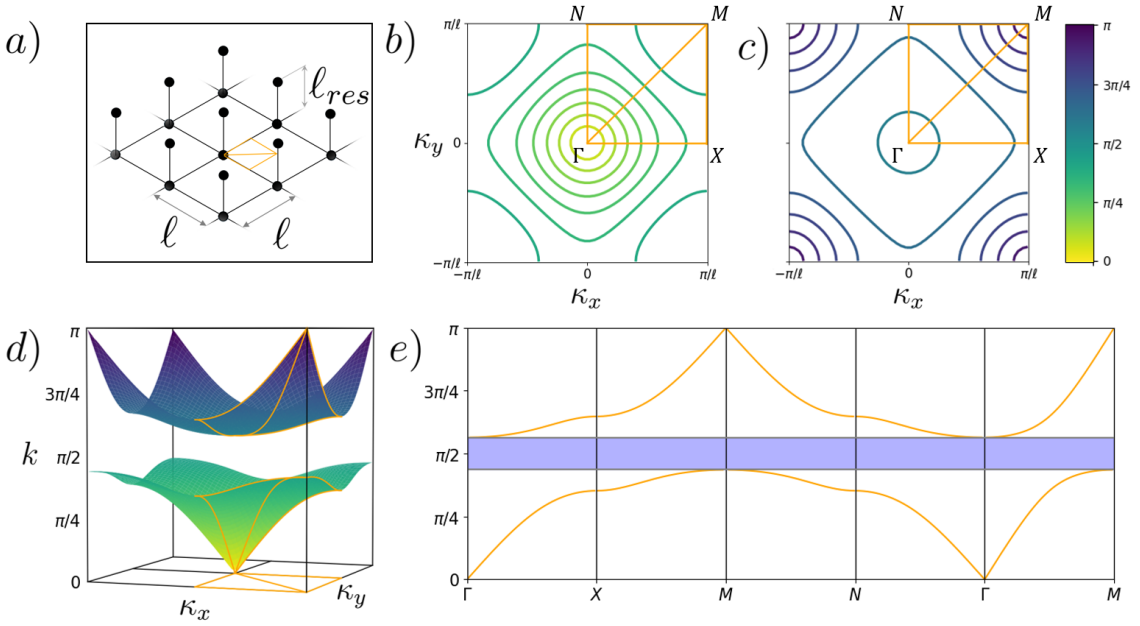

Figure 14: a) Illustrates the neighborhood of a vertex within a 2D square periodic quantum graph with period ℓ, with a vertex decoration consisting of a single edge of length $\ell_{res} = 1$. b) Shows a contour plot of the first band within the Brillouin Zone, highlighting the points of symmetry Γ, X, N, and M. c) Displays the contour plot of the second band. d) Presents the band diagram over a frequency domain of $k \in [0, \pi/\ell]$. e) Shows the momentum solutions between the points of symmetry within the Brillouin Zone, highlighting a band gap in blue.

The band diagram in Figure 14d) shows the domain $k \in [0, \pi/\ell]$, where a band gap is evident. This band gap, highlighted in blue in Figure 14e), represents a frequency range in which no real values of $\boldsymbol{\kappa}$ exist, indicating that wave transport through the mesh is prohibited. The presence of this gap results directly from the vertex resonance introduced in the system.

Additionally, the introduction of the resonance shifts the position of the diamond contour. In the isotropic case (Figure 11b and 11c), the diamond contour occurs at $k = \pi/2\ell$. However, with the vertex resonance, it shifts to $k = 3\pi/8$ in Figure 14b and 14c). This effect illustrates how high-frequency phenomena can be manipulated into the low-frequency domain, providing a mechanism for designing metamaterials

with tailored wave properties.

2.5 Chapter Summary

This chapter introduced the scattering formalism of quantum graph theory, where vertices act as point scatterers defined by variable boundary conditions. Special cases of vertex scattering, such as Kirchhoff-Neumann, Dirichlet, and δ-type boundary conditions, were explored to illustrate their impact on wave propagation at the vertices. As an example, the harmonics of a closed finite quantum graph were determined through the eigenvectors of the quantum map, which takes into account the graph's topology, metric, and boundary conditions.

The formalism was then extended to the spectrum of an open quantum graph, where scattering between leads was derived using an inverse operator related to a specific matrix block of the quantum map. Particular attention was given to cases where this matrix inverse leads to poles, resulting in instances where scattering between leads is not well-defined. Building on this, the scattering formulation was further extended to infinite periodic quantum graphs, revealing that the eigenvectors of the quantum map correspond to plane waves propagating within the lattice.

It was shown that introducing frequency-dependent vertex boundary conditions, constructed via finite open graphs attached at each lattice point, leads to resonant conditions that prohibit wave transport within the mesh. These spectral or band gaps arise as a direct consequence of the poles in the inverse operator defined by a sub-graph's quantum map, effectively driving high-frequency effects into the low-frequency regime.

The key learning outcomes of this chapter include understanding how boundary conditions and lattice geometry influence the band structure of quantum graphs, how resonant vertex conditions can be engineered to create band gaps, and the critical role of scattering matrices in describing wave propagation. These concepts set

the foundation for the next chapter, which focuses on Green's functions on quantum graphs, where the challenge of dealing with scattering at resonant frequencies becomes particularly significant.

3 Green's Functions on Quantum Graphs

In this chapter, based on the published work by Lawrie et al. [230], we present a comprehensive three-step procedure for deriving a closed-form expression of the Green's function for both closed and open finite quantum graphs with general self-adjoint matching conditions. Unlike in the previous chapter, where the interpretation of the field ψ was left open for various wave fields, we explicitly consider the operator on the graph to be the Schrödinger operator, with $k^2 = E$ representing the energy. Whilst of course, this formalism is applicable to other wave fields it is more natural to consider the graph harmonics in relation to the energy spectrum.

We begin by generalizing and simplifying the approach developed by Barra and Gaspard [229], before discussing the validity and application of the resulting explicit expressions. For compact graphs, we show that this expression is equivalent to the spectral decomposition, forming a sum over poles at the discrete energy eigenvalues, with residues containing the projector kernel onto the corresponding eigenstates.

Our derivation employs a scattering approach, where each vertex or subgraph is treated as a scattering site described by a scattering matrix. This matrix is formulated in a simple closed form, allowing for the subsequent derivation of the Green's function. We then address the fact that these scattering matrices involve inverse operators that become singular at specific wave numbers associated with bound states in the continuum. We explore the regularization of these singularities, related to bound states or perfect scars, and express the Green's functions or scattering matrices as a sum of regular and singular components, with the singular part encapsulating the projection kernel onto the perfect scar.

In the latter part of the chapter, we extend our analysis to periodic quantum graphs, introducing new results on the Green's function for infinite periodic systems.

3.1 Motivation

For a comprehensive introduction to solving partial differential equations, including foundational concepts and techniques not covered in detail in this chapter, readers are referred to the work of Renardy and Rogers [234]. For now, we motivate the importance of the Green function in the context of forcing. Throughout the previous chapter, we have primarily focused on solving the homogeneous differential equation,

$$\left(E - \hat{H}\right)\psi(z) = 0. \tag{63}$$

The eigenvector solutions $\psi(z)$ describe the stationary states of the system, which, in free space, can generally be expressed as a superposition of counter-propagating plane waves. This formulation has allowed us to understand the properties of quantum graphs through band diagrams, using plane wave representations. However, to apply the quantum graph model to physical systems, we must consider the system's response to external forces. This is modeled by inhomogeneous terms in the governing equation:

$$(E - \hat{H})\phi(z) = f(z). \tag{64}$$

Here, $\phi(z)$ represents the system's response to some external forcing $f(z)$. In general, finding a solution for $\phi(z)$ can be challenging, and thus we rely on well-established techniques in differential calculus, particularly Green's function.

Green's function is a fundamental tool in mathematical physics for solving linear differential equations, especially in cases involving point sources or external forcing functions [235]. The Green's function can be interpreted as a special solution to equation (64), where the forcing function is a Dirac delta function, $f(z) = \delta(z - z')$. The delta function is defined to be zero everywhere except at $z = z'$, while having a

unit integral:

$$1 = \int_{-\infty}^{\infty} \delta(z - z')\, dz, \tag{65}$$

The Green's function, therefore, satisfies the inhomogeneous differential equation:

$$(E - \hat{H})G(z, z') = \delta(z - z'). \tag{66}$$

This reduces to the homogeneous case in (63) everywhere except at the point of excitation, $z = z'$, allowing the Green function to be written as a superposition of counter propegating plane waves. The solution $\phi(z)$ to equation (64) can then be expressed as an integral over the source function $f(z')$ using the Green function:

$$\phi(z) = \int G(z, z')f(z')\, dz'. \tag{67}$$

To see why this holds, we apply the operator $(E - \hat{H})$ to both sides of the equation:

$$(E - \hat{H})\phi(z) = (E - \hat{H}) \int G(z, z')f(z')\, dz'. \tag{68}$$

Since the operator $(E - \hat{H})$ acts only on z, we can move it inside the integral,

$$(E - \hat{H})\phi(z) = \int (E - \hat{H})G(z, z')f(z')\, dz', \tag{69}$$

which from equation (66) naturally simplifies to,

$$(E - \hat{H})\phi(z) = \int \delta(z - z')f(z')\, dz'. \tag{70}$$

Due to the properties of the delta function as defined in equation (65), the integral

only gives non-zero values when $z = z'$, thus recovering the original inhomogeneous differential equation (64). This powerful method demonstrates the importance of Green's functions in solving differential equations with arbitrary forcing terms.

In 2001, Barra and Gaspard [229] used the scattering approach to express the Green's function of a quantum graph as a sum over trajectories in the spirit of semiclassical quantum mechanics. At the time, it was not yet clear within the physics community how scattering matrices are connected to matching conditions related to a well-defined self-adjoint Schrödinger operator on the metric graph. We generalize and simplify the approach [229] by using a simple three step procedure that leads to the Green's function for general self-adjoint matching conditions for closed and open graphs with a finite number of edges. This directly provides a number of closed form expressions that, to the best of our knowledge, have not been given before (though implied in [229], see also [231], where closed form expressions are given for a few simple examples). These closed forms are of great practical advantage when dealing with explicit graphs as they sum all relevant trajectories. Moreover, they are the starting point of an analysis of the validity and convergence of the Green's function when expressed as a sum over trajectories. We thus hope to provide a more straightforward way of computing Green's functions on graphs. This could lead to helpful insight into the growing literature on applications for Green's functions on graphs that often require relatively cumbersome sums over trajectories, see [236, 237, 238] and references therein.

We also discuss in some detail cases where the sum over trajectories fails to converge while closed form expressions may be regularized. Indeed, when evaluating the scattering matrix on open graphs, such as those used in the construction of the Green's function, one must take great care at frequencies corresponding to bound states in the continuum. These states vanish necessarily on the scattering leads and potentially lead to singular behaviour when considering the Green's function. Scarring of

eigenfunctions is a well-known semiclassical phenomenon in more general systems [239]. It has been known since the work of Schanz and Kottos [240] that quantum graphs allow for a much stronger scarring mechanism than in more general wave systems. These so-called perfect scars are non-vanishing only on a finite subset of the edges and vanish exactly in the remainder of the graph. They are easily constructed, for example, in certain quantum graphs with standard (Neumann-Kirchhoff) vertex matching conditions. For open graphs, bound states in the continuum are examples of perfect scars. Perfect scars lead to singularities in some inverted matrices that are used in the construction of scattering matrices and Green's function and this implies non-convergence of the related sums over trajectories at the corresponding wave number. We will explain that both the scattering matrix and the Green's function (outside the domain of the perfect scar) stay regular at these frequencies and give suitable regularised equations. These regularized expressions may be of practical importance even if there are no perfect scars on the graph. This is due to the far more generic phenomenon of almost perfect scars which was also described in [240]. These are states where the conditions for a perfect scar on a subgraph are fulfilled up to small terms leading to states which are only slightly coupled to outgoing channels. In the scattering matrix, almost perfect scars lead to what is known as topological resonances [241, 242]. In this context, a simplified variant of the regularization scheme we describe here has been used to derive the tails in the distribution of resonance widths [241].

This chapter is structured as follows: In Section. 3.2.1, a three step procedure for generating a closed form expression for the Green's function is introduced via the scattering approach formulated in Chapter 2. This formalism is then extended to include open quantum graph in Section 3.2.2. It is assumed that the graph scattering matrix is non-singular and well defined. In Section 3.3.1, a formal definition is given for a scar state in terms of the quantum map. It is shown that the block component of the quantum map that refers to the compact portion of the graph is non-invertible.

It is shown through a regularization of the scattering approach, that the full solution is indeed regular as it is evaluated within a reduced space. Further analysis of the scattering states for eigen energies approaching a scar state are investigated D. In Section. 3.4, we generate the Green's function in the presence of scars for the open lasso. This formalism is then extended to the infinite periodic quantum graph in Section 3.5. We finally conclude this work in section 3.6 with a brief summary this chapter.

3.2 Green's Functions on Quantum Graphs

The Green's function may be considered as the integral kernel of the resolvent operator $(E - \hat{H})^{-1}$ which has singularities at the spectrum of $\hat{H}$. It has poles at the discrete spectrum and a branch cut along the continuous spectrum.

For a given (complex) energy $E = k^2$ and two points $\mathbf{z} = (e, z_e)$ and $\mathbf{z}' = (e', z'_{e'})$ on a quantum graph, the Green's function $G(\mathbf{z}, \mathbf{z}', E)$ satisfies the inhomogeneous equation

$$\left(E - \hat{H}\right) G(\mathbf{z}, \mathbf{z}', E) = \delta(\mathbf{z}, \mathbf{z}') \equiv \begin{cases} \delta(z_e - z'_{e'}) & \text{if } e = e' \\ 0 & \text{if } e \neq e' \end{cases}, \tag{71}$$

where $\hat{H}$ acts on $\mathbf{z}$. The solution of this differential equation (71) with given self-adjoint matching conditions at the vertices may not be unique or not exist at all. The latter happens when the energy E belongs to the discrete real eigenvalue spectrum. For complex energies with a non-vanishing imaginary part, one can always find a unique square integrable solution and this then coincides with the integral kernel of the resolvent operator. The relation to the resolvent operator gives rise to the symmetry

$$G(\mathbf{z}, \mathbf{z}'; E) = G(\mathbf{z}', \mathbf{z}; E^*)^* \ . \tag{72}$$

We focus on the Green's function $G_+(\mathbf{z}, \mathbf{z}', E) \equiv G(\mathbf{z}, \mathbf{z}', E_+)$ with positive real and imaginary parts: $E_+ = k_+^2 = E_r + iE_i$ with $0 < E_r \in \mathbb{R}$ and $0 < E_i \in \mathbb{R}$. For

real energies that are not in the (discrete or continuous) eigenvalue spectrum, we allow the imaginary part to vanish, that is, $E_i = 0$, as the Green's function is well defined in that case. Solutions at real energies in the continuous spectrum require the limit $E_i \to 0^+$ which is always implied. If E_r belongs to the discrete eigenvalue spectrum, the Green's function has a pole $G(\mathbf{z}, \mathbf{z}'; E) \sim \frac{P(\mathbf{z},\mathbf{z}')}{E_i}$ (with a non-vanishing function $P(\mathbf{z}, \mathbf{z}')$) preventing the existence of the limit $E_i \to 0^+$. For brevity we write $E = E_+$ and $k = k_+$ during the following derivations.

To construct the Green's function, we exploit the fact that for all $\mathbf{z} \neq \mathbf{z}'$ the solutions to equation (71) are solutions to the homogeneous wave equation in (5). This allows one to express the solutions again as a linear superposition of counter propagating plane waves as express in (7). The set of unknown coefficients are then chosen to satisfy the imposed vertex boundary conditions as well as the appropriate boundary conditions at the delta function excitation $\mathbf{z} = \mathbf{z}'$. This procedure is detailed via a scattering approach in the following.

3.2.1 Green's Function of a Closed Finite Quantum Graph

The Green's function on a graph can be constructed in a three step procedure as illustrated in Figure 15.

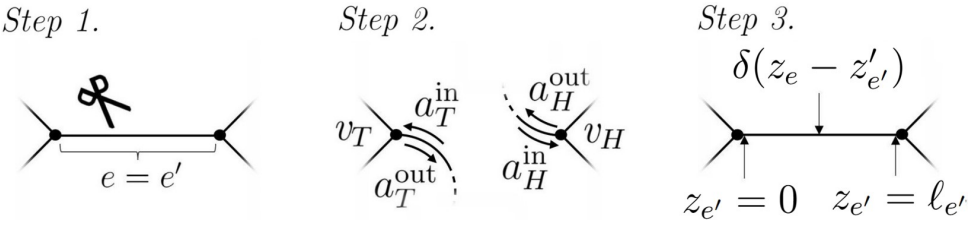

Figure 15: This three step procedure is described in detail below.

Step 1. Define the graph and the coordinate of the delta function excitation $\mathbf{z}' = (e', z'_{e'})$. The delta function acts as a source which we model by creating an auxiliary open scattering graph by "cutting out" the excited edge e' and replacing it with two auxiliary leads.

Step 2. Treat the auxiliary graph as a scattering site and construct a lead scattering matrix for energy E_+. This allows one to determine the two outgoing lead wave amplitudes in terms of the two incoming wave amplitudes which are free parameters.

Step 3. Take the scattering solution on the auxiliary leads at distances $z'_{e'}$ and $\ell_{e'} - z'_{e'}$ from the vertices and "glue" these solutions together such that the differential equation (71) is satisfied yielding a Dirac δ-function at the position $\mathbf{z}'$. This determines all free parameters and results in the Green's function $G(\mathbf{z}, \mathbf{z}'; E_+)$.

Let us now go through these steps in detail:

Step 1. Consider a compact quantum graph $\mathcal{G}(\mathcal{V}, \mathcal{E}, L)$ as defined in section 2 which we wish to excite with a delta function at location $\mathbf{z}' = (e', z'_{e'}) \in \mathcal{G}$. Let us denote the vertex at $z_{e'} = 0$ as the 'tail' vertex v_T and the vertex at $z_{e'} = l_{e'}$ as the 'head' vertex v_H. We begin by cutting the excited edge e' and replacing it by two leads attached at v_T and v_H, respectively, thus creating the auxiliary open scattering graph $\mathcal{G}_{\text{aux},e'} = \mathcal{G}_{\text{aux},e'}(\mathcal{V}, \mathcal{E}_{\text{aux,e'}}, L_{\text{aux,e'}})$, where $\mathcal{E}_{\text{aux,e'}} = \mathcal{L}_{\text{aux,e'}} \cup (\mathcal{B} \setminus \{e'\})$ and $L_{\text{aux,e'}} = L \setminus \{\ell_{e'}\}$. The coordinates on the leads are set to be $z_T = z_H = 0$ at the vertices v_T and v_H, respectively. On each lead, the solutions are defined as

$$\begin{aligned} \psi_T(z_T) &= a_T^{\text{in}} e^{-ik_+ z_T} + a_T^{\text{out}} e^{ik_+ z_T}, \\ \psi_H(z_H) &= a_H^{\text{in}} e^{-ik_+ z_H} + a_H^{\text{out}} e^{ik_+ z_H}. \end{aligned} \tag{73}$$

Step 2. Next, we construct the scattering states on the auxiliary graph. The quantum map of the auxiliary graph can then be written in the form equation (31) and only differs from the quantum map (23) of $\mathcal{G}$ by excluding the rows corresponding to the excited edge e'. The wave amplitudes on the two leads are mapped from incoming to outgoing wave amplitudes by the graph scattering matrix $\boldsymbol{\sigma}(k_+)$ as defined in

(33) with matrix elements

$$\begin{pmatrix} a_{\mathrm{H}}^{\mathrm{out}} \\ a_{\mathrm{T}}^{\mathrm{out}} \end{pmatrix} = \begin{pmatrix} \sigma(k_+)_{HH} & \sigma(k_+)_{HT} \\ \sigma(k_+)_{TH} & \sigma(k_+)_{TT} \end{pmatrix} \begin{pmatrix} a_{\mathrm{H}}^{\mathrm{in}} \\ a_{\mathrm{T}}^{\mathrm{in}} \end{pmatrix}. \tag{74}$$

The incoming wave amplitudes $a_{\mathrm{H}}^{\mathrm{in}}$ and $a_{\mathrm{T}}^{\mathrm{in}}$ are at this stage free parameters.

Step 3. We project the set of scattering solutions from the auxiliary graph onto the original graph by cutting the leads H and T at $z_{\mathrm{T}} = z'_{e'}$ and $z_{\mathrm{H}} = \ell_{e'} - z'_{e'}$, then "gluing" the two ends together forming a single bond. The solution on e' is then

$$\psi_{e'}(z_{e'}) = \begin{cases} a_{\mathrm{T}}^{\mathrm{in}} e^{-ik_+ z_{e'}} + \left(\sigma_{\mathrm{TH}} a_{\mathrm{H}}^{\mathrm{in}} + \sigma_{\mathrm{TT}} a_{\mathrm{T}}^{\mathrm{in}}\right) e^{ik_+ z_{e'}} & \text{for } z_{e'} < z'_{e'}; \\ a_{\mathrm{H}}^{\mathrm{in}} e^{-ik_+(\ell_{e'} - z_{e'})} + \left(\sigma_{\mathrm{HH}} a_{\mathrm{H}}^{\mathrm{in}} + \sigma_{\mathrm{HT}} a_{\mathrm{T}}^{\mathrm{in}}\right) e^{ik_+(\ell_{e'} - z_{e'})} & \text{for } z_{e'} > z'_{e'}. \end{cases} \tag{75}$$

One determines $a_{\mathrm{H}}^{\mathrm{in}}$ and $a_{\mathrm{T}}^{\mathrm{in}}$ by fulfilling equation (71) at $z_{e'} = z'_{e'}$; this leads to the following conditions:

i. continuity at $z_{e'} = z'_{e'}$

$$\lim_{\alpha \to 0^+} \left[\psi_{e'}(z'_{e'} + \alpha) - \psi_{e'}(z'_{e'} - \alpha)\right] = 0; \tag{76}$$

ii. a discontinuity of the derivatives of the form

$$\lim_{\alpha \to 0^+} \left[\frac{d\psi_{e'}\left(z'_{e'} + \alpha\right)}{dz_{e'}} - \frac{d\psi_{e'}\left(z'_{e'} - \alpha\right)}{dz_{e'}}\right] = 1\ . \tag{77}$$

These two conditions result in a non-homogeneous system of linear equations for the

two incoming scattering amplitudes. The unique solution of this system is

$$\begin{aligned} a_{\mathrm{T}}^{\mathrm{in}} =& \frac{e^{ik_+\ell_{e'}}\left(e^{-ik_+(\ell_{e'}-z'_{e'})}+\sigma_{\mathrm{HH}}e^{ik_+(\ell_{e'}-z'_{e'})}-\sigma_{\mathrm{TH}}e^{ik_+z'_{e'}}\right)}{2ik_+\left[(1-e^{ik_+\ell_{e'}}\sigma_{\mathrm{HT}})(1-e^{ik_+\ell_{e'}}\sigma_{\mathrm{TH}})-e^{2ik_+\ell_{e'}}\sigma_{\mathrm{HH}}\sigma_{\mathrm{TT}})\right]} \\ =& \frac{1}{2ik_+}\left[e^{ik_+z'_{e'}}\left[\frac{\mathbb{I}}{\mathbb{I}-\mathbf{U}(k_+)}\right]_{e'_-e'_-}+e^{ik_+(\ell_{e'}-z'_{e'})}\left[\frac{\mathbb{I}}{\mathbb{I}-\mathbf{U}(k_+)}\right]_{e'_-e'_+}\right] \qquad (78a) \\ a_{\mathrm{H}}^{\mathrm{in}} =& \frac{e^{ik_+\ell_{e'}}\left(e^{-ik_+z'_{e'}}+\sigma_{\mathrm{TT}}e^{ik_+z'_{e'}}-\sigma_{\mathrm{HT}}e^{ik_+(\ell_{e'}-z'_{e'})}\right)}{2ik_+\left[(1-e^{ik_+\ell_{e'}}\sigma_{\mathrm{HT}})(1-e^{ik_+\ell_{e'}}\sigma_{\mathrm{TH}})-e^{2ik_+\ell_{e'}}\sigma_{\mathrm{HH}}\sigma_{\mathrm{TT}})\right]} \\ =& \frac{1}{2ik_+}\left[e^{ik_+(\ell_{e'}-z'_{e'})}\left[\frac{\mathbb{I}}{\mathbb{I}-\mathbf{U}(k_+)}\right]_{e'_+e'_+}+e^{ik_+z'_{e'}}\left[\frac{\mathbb{I}}{\mathbb{I}-\mathbf{U}(k_+)}\right]_{e'_+e'_-}\right]. \qquad (78b) \end{aligned}$$

The derivation of the expressions involving $(\mathbb{I}-\mathbf{U}(k_+))^{-1}$, the resolvent matrix of the quantum map, can be found in Appendix A. Inserting (78) into (75) and extending the solution to the entire graph using (35), the Green's function of the compact graph $\mathcal{G}$ can finally be written in the form

$$\begin{aligned} G(\mathbf{z},\mathbf{z}',E_+) = \frac{1}{2k_+i} \quad & \Bigg[\delta_{ee'}e^{ik_+|z_e-z'_{e'}|}+e^{ik_+(z_e-z'_{e'}-\ell_e+\ell_{e'})}\left[\tfrac{\mathbf{U}(k_+)}{\mathbb{I}-\mathbf{U}(k_+)}\right]_{e_+e'_+} \\ & +e^{-ik_+(z_e-z'_{e'})}\left[\tfrac{\mathbf{U}(k_+)}{\mathbb{I}-\mathbf{U}(k_+)}\right]_{e_-e'_-} \\ & +e^{ik_+(z_e+z'_{e'}-\ell_e)}\left[\tfrac{\mathbf{U}(k_+)}{\mathbb{I}-\mathbf{U}(k_+)}\right]_{e_+e'_-} \\ & +e^{-ik_+(z_e+z'_{e'}-\ell_{e'})}\left[\tfrac{\mathbf{U}(k_+)}{\mathbb{I}-\mathbf{U}(k_+)}\right]_{e_-e'_+}\Bigg]. \qquad (79) \end{aligned}$$

Here of course δ_{ij} represents the Kronecker delta, where $\delta_{ij}=0$ for $i\neq j$ and $\delta_{ij}=1$ for $i=j$. This is our main result in this section. We give here for the first time a closed form expression of the Green's function on a graph following the recipe from Barras and Gaspard [229].

By formally expanding $\frac{\mathbf{U}}{\mathbb{I}-\mathbf{U}}=\sum_{n=1}^{\infty}\mathbf{U}^n$, one may express the Green's function as a sum over paths p on the metric graph starting at $\mathbf{z}'$ and ending at $\mathbf{z}$, that is,

$$G(\mathbf{z},\mathbf{z}',E_+)=\frac{1}{2k_+i}\sum_p A_p(k_+)e^{iL_pk_+}. \qquad (80)$$

Here, L_p is the metric length of the path and the amplitude A_p is the product of all scattering amplitudes along the trajectory. If $e = e'$, the direct path between $z_{e'}$ and $z'_{e'}$ has length $L_p = |z_{e'} - z'_{e'}|$ and $A_p = 1$. Equation (80) is the starting point for the investigations in [229], which, however, makes it necessary to do an explicit summation over all possible paths - in general a cumbersome task. Note also that this expansion converges only if the imaginary part of k_+ is positive and these expressions thus require a limit if used for real wave numbers. This is all well known for similar expansions into sums over paths in trace formulae and scattering systems, we refer to the textbook [172] and references therein.

Finally, let us briefly discuss the pole structure of the Green's function. For a compact graph, the eigenvalue spectrum is a discrete countable set $\{E_0, E_1, \dots\}$. Let us assume that there are no degeneracies and all eigenvalues are positive, that is, $E_n > 0$. The spectral decomposition of the Schrödinger operator $\hat{H}$ allows us to write the resolvent operator as

$$(E_+ - \hat{H})^{-1} = \sum_{n=0}^{\infty} \frac{\boldsymbol{P}_n}{E_+ - E_n} \tag{81}$$

where $\boldsymbol{P}_n$ is the projection operator onto the subspace spanned by the n-th eigenvector. For the Green's function this implies

$$G(\mathbf{z}, \mathbf{z}', E_+) = \sum_{n=0}^{\infty} \frac{P_n(\mathbf{z}, \mathbf{z}')}{E_+ - E_n} \tag{82}$$

where $P_n(\mathbf{z}, \mathbf{z}')$ is the integral kernel of $\boldsymbol{P}_n$. Let us now show that (79) and (82) are indeed equivalent. We start by considering the limit $E_+ \to E_n$ for some given eigenvalue $E_n = k_n^2$ and by showing that the singular part of the Green's function (79) in this limit is given by $\frac{P_n(\mathbf{z},\mathbf{z}')}{E_+ - E_n}$. Let us extract first the singular part of the matrix

$$\frac{\mathbf{U}(k_+)}{\mathbb{I} - \mathbf{U}(k_+)} \sim \frac{\mathbf{P}}{-i(k_+ - k_n)C} \ . \tag{83}$$

Here, $\mathbf{P} = \mathbf{b}^{\text{in}}\mathbf{b}^{\text{in}\dagger}$ is the projection matrix with matrix elements on the corresponding unit eigenvector $\mathbf{U}(k_n)\mathbf{b}^{\text{in}} = \mathbf{b}^{\text{in}}$ and

$$C = \mathbf{b}^{\text{in}\dagger}\left[k_n\mathbf{L} + \sin(k_n\mathbf{L})\mathbf{\Pi}\right]\mathbf{b}^{\text{in}} > 0 \tag{84}$$

is a positive constant and $\mathbf{L}$ is a $2N_B$ dimensional diagonal matrices with diagonal entries ℓ_e. We refer to Appendix B for a detailed derivation of (83) and (84). With $2k_+(k_+ - k_n) \sim E_+ - E_n$ one then finds

$$\begin{aligned} G(\mathbf{z},\mathbf{z}',E_+) \sim & \frac{\left(a^{\text{in}}_{e_-}e^{-ik_nz_e} + a^{\text{in}}_{e_+}e^{ik_n(z_e-\ell_e)}\right)^*\left(a^{\text{in}}_{e'_-}e^{-ik_nz_{e'}} + a^{\text{in}}_{e'_+}e^{ik_n(z_{e'}-\ell_{e'})}\right)}{C(E_+ - E_n)} \\ = & \frac{P_n(\mathbf{z},\mathbf{z}')}{E_+ - E_n}\ , \end{aligned} \tag{85}$$

where the last equality requires that the constant C gives the correct normalization of the projection kernel $P_n(\mathbf{z},\mathbf{z}')$. This is equivalent to $\sum_{e\in\mathcal{E}}\int_0^{\ell_e} P_n((e,z_e),(e,z_e))dz_e = 1$ which is easily checked by direct calculation. Repeating this calculation for E_+ near all other energy eigenvalues shows that expressions (79) and (82) have the same poles and the same residues. Both expressions can be continued analytically to the lower half plane where the imaginary part of the energy is negative. They are thus equivalent up to an entire function $F(E)$, (i.e., it is analytic in the whole complex plane). As both (79) and (82) vanish in the limit $E_i \to \pm\infty$, the same must be true for their difference $F(E)$. The entire function that vanishes in these limits for all E_r is $F(E) = 0$.

3.2.2 Green's Function of an Open Finite Quantum Graph

The construction of the Green's function on an open scattering graph follows analogously. In this case, our assumption that the energy has a positive imaginary part together with the requirement of square integrability leads to outgoing boundary conditions along the leads. That is, the amplitudes of incoming plane waves need to

vanish, as these would lead to exponentially increasing contributions. These conditions are straight forward to implement and we can go through the same construction as for the compact graph. A short-cut is obtained by first replacing each lead $e \in \mathcal{L}$ by an edge of finite length with a dangling vertex of degree one and choosing some self-adjoint boundary conditions at the dangling vertices. This results in an auxiliary compact quantum graph as described in the previous section. The Green's function of the auxiliary quantum graph is then given by (79). Clearly, the solution depends on the lengths that have been introduced for the leads as parameters. Next, one sends the introduced edge lengths to infinity. Because the imaginary part of the wave number is positive Im $k_+ > 0$ the corresponding phase factors then decay as $e^{ik_+\ell_e} \to 0$ as $\ell_e \to \infty$. In this limit any dependence on the arbitrary choice of boundary conditions at the dangling vertices disappears and what remains is the Green's function of the open graph. We refer to Appendix C for the details of the

calculation which results in

$$G(\mathbf{z},\mathbf{z}',E_+) = \frac{1}{2k_+ i}\times$$
$$\begin{cases} \delta_{e,e'}\, e^{ik_+|z_e - z'_{e'}|} + e^{ik_+(z_e+z'_{e'})}\left[\mathbf{U}(k_+)_{\mathcal{L}\mathcal{L}} + \mathbf{U}(k_+)_{\mathcal{L}\mathcal{B}}\frac{\mathbb{I}}{\mathbb{I}-\mathbf{U}(k_+)_{\mathcal{B}\mathcal{B}}}\mathbf{U}(k_+)_{\mathcal{B}\mathcal{L}}\right]_{ee'} \\ \qquad\qquad \text{if } e,e' \in \mathcal{L}, \\ e^{ik_+(z_e - z'_{e'}+\ell_{e'})}\left[\mathbf{U}(k_+)_{\mathcal{L}\mathcal{B}}\frac{\mathbb{I}}{\mathbb{I}-\mathbf{U}(k_+)_{\mathcal{B}\mathcal{B}}}\right]_{ee'_+} + e^{ik_+(z_e+z'_{e'})}\left[\mathbf{U}(k_+)_{\mathcal{L}\mathcal{B}}\frac{\mathbb{I}}{\mathbb{I}-\mathbf{U}(k_+)_{\mathcal{B}\mathcal{B}}}\right]_{ee'_-} \\ \qquad\qquad \text{if } e \in \mathcal{L} \text{ and } e' \in \mathcal{B}, \\ e^{-ik_+(z_e - z'_{e'})}\left[\frac{\mathbb{I}}{\mathbb{I}-\mathbf{U}(k_+)_{\mathcal{B}\mathcal{B}}}\mathbf{U}(k_+)_{\mathcal{B}\mathcal{L}}\right]_{e_-e'} + e^{ik_+(z_e+z'_{e'}-\ell_e)}\left[\frac{\mathbb{I}}{\mathbb{I}-\mathbf{U}(k_+)_{\mathcal{B}\mathcal{B}}}\mathbf{U}(k_+)_{\mathcal{B}\mathcal{L}}\right]_{e_+e'} \\ \qquad\qquad \text{if } e \in \mathcal{B} \text{ and } e' \in \mathcal{L}, \\ \delta_{ee'}\, e^{ik_+|z_e - z'_{e'}|} + e^{ik_+(z_e - z'_{e'}-\ell_e+\ell_{e'})}\left[\frac{\mathbf{U}(k_+)_{\mathcal{B}\mathcal{B}}}{\mathbb{I}-\mathbf{U}(k_+)_{\mathcal{B}\mathcal{B}}}\right]_{e_+e'_+} + e^{-ik_+(z_e - z'_{e'})}\left[\frac{\mathbf{U}(k_+)_{\mathcal{B}\mathcal{B}}}{\mathbb{I}-\mathbf{U}(k_+)_{\mathcal{B}\mathcal{B}}}\right]_{e_-e'_-} \\ \quad + e^{ik_+(z_e+z'_{e'}-\ell_e)}\left[\frac{\mathbf{U}(k_+)_{\mathcal{B}\mathcal{B}}}{\mathbb{I}-\mathbf{U}(k_+)_{\mathcal{B}\mathcal{B}}}\right]_{e_+e'_-} + e^{-ik_+(z_e+z'_{e'}-\ell_{e'})}\left[\frac{\mathbf{U}(k_+)_{\mathcal{B}\mathcal{B}}}{\mathbb{I}-\mathbf{U}(k_+)_{\mathcal{B}\mathcal{B}}}\right]_{e_-e'_+} \\ \qquad\qquad \text{if } e,e' \in \mathcal{B}. \end{cases} \tag{86}$$

If the energy spectrum of the graph is continuous these expressions are regular and the limit Im $k_+ \to 0^+$ can be performed by just choosing $k_+ \to k \in \mathbb{R}$. A similar expression for energies $E_-^2 = k_-^2$ with negative imaginary parts may be obtained in the same way. More directly, it can be obtained from the symmetry (72). Note that it will have a different limit as k_- approaches the real axis.

We note, the form of the Green function in equation (86) under the condition that we consider both the measured and excited edge on the bond, $e, e' \in \mathcal{B}$, takes a similar form to the Green function of a cavity in [243] for equation (4). Indeed, future work would be to represent the formulism above in a similar manner to that found in [243].

The energy spectrum of an open graph may contain a discrete set $\{E_0, E_1, \dots\}$ of bound states in the continuum. These have square integrable eigenfunctions and they thus vanish on the leads. The Green's function for E close to any of these energy eigenvalues will have poles just as in the compact case that we discussed in the previous section. And the calculation there applies here as well. If either $\mathbf{z}$ or $\mathbf{z}'$ is chosen on a lead the expression for the Green's function should remain regular as $E \to E_n = k_n^2$ which is not obvious from the given explicit expressions above which contain the inverse $(\mathbb{I} - U(k_+)_{\mathcal{BB}})^{-1}$. We will show regularity explicitly if both $\mathbf{z}$ and $\mathbf{z}'$ are on the leads. In that case the expression above reduces to

$$G(\mathbf{z}, \mathbf{z}', E_+) = \frac{1}{2k_+ i}\left[\delta_{e,e'}\, e^{ik_+|z_e - z'_{e'}|} + e^{ik_+(z_e + z'_{e'})}\boldsymbol{\sigma}(k_+)_{e,e'}\right] . \tag{87}$$

We will show in the following section that the scattering matrix is indeed analytic as $k \to k_n$ for at a bound state. Regularity in the case that one point is on a lead and the other on a bond can be shown as well using essentially the same tools but we will leave this to the reader.

3.3 Regularisation schemes for perfect scars

3.3.1 Bound states in the continuum

The eigenstates of a quantum graph are generally supported on all edges of a graph as long as the graph is fully connected. However, it is not too difficult to construct graphs which have eigenstates that are non-zero exclusively on a compact subgraph $\mathcal{S}$, but vanish exactly on the rest $\mathcal{R}$ of the edges. We call such an eigenstate a *perfect scar* of the graph. These states exist, for example, on quantum graphs with Kirchhoff-Neumann conditions where the subgraph $\mathcal{S}$ is a cycle on which all edge lengths are rationally dependent. In that case, the cycle edge lengths are an integer multiple of a minimal length $\ell_e = n_e \ell_0$. At wave number $\tilde{k} = 2\pi/\ell_0$ (or any integer multiple of it), one may then set

$$\psi_e(z_e) = \begin{cases} \pm \sin(\tilde{k} z_e) & \text{if e belongs to the cycle of } \mathcal{S}; \\ 0 & \text{if e belongs to } \mathcal{R}. \end{cases} \tag{88}$$

Here the signs $\pm$ can be chosen to satisfy the flux conservation condition.

Since the union of $\mathcal{S}$ and $\mathcal{R}$ make up the total graph $\mathcal{G}$, it is natural to express the quantum map in the block-form

$$\mathbf{U}(k) = \begin{pmatrix} \mathbf{U}(k)_{\mathcal{R}\mathcal{R}} & \mathbf{U}(k)_{\mathcal{R}\mathcal{S}} \\ \mathbf{U}(k)_{\mathcal{S}\mathcal{R}} & \mathbf{U}(k)_{\mathcal{S}\mathcal{S}} \end{pmatrix} \tag{89}$$

with appropriate permutations applied. In general there is perfect scar on the subgraph $\mathcal{S}$ at energy $E = k^2 > 0$, if the block $\mathbf{U}(k)_{\mathcal{S}\mathcal{S}}$ has an eigenvector $\mathbf{a}^{\text{in}}_{\mathcal{S}}$ with unit eigenvalue $\mathbf{U}(k)_{\mathcal{S}\mathcal{S}}\mathbf{a}^{\text{in}}_{S} = \mathbf{a}^{\text{in}}_{\mathcal{S}}$. The unitarity of the full quantum map then implies that $\mathbf{U}(k)_{\mathcal{R}\mathcal{S}}\mathbf{a}^{\text{in}}_{\mathcal{S}} = 0$ vanishes. One may extend $\mathbf{a}^{\text{in}}_{\mathcal{S}}$ to an eigenvector of the full map by setting $\mathbf{a}^{\text{in}}_{\mathcal{R}} = 0$ resulting in the vanishing of wave amplitudes on edges that do not belong to $\mathcal{S}$.

For open graphs, a perfect scar at a wavenumber $k_0 > 0$ is a bound state in the continuum and this situation is again straight forward to construct, such as by using the cycle example above. In this case, one may take $\mathcal{R}$ to contain all leads and $\mathcal{S}$ to be a sub-graph containing a sub-set of the finite bonds.

Throughout the previous sections, we assumed that the matrix $\mathbb{I} - \mathbf{U}(k)_{\mathcal{BB}}$ is invertible, which is generically the case as $\mathbf{U}(k)_{\mathcal{BB}}$ is a block of a unitary matrix. However, a perfect scar exists, if and only if $\mathbf{U}(k)_{\mathcal{BB}}$ has an eigenvalue one at the wave number $k = k_0$. Even in the case of "almost" perfect scars (with small nonzero entries for $\mathbf{a}^{\text{in}}_{\mathcal{R}}$), matrix inversion may cause large numerical errors when inverting $\mathbb{I} - \mathbf{U}(k)_{\mathcal{BB}}$. To deal with this issue, we describe a regularisation scheme of the scattering matrix in the following section. This is important when dealing with open quantum graphs and when constructing Green's function both in the compact and open case. The approach may also be used to find the regular part of the Green's function in compact quantum graphs when the energy is in the eigenvalue spectrum. (By regular part, we refer to the Green's function where the contribution from the pole at the energy has been removed). We will focus on the regularization of the scattering matrix, as the other applications can all be derived from there when needed.

3.3.2 Regularization of the scattering approach at a bound state

We will show in this section that scattering solutions of the form (33) are well defined at $k = k_0$ even in the presence of a bound state at that wave number. We show in Appendix D that the scattering matrix can be regularised across a k interval containing k_0.

Consider a non-degenerate bound state at wave number $k = k_0$ with wave amplitudes $\mathbf{b}^{\text{in}}_{\mathcal{B}}$ such that,

$$\mathbf{U}(k_0)_{\mathcal{BB}}\, \mathbf{b}^{\text{in}}_{\mathcal{B}} = \mathbf{b}^{\text{in}}_{\mathcal{B}} \ . \tag{90}$$

As discussed in the previous section, the unitarity of the quantum map $\mathbf{U}(k)$ implies

$$\mathbf{U}(k_0)_{\mathcal{LB}}\mathbf{b}^{\text{in}}_{\mathcal{B}} = 0 \qquad \text{and} \qquad \mathbf{b}^{\text{in}\dagger}_{\mathcal{B}}\mathbf{U}(k_0)_{\mathcal{BL}} = 0, \tag{91}$$

that is, incoming waves $\mathbf{a}^{\text{in}}_{\mathcal{L}}$ in the leads can not couple into the bound state $\mathbf{b}^{\text{in}}_{\mathcal{B}}$ and the bound state can not couple back out. Let us assume for simplicity that the perfect scar described by $\mathbf{b}^{\text{in}}_{\mathcal{B}}$ is not degenerate and introduce the idempotent, Hermitian $2N_{\mathcal{B}} \times 2N_{\mathcal{B}}$ projection matrix

$$\mathbf{P} \equiv \mathbf{b}^{\text{in}}_{\mathcal{B}}\mathbf{b}^{\text{in}\dagger}_{\mathcal{B}} \tag{92}$$

and its orthogonal complement

$$\mathbf{Q} = \mathbb{I} - \mathbf{P} \ . \tag{93}$$

The methods below can be generalised to situations where more than one perfect scar exists at the same wave number k_0, such as, if all edge lengths are rationally related in a large graph with Neumann-Kirchhoff matching conditions. Writing equation (35) in the form

$$(\mathbb{I} - \mathbf{U}(k)_{\mathcal{BB}})\,\mathbf{a}^{\text{in}}_{\mathcal{B}} = \mathbf{U}(k)_{\mathcal{BL}}\mathbf{a}^{\text{in}}_{\mathcal{L}}, \tag{94}$$

we find that the solution $\mathbf{a}^{\text{in}}_{\mathcal{B}}$ is not unique at $k = k_0$ as both

$$\mathbf{P}\,(\mathbb{I} - \mathbf{U}(k_0)_{\mathcal{BB}}) = 0 \quad \text{and} \quad \mathbf{P}\mathbf{U}(k_0)_{\mathcal{BL}} = 0, \tag{95}$$

which follows directly from (91). This implies, that for any solution $\mathbf{a}^{\text{in}}_{\mathcal{B}}$ of equation (94), $\mathbf{a}^{\text{in}}_{\mathcal{B}} + \alpha\mathbf{b}^{\text{in}}_{\mathcal{B}}$, $\alpha \in \mathbb{C}$, is also a solution. However, a unique solution $\tilde{\mathbf{a}}^{\text{in}}_{\mathcal{B}}$ exists for the reduced system of equations

$$\mathbf{Y}_Q(k_0)\,\tilde{\mathbf{a}}^{\text{in}}_{\mathcal{B}} = \mathbf{U}(k_0)_{\mathcal{BL}}\,\mathbf{a}^{\text{in}}_{\mathcal{L}} \quad \text{with} \quad \mathbf{Y}_Q(k_0) = \mathbf{Q}\,(\mathbb{I} - \mathbf{U}(k_0)_{\mathcal{BB}})\,\mathbf{Q}. \tag{96}$$

As $\mathbf{Y}_Q(k_0)\mathbf{b}_{\mathcal{B}}^{\text{in}} = 0$, its standard inverse does not exist. One may perform a pseudo inverse in the subspace orthogonal to $\mathbf{b}_{\mathcal{B}}^{\text{in}}$. Let us define (with mild abuse of notation)

$$\mathbf{Y}_Q(k_0)^{-1} = \mathbf{Q}\frac{\mathbb{I}}{\mathbb{I} - \mathbf{Q}\mathbf{U}(k_0)\mathbf{Q}}\mathbf{Q} \tag{97}$$

as the unique $2N_{\mathcal{B}} \times 2N_{\mathcal{B}}$ matrix with by $\mathbf{Y}_Q(k_0)^{-1}\mathbf{Y}_Q(k_0) = \mathbf{Q} = \mathbf{Y}_Q(k_0)\mathbf{Y}_Q(k_0)^{-1}$ and $\mathbf{Y}_Q(k_0)^{-1}\mathbf{P} = 0 = \mathbf{P}\mathbf{Y}_Q(k_0)^{-1}$. As $\mathbf{U}(k_0)_{\mathcal{L}\mathcal{B}}\mathbf{P} = 0$, one obtains a well-defined scattering solution for equation (33), that is,

$$\mathbf{a}(k)_{\mathcal{L}}^{\text{out}} = \mathbf{U}(k_0)_{\mathcal{L}\mathcal{B}}\,\tilde{\mathbf{a}}_{\mathcal{B}}^{\text{in}}. \tag{98}$$

We may thus write the scattering matrix (34) in the form

$$\boldsymbol{\sigma}(k_0) = \mathbf{U}(k_0)_{\mathcal{L}\mathcal{L}} + \mathbf{U}(k_0)_{\mathcal{L}\mathcal{B}}\mathbf{Y}_Q(k_0)^{-1}\mathbf{U}(k_0)_{\mathcal{B}\mathcal{L}}\ . \tag{99}$$

For an in-depth discussion of the regularity of the scattering matrix as $k \to k_0$, see Appendix D.

3.4 Worked examples - Open Lasso

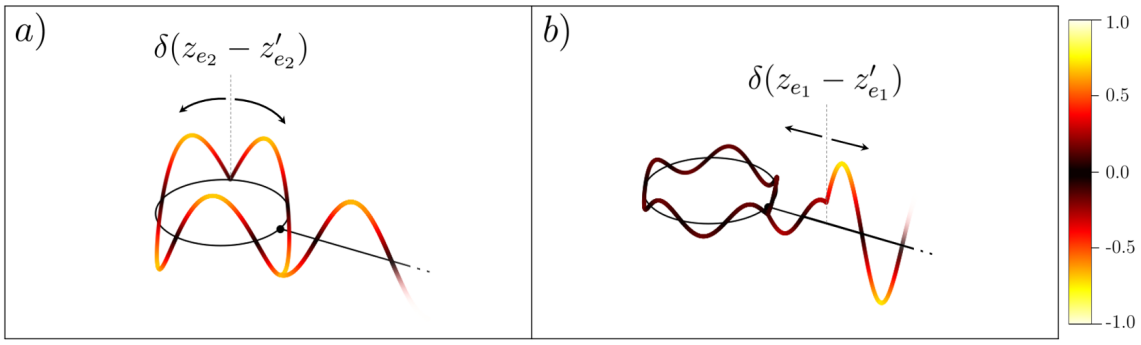

Figure 16: An open lasso graph constructed from two edges e_1 and e_2 where e_1 is a lead and e_2 is an bond. Both edges are connected to the same vertex v_1 where edge e_2 has both ends connected forming a loop wherein bound states can exist in the continuum. The real component of the Green function has been plotted for an excitation on the edge as in a), and the lead as in b).

Consider the open lasso quantum graph illustrated in figure 16. The coordinate $z_1 \geq 0$ runs along the lead with $z_1 = 0$ at the vertex v_1 and the coordinate $z_2 \in [0, \ell_2]$ runs along the loop such that $z_2 = 0$ and $z_2 = \ell_2$ are the endpoints at the vertex v_1. At the vertex, we enforce Neumann boundary conditions, as expressed in (17) for $\lambda^{(v)} = 0$, leading to the quantum map written in block form as

$$\mathbf{U}(k) = \left(\begin{array}{c|cc} -\frac{1}{3} & \frac{2}{3} & \frac{2}{3} \\ \hline \frac{2e^{ik\ell_2}}{3} & \frac{2e^{ik\ell_2}}{3} & -\frac{e^{ik\ell_2}}{3} \\ \frac{2e^{ik\ell_2}}{3} & -\frac{e^{ik\ell_2}}{3} & \frac{2e^{ik\ell_2}}{3} \end{array}\right) \equiv \begin{pmatrix} \mathbf{U}_{\mathcal{LL}} & \mathbf{U}_{\mathcal{LB}} \\ \mathbf{U}(k)_{\mathcal{BL}} & \mathbf{U}(k)_{\mathcal{BB}} \end{pmatrix}. \tag{100}$$

In the construction of the scattering matrix and the Green's function, one needs to invert the matrix $\mathbb{I} - \mathbf{U}(k)_{\mathcal{BB}}$ which yields

$$\frac{\mathbb{I}}{\mathbb{I} - \mathbf{U}(k)_{\mathcal{BB}}} = \begin{pmatrix} \frac{3-2e^{ik\ell_2}}{\left(e^{ik\ell_2}-1\right)\left(e^{ik\ell_2}-3\right)} & -\frac{e^{ik\ell_2}}{\left(e^{ik\ell_2}-1\right)\left(e^{ik\ell_2}-3\right)} \\ -\frac{e^{ik\ell_2}}{\left(e^{ik\ell_2}-1\right)\left(e^{ik\ell_2}-3\right)} & \frac{3-2e^{ik\ell_2}}{\left(e^{ik\ell_2}-1\right)\left(e^{ik\ell_2}-3\right)} \end{pmatrix} \tag{101}$$

and is well defined as long as $e^{ik\ell_2} \neq 1$, that is, if $k \neq k_n = 2\pi n/\ell_2$ for $n = 1, 2, \ldots$. The reason for this is the existence of perfect scars on the loop which here lead to bound states in the continuum of scattering states. These bound state wave functions are given as

$$\psi_1(z_1) = 0, \tag{102a}$$

$$\psi_2(z_2) = \sqrt{\frac{2}{\ell_2}} \sin(k_n z_2) \ . \tag{102b}$$

The continuum of scattering states exists for all wave numbers $k > 0$ and is given by

$$\psi_{e_1}(z_1) = e^{-ikz_1} + \boldsymbol{\sigma}(k) e^{ikz_1}, \tag{103a}$$

$$\psi_{e_2}(z_2) = \boldsymbol{\rho}(k)_{2_+1} e^{ik(z_2-\ell_2)} + \boldsymbol{\rho}(k)_{2_-1} e^{-ikz_2} \ . \tag{103b}$$

where

$$\boldsymbol{\rho}(k) = \frac{\mathbb{I}}{\mathbb{I} - \mathbf{U}(k)_{\mathcal{B}\mathcal{B}}} \mathbf{U}(k)_{\mathcal{B}\mathcal{L}} = \begin{pmatrix} \frac{2e^{ik\ell_2}}{3-e^{ik\ell_2}} \\ \\ \frac{2e^{ik\ell_2}}{3-e^{ik\ell_2}} \end{pmatrix} \tag{104}$$

and

$$\boldsymbol{\sigma}(k) = \mathbf{U}_{\mathcal{L}\mathcal{L}} + \mathbf{U}_{\mathcal{L}\mathcal{B}} \boldsymbol{\rho}(k) = \frac{3e^{ik\ell_2} - 1}{3 - e^{ik\ell_2}} \ . \tag{105}$$

While the matrix $\frac{\mathbb{I}}{\mathbb{I} - \mathbf{U}(k)_{\mathcal{B}\mathcal{B}}}$ is used to find $\boldsymbol{\rho}(k)$ and $\boldsymbol{\sigma}(k)$ in the scattering approach the poles at $k = k_n$ have disappeared in the final results. This is a unique consequence of chosen example where the bound states and scattering states are trivially orthogonal due to their symmetry under $z_2 \mapsto \ell_2 - z_2$ (which can be viewed as a mirror symmetry of the lasso). The bound states are odd under this symmetry as $\psi_{e_1}(z_1) = 0$ and $\psi_2(z_2) = -\psi_{e_2}(\ell_2 - z_2)$ at wave numbers k_n. The scattering states are even under this symmetry for all wave numbers $k > 0$ as

$$\psi_2(z_2) = \frac{4e^{ik\ell_2/2}}{3 - e^{ik\ell_2}} \cos\left(k \frac{2z_2 - \ell_2}{2}\right) = \psi_2(\ell_2 - z_2). \tag{106}$$

While in this example it is trivial to show analytically that the poles in equation (101) disappear, we may consider more complicated examples, where the matrix $\frac{\mathbb{I}}{\mathbb{I}-\mathbf{U}(k)_{\mathcal{BB}}}$ has to be solved numerically, leading to a large error in the scars of the lasso $k = k_n$. For completeness, let us evaluate the same problem at a pole corresponding to a scar of the lasso and show that the formulism in Section 3.3 for equation (99) gives the equivalent reflection coefficient in equation (105).

To begin, we determine the bond quantum map at resonance $k = k_n$:

$$\mathbf{U}(k_n)_{\mathcal{BB}} = \begin{pmatrix} \frac{2}{3} & -\frac{1}{3} \\ -\frac{1}{3} & \frac{2}{3} \end{pmatrix}, \tag{107}$$

and determine it corresponding eigen vector:

$$\mathbf{b}^{\text{in}}_{\mathcal{B}} = \begin{pmatrix} \frac{1}{\sqrt{2}} \\ -\frac{1}{\sqrt{2}} \end{pmatrix}. \tag{108}$$

From here, it is trivial to determine the idempotent projection matrix from equation (92) as well as its orthogonal complement from equation (93),

$$\mathbf{P} = \frac{1}{2}\begin{pmatrix} 1 & -1 \\ -1 & 1 \end{pmatrix} \quad \text{and} \quad \mathbf{Q} = \frac{1}{2}\begin{pmatrix} 1 & 1 \\ 1 & 1 \end{pmatrix}. \tag{109}$$

From here $\mathbf{Q}$ can be substituted into equation (97) to give a well-defined inverse in the presence of poles. Explicitly:

$$\mathbf{Y}_Q(k_n)^{-1} = \frac{3}{4}\begin{pmatrix} 1 & 1 \\ 1 & 1 \end{pmatrix}, \tag{110}$$

which when substituted into equation (99) gives unit reflection $\sigma(k_n) = 1$, which agrees directly with the result in equation (105).

Having fully defined the lead scattering matrix in the presence of scars, in both presented methodologies, we give the full Green function for this example below, where z_e (or $z'_{e'}$) are either on the lead ($e = e_1$) or on the loop ($e = e_2$). Following on from the last line in (86), one obtains, using the expressions in (100) and (101),

$$G_{\text{lasso}}(\mathbf{z}, \mathbf{z}', E_+) = \frac{1}{2k_+ i} \times \begin{cases} e^{ik_+|z_{e_1} - z'_{e_1}|} + e^{ik_+(z_{e_1} + z'_{e_1})} \frac{3e^{ik_+\ell_2} - 1}{3 - e^{ik_+\ell_2}} & \text{if } e = e_1 \text{ and } e' = e_1, \\ \frac{2}{3 - e^{ik_+\ell_2}} e^{ik_+ z_{e_1}} \left(e^{ik_+ z'_{e_2}} + e^{-ik_+(z'_{e_2} - \ell_2)} \right) & \text{if } e = e_1 \text{ and } e' = e_2, \\ \frac{2}{3 - e^{ik_+\ell_2}} e^{ik_+ z'_{e_1}} \left(e^{ik_+ z_{e_2}} + e^{-ik_+(z_{e_2} - \ell_2)} \right) & \text{if } e = e_2 \text{ and } e' = e_1, \\ e^{ik_+|z_{e_2} - z'_{e_2}|} + \alpha \left[(2 - e^{ik_+\ell_2}) \cos(k_+(z_{e_2} - z'_{e_2})) \right. & \\ \qquad \left. - \cos(k_+(z_{e_2} + z'_{e_2} - \ell_2)) \right] & \text{if } e = e_2 \text{ and } e' = e_2. \end{cases} \tag{111}$$

Where $\alpha = \frac{2e^{ik_+\ell_2}}{(e^{ik_+\ell_2} - 1)(e^{ik_+\ell_2} - 3)}$. The real component of the Green's function is plotted for each case in Figure 16 a) and b).

Having now derived a closed form expression for the Green's function of both a closed and open finite quantum graph, we now extend this formalism to consider periodic quantum graphs.

3.5 Green's Function of a Periodic Quantum Graph

As early as the 1880s, the properties of periodic systems were explored in the works of Lord Rayleigh and Lord Kelvin. Rayleigh's analysis of random walks and small vibrations, along with Kelvin's observations on wave propagation in diatomic lattices, laid the foundation for understanding the properties of periodic media. While Green's functions were not formalized in their work, their insights laid the groundwork for the mathematical tools that would later emerge. It was not until the mid-20th century that lattice Green's functions became integral to the study of lattice vibrations (see [244, 245] and the references therein). In these works, Maradudin et al. made significant contributions by using Green's functions to analyze the effects of point defects on lattice vibrations. These investigations revealed localized and resonance modes that critically influence material properties [245].

A critical step in defining Green's functions on a lattice involves the use of lattice sums, which represent summations over the periodic structure of the lattice. These sums encode the geometric and topological information of the lattice, playing a pivotal role in calculating Green's functions for periodic systems. Watson's integrals, developed in a broader context of mathematical physics, were later adapted to lattice problems by Glasser and Zucker [246], who provided exact expressions for these lattice sums. Their work offered a framework for evaluating properties of square lattices, enabling precise calculations of lattice transport properties. While these summations facilitate the determination of a lattice's Green's function, they often involve integrals that become challenging to solve, particularly in higher-dimensional problems or for complex lattice geometries. To address these challenges, various methodologies have been developed to enhance computational efficiency. Notably, Martinsson et al. [247] derived asymptotic expansions for Green's functions in lattices. Additional work by Linton employed techniques such as Ewald's method to transform slowly convergent series into computationally viable forms, thereby en-

abling the practical application of Green's functions in complex periodic systems [248].

These methodologies for determining the Green's function of a lattice have been applied to a wide range of lattice configurations and operators. Examples include applications in electromagnetics [249], waveguide problems, diffraction by periodic structures, and the analysis of phononic band gaps [250, 251].

The key methodology relevant to this work constructs the Green's function of the lattice from the periodic Green's function via a Fourier transform [252]. This approach is widely used in the literature but has been typically applied to lattice vibrations governed by a discrete Laplacian operator at each unit cell, akin to a spring-mass model. Unlike the existing literature, the quantum graph formalism developed here considers the full Laplacian operator acting on the finite bond domain that couples lattice sites. This approach allows for excitations on the lattice bonds themselves, providing a richer and more versatile representation of wave dynamics in lattice systems. This formalism offers unique insights compared to traditional methods by capturing additional dynamic behaviors intrinsic to the bonds. To the best of our knowledge this work presents the Green's function of a periodic quantum graph for the first time.

This method applies to any lattice topology, but for this work, we consider the square periodic graph with edge metric equal to the lattice period, $\ell_x = \ell_y = \ell$, as discussed in Sections 2.4.1 and 2.4.3. The vertex boundary conditions are considered arbitrary and are represented by the scattering matrix $\mathbf{\Sigma}^{(1)}(k)$, as defined in Section 2.1. We consider a point of excitation at an arbitrary vertex $\boldsymbol{R}' = (n'\ell, m'\ell)^T$ in direction e', where $e' \in \{l, r, d, u\}$. While the graph is translationally symmetric, we keep the excitation point variable to address future applications involving lattices with boundaries.

The Green function $\tilde{G}$ of the periodic quantum graph satisfies the inhomogeneous

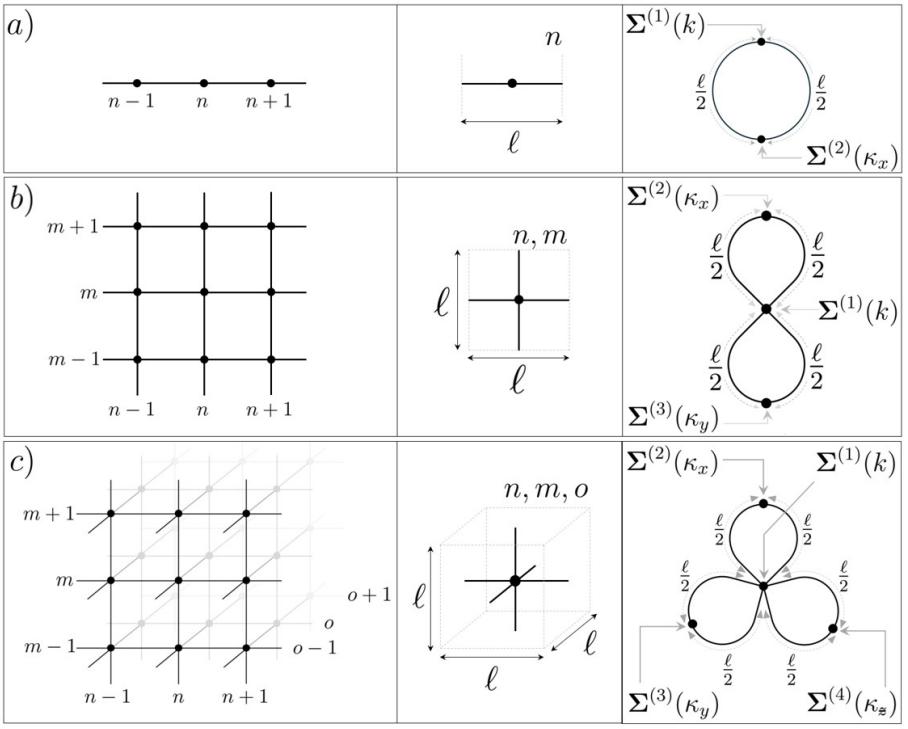

Figure 17: a) Left: Illustrates the neighborhood of a vertex within a 1D periodic quantum graph. Middle: Shows the unit cell of length ℓ at some arbitrary location n, serving as the building block of the lattice. Right: An auxiliary finite quantum graph is formed from the unit cell, with a spectrum equivalent to that of the infinite system, modeled via the addition of a phase matrix $\mathbf{\Sigma}^{(2)}(\kappa_x)$. b) Equivalent construction for a lattice in 2D, where the finite auxiliary quantum graph contains two phase matrices, $\mathbf{\Sigma}^{(2)}(\kappa_x)$ and $\mathbf{\Sigma}^{(3)}(\kappa_y)$. c) Equivalent construction for a lattice in 3D, where the finite auxiliary quantum graph contains three phase matrices, $\mathbf{\Sigma}^{(2)}(\kappa_x)$, $\mathbf{\Sigma}^{(3)}(\kappa_y)$, and $\mathbf{\Sigma}^{(4)}(\kappa_{\text{⋕}})$.

differential equation:

$$\left(\frac{d^2}{dz_{nm,e}^2} + E\right)\tilde{G}(z_{nm,e}, z'_{n'm',e'}; k) = \delta(z_{nm,e} - z'_{n'm',e'}). \tag{112}$$

In the methodology for finite quantum graphs, we introduced an auxiliary graph by cutting the excited edge e' and treating it as a pair of leads. This allows one

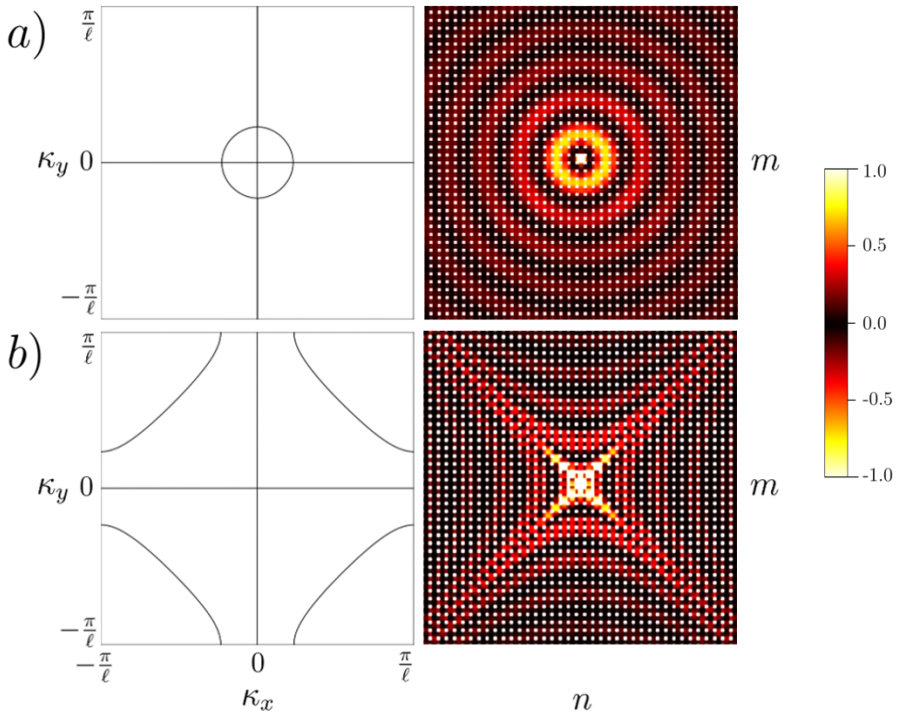

Figure 18: a) Shows a top-down view of the real component of the Green's function for $k = 0.5/\ell$, along with the equivalent iso-frequency contour. b) Shows a top-down view of the real component of the Green's function for $k = 1.7/\ell$ with the equivalent iso-frequency contour.

to derive the Green function G in a closed form through the inversion of a $2N_{\mathcal{B}}$ dimensional matrix, as seen in equation (79). For an infinite lattice, however, this approach would require inverting an infinite-dimensional matrix. To avoid this, we consider the periodic Green function of the lattice, which defines the wave response to periodic excitation, and via Fourier transform, construct the Green function of the graph. The periodic Green function satisfies the equation,

$$\left(\frac{d^2}{dz_{nm,e}^2} + E\right) G(z_{nm,e}, {z'}_{nm,e'}, \boldsymbol{\kappa}; k) = \delta(z_{nm,e} - z'_{nm,e'}), \tag{113}$$

where the point of excitation e' exists in every unit cell nm. To determine the periodic Green function, we again construct an auxiliary finite closed graph with a spectrum equivalent to that of the infinite lattice, as illustrated in Figure 17 for a

1D, 2D and 3D square periodic graph. Here, the Bloch decomposition is modeled via the introduction of vertex scattering vertices $\mathbf{\Sigma}^{(v)}(\kappa_j)$ that take account of the Bloch phase accumulated by a wave traveling throughout the lattice in direction j. Here,

$$\mathbf{\Sigma}^{(v)}(\kappa_j) = \begin{pmatrix} \mathrm{e}^{i\kappa_j \ell} & 0 \\ 0 & \mathrm{e}^{-i\kappa_j \ell} \end{pmatrix}. \tag{114}$$

Note the difference in sign, which defines waves traveling in the increasing $(+)$ or decreasing $(-)$ j-direction. As in Chapter 2.2 the graph scattering matrix is then given by a diagonal block matrix formed of each vertex scatterer. Explicitly,

$$\mathbf{\Sigma} = \mathbf{\Pi} \begin{pmatrix} \mathbf{\Sigma}^{(1)}(k) & 0 & 0 & \dots \\ 0 & \mathbf{\Sigma}^{(2)}(\kappa_x) & 0 & \dots \\ 0 & 0 & \mathbf{\Sigma}^{(3)}(\kappa_y) & \dots \\ \vdots & \vdots & \vdots & \ddots \end{pmatrix} = \mathbf{\Pi}\, \hat{\mathbf{\Sigma}}, \tag{115}$$

where $\mathbf{\Pi}$ is a permutation matrix that orders the matrix elements correctly. The phase information accumulated as waves travel between vertices is given by the matrix $\boldsymbol{P}(k)$, with elements vv' given by,

$$[\mathbf{P}(k)]_{vv'} = \begin{cases} e^{ik\ell/2}, & \text{if vertex } v \text{ and } v' \text{ are connected,} \\ 0, & \text{otherwise.} \end{cases} \tag{116}$$

The quantum map of the auxiliary graph is constructed by multiplying equations (116) and (115) as,

$$\boldsymbol{U}(k, \kappa_x, \kappa_y) = \boldsymbol{P}(k)\mathbf{\Sigma}(k, \kappa_x, \kappa_y). \tag{117}$$

Having determined the quantum map of the auxiliary compact quantum graph with equivalent lattice spectrum, we determine Green's function G by substitution of equation (117) into equation (79). The Green function of the periodic quantum graph $\tilde{G}$ is then obtained by performing a Fourier transform on both sides of equation

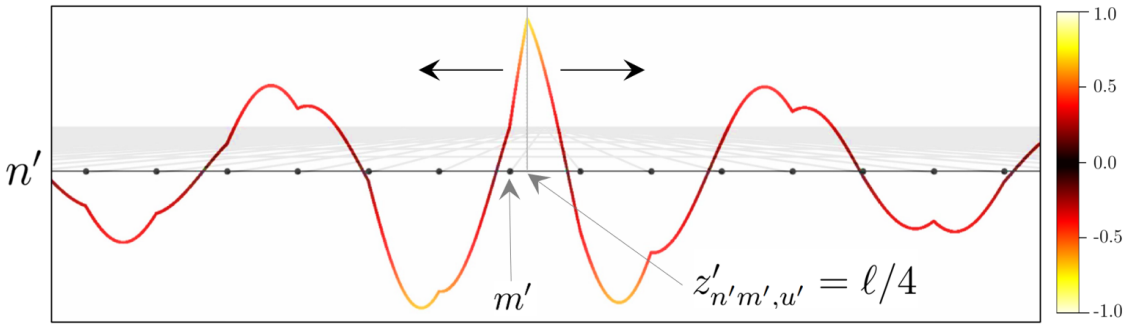

Figure 19: Shows the real component of the Green function in a cross-section of all m at location n' around the point of excitation at vertex m' with coordinate $z'_{n'm',u'} = \ell/4$.

(113), which naturally gives,

$$\tilde{G}_{nm}(z_{nm,e}, z_{n'm',e'}, k) = \left(\frac{\ell}{2\pi}\right)^2 \int_{-\frac{\pi}{\ell}}^{\frac{\pi}{\ell}} \int_{-\frac{\pi}{\ell}}^{\frac{\pi}{\ell}} \mathrm{e}^{i\boldsymbol{\kappa}\cdot(\boldsymbol{R}-\boldsymbol{R}')} G(\mathbf{z}, \mathbf{z}', \boldsymbol{\kappa}; k) d\kappa_x d\kappa_y. \tag{118}$$

This integral sums over all possible Bloch phases, thus reconstructing the Green function for the infinite lattice from its finite counterpart.

Figure 19 shows a cross section of the quantum graph at the point of excitation with the real component of Green's function plotted. Of key interest is the asymmetry of the Green function that is a consequence of the point of excitation on the edge not being symmetrical. This is a unique consequence of the graph topology, which is not found in other lattice models, such as the spring mass model [252]. Additionally in Figure 18 we show a top down view of the real component of the Green function for both $k = 0.5/\ell$ and $k = 1.7/\ell$. As one would expect the solution in the long wavelength regime, where the graphs wave properties are circularly disipitive, we restore solutions reminiscent of the Hankel function that describes the free space Green's function in 2D [235]. As the frequency is then changed to $k = 1.7/\ell$ we see the square periodic mesh topology present in the wave field, as high wave calumniation appears for all diagonal directions.

3.6 Chapter Summary

We present a simple three-step procedure for generating the Green's function on both closed and open finite quantum graphs. The procedure exploits the standard scattering approach, wherein the infinite sum of trajectories between a given source point and a receiver point on the graph involves the inverse of a block component of the matrix that defines the graph's quantum map. Generally, this matrix is sub-unitary, and its inverse is well-defined. Using this scattering representation, a closed-form expression for the Green's function is provided here for the first time.

We also discuss the possibility of perfect scars and bound states in the continuum, which cause divergence in existing trajectory-based approaches. We demonstrate that our closed-form expressions can be regularized in these cases. This regularization scheme is important on a practical level, as scattering matrices of generic quantum graphs with Kirchhoff-Neumann matching conditions may have resonances that are arbitrarily close to bound states, even if they do not possess exact bound states. If not treated with care, these resonances can lead to significant errors in numerical investigations.

After thoroughly investigating the scattering conditions in both closed and open finite quantum graphs, we extend the formalism to periodic quantum graphs by introducing an equivalent closed auxiliary graph with imposed scattering matrices that yield an equivalent lattice spectrum. The solutions of the finite graph were then determined via the proposed three-step procedure, resulting in the periodic Green's function. Through a Fourier transform, this produced the desired lattice Green's function. We show through examples that the Green's function can be asymmetric due to the underlying graph topology. Moreover, in the long-wavelength regime, the solutions closely resemble those of the Hankel function, which describes the free-space Green's function in 2D. With this we have developed the scattering language of quantum graph theory to a point where we may apply it to the study of

metamaterials. In the following, we consider both theoretically and experimentally a quantum graph approach to metamaterial design.

4 Modeling Metamaterials on Quantum Graphs: Theory and Experiment

In this chapter, we present and build on two works by Lawrie et al. [253, 254] that use quantum graph theory to model metamaterials. The first study [253] develops a theoretical scattering framework for periodic layered quantum graphs as a model for a 2D metamaterial, demonstrating phenomena such as positive and negative refraction, total internal reflection, and beam steering. The second study [254] validates this model to a high accuracy in the acoustic regime through both numerical simulations and experiment.

4.1 Motivation

A key motivation for this chapter arises from the work of Veselago [4] and Pendry [5], discussed in Chapter 1.1. Their studies on materials with a negative (effective) refractive index showed that waves can possess anti-parallel phase and group velocities, leading to effects such as the reversal of Snell's law. Pendry's work also proposed the concept of a perfect lens, capable of focusing light beyond the diffraction limit. These ideas inspired extensive research into modeling and designing metamaterials, as discussed in Section 1.2, with various techniques presenting both advantages and challenges.

In previous chapters, we developed the scattering formalism of quantum graph theory for finite closed, open, and infinite periodic quantum graphs, and formulated the Green's function for quantum graphs in a closed form. We extended this formalism to infinite periodic quantum graphs, where the mesh Green's function resembled free-space solutions in the long-wavelength regime. By varying the vertex scattering properties, spectral gaps could be engineered, aligning with the findings of Kuchment et al. [211]. These results demonstrate that the wave properties of a graph are

inherently influenced by its topology and boundary conditions. Building on this foundation, we now apply quantum graph theory to the modeling of metamaterials, with the goal of engineering wave transport properties such as negative refraction within these complex structures.

We begin by considering the eigen-spectrum of a trivially connected square periodic quantum graph as a representation of free space, as discussed in Section 2.4. This serves as a baseline model from which more intricate behaviors can be engineered. By altering the edge metrics to represent space-coiled waveguides [255], we introduce anisotropic properties into the system, thereby modifying the relationship between phase and group velocities.

These changes in material properties are demonstrated by the scattering of a Gaussian beam incident on an interface between two semi-infinite quantum graphs with different edge metrics. We demonstrate positive and negative refraction as well as total internal reflection. This framework also allows us to explore beam steering across multiple layers of metamaterials using the Transfer Matrix Method.

To validate these findings, we consider the graph wave function as an acoustic pressure field, with the graph's edges modeling thin tubes through which the acoustic waves propagate. This analogy closely maps to the networks of interconnected waveguides commonly found in acoustic metamaterials [256]. We examine the properties of these networks using numerical simulations in COMSOL Multiphysics [254] and experimental measurements of the pressure field within a network of interconnected thin tubes. The validity of the quantum graph approach is confirmed through comparison with numerical and experimental results. We show a clear agreement between the quantum graph model and COMSOL simulations, particularly below the cut-off frequency. Furthermore, these properties are experimentally verified with high accuracy, emphasising the robustness of quantum graph theory as a design tool for metamaterials.

This chapter is structured as follows: Section 4.2 provides a brief overview of the scattering formulation for periodic quantum graphs, and shows the relationship between wave group and phase velocity as a function of graph edge metric. Negative refraction is shown and the group velocity is investigated in terms of edge flux in Section 4.3. To demonstrate both group and phase properties of a graph, Gaussian beams are constructed in Section 4.4. In Section 4.6, we explore boundary problems involving interfaces between two metamaterials, where the graph material properties are demonstrated in terms of the scattering profiles of incident Gaussian beams on the interface. Section 4.6.1 extends this formalism to N-layered metamaterials using the Transfer Matrix Method, showcasing beam steering across three-layered structures. Finally, Sections 4.7 assess the validity of the quantum graph approach through numerical simulations and experiment in the acoustic regime.

4.2 Mesh Solutions - A Recap

In order to construct solutions on a lattice as a model for a metamaterial, let us briefly recap the key equations derived in Section 2.4 for modeling plane waves on periodic quantum graphs. Plane waves on periodic quantum graphs are described by the following system of equations:

$$\boldsymbol{\psi}_{nm} = e^{i(\kappa_x n + \kappa_y m)\ell} \left[e^{ik\hat{z}} \boldsymbol{\Sigma} + e^{-ik\hat{z}} \mathbb{I} \right] \mathbf{a}^{\text{in}} \tag{119}$$

Here, $\boldsymbol{\psi}_{nm} = (\psi_{nm,l}, \psi_{nm,r}, \psi_{nm,d}, \psi_{nm,u})^T$ is the vector of edge solutions to the left(l), right(r), down(d), and up(u) of vertex nm. The edge phase is given by $\hat{z} = \text{diag}(z_l, z_r, z_d, z_u)$, which is a diagonal matrix of local edge coordinates, with $z_e \in [0, \ell_e]$, where ℓ_e is the metric of edge e within the star of the vertex $\mathcal{S} = \{l, r, d, u\}$. The vertex scattering matrix $\boldsymbol{\Sigma}$ fixes the boundary conditions, which we

set to be Kirchhoff-Neumann as in equation (120),

$$\mathbf{\Sigma}_{pq} = \frac{1}{2} - \delta_{pq}. \tag{120}$$

The vector $\mathbf{a}^{\text{in}} = (a_l^{\text{in}}, a_r^{\text{in}}, a_d^{\text{in}}, a_u^{\text{in}})^T$ represents the incoming wave amplitudes at a vertex within the lattice, given as the eigenvector of the graph quantum map as in equation (55). Finally the lattice or "crystal" phase is given by $e^{i(\kappa_x n + \kappa_y m)\ell}$ where the relationship between the horizontal and vertical Bloch momentum κ_x and κ_y is given by the secular equation of the quantum map as in equation (56). For a simply connected square periodic quantum graph where the edge metric $\boldsymbol{\mathcal{L}} = \{\ell_x, \ell_x, \ell_y, \ell_y\}$ is equal to the vertex period $\ell_x = \ell_y = \ell$, we define the relationship as,

$$\kappa_x(k, \kappa_y) = \pm\frac{1}{\ell}\arccos(2\cos(k\ell) - \cos(\kappa_y\ell)). \tag{121}$$

This space of solutions can be thought of as "free space" in the long wavelength regime as discussed in section 2.4 and shown in Figure 11 with a given solution within the BZ being demonstrated in a plane wave representation in Figure 12. As will become apparent, the direction of phase and group, as defined by the flux, do not necessarily have to be in parallel. To investigate this further, let us formulate the relationship between group and phase in the following.

4.3 Phase and Flux

The phase of the resulting eigenfunction is determined by the chosen Bloch wave vector $\boldsymbol{\kappa} = (\kappa_x, \kappa_y)^T$, while the energy flow is given by the Poynting vector $\boldsymbol{J} = (J_x, J_y)^T$, which is normal to the iso-frequency contour. To explicitly construct the components of $\boldsymbol{J}$, we evaluate the flux on the graph edges. The 1D flux J of the

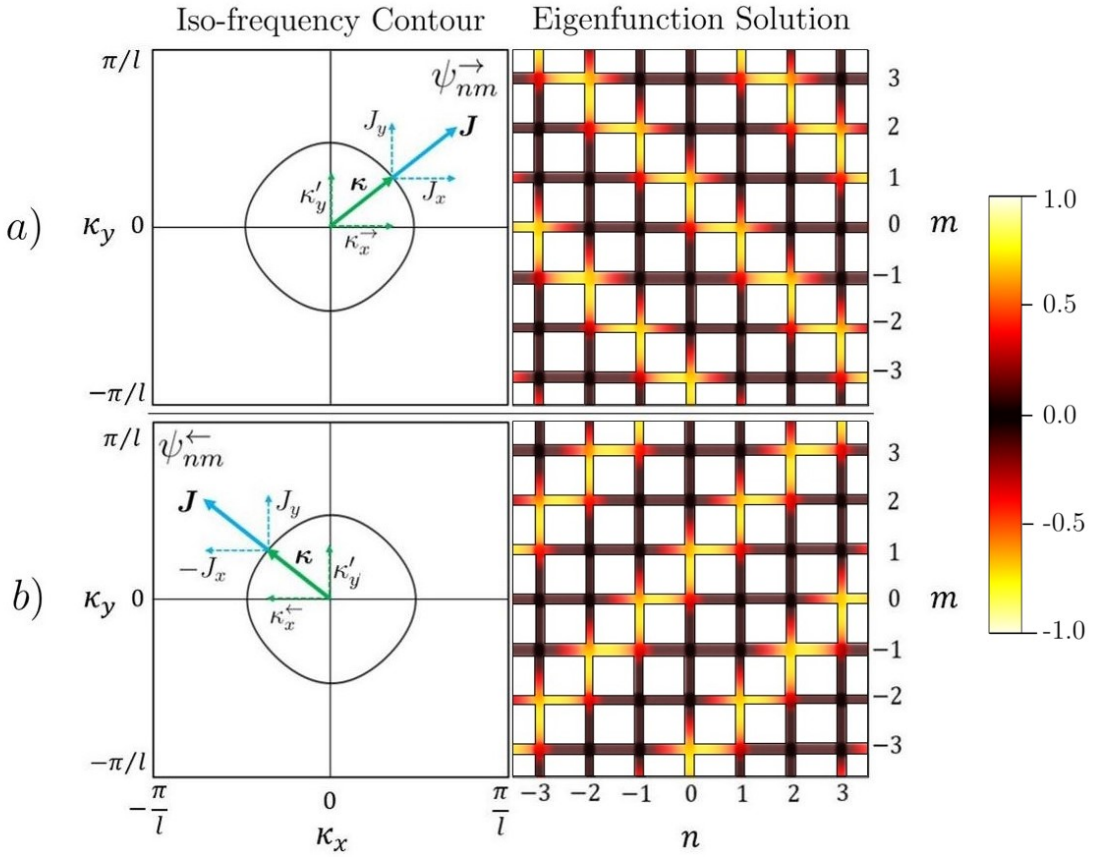

Figure 20: Iso-frequency contour of Figure 11b) at $k = \frac{1}{\ell}$ with possible wave vectors $\boldsymbol{\kappa} = (\kappa_x^{\rightarrow}, \kappa'_y)^T = (\frac{1}{\ell}, \frac{1}{\ell})^T$ in a) and $\boldsymbol{\kappa} = (\kappa_x^{\leftarrow}, \kappa'_y)^T = (-\frac{1}{\ell}, \frac{1}{\ell})^T$ in b), both shown in green, with the corresponding Poynting vector $\boldsymbol{J} = (J_x, J_y)^T$ and $\boldsymbol{J} = (-J_x, J_y)^T$ normal to the contour shown in blue. The resulting real components of the eigenfunction solutions $\psi^{\rightleftarrows}_{nm,e}(z_e; k, \kappa_x^{\rightleftarrows}, \kappa_y)$ for the wave vectors used in a) and b) are also shown.

wave function $\psi_{nm,e}$ is given by:

$$J(\psi_{nm,e}(z_e)) := \Re\left(\bar{\psi}_{nm,e}(z_e)\frac{1}{i}\frac{\partial\psi_{nm,e}(z_e)}{\partial z_e}\right) = k(|a_e^{\text{out}}|^2 - |a_e^{\text{in}}|^2), \tag{122}$$

where $\bar{\psi}$ denotes the complex conjugate of ψ. The horizontal and vertical components of the Poynting vector can then be evaluated in terms of the waves on edges

right (r) (or left (l)) and up (u) (or down (d)), respectively:

$$\boldsymbol{J} = \begin{pmatrix} J_x \\ J_y \end{pmatrix} := k \begin{pmatrix} |a_r^{\text{out}}|^2 - |a_r^{\text{in}}|^2 \\ |a_u^{\text{out}}|^2 - |a_u^{\text{in}}|^2 \end{pmatrix} \equiv k \begin{pmatrix} |a_l^{\text{in}}|^2 - |a_l^{\text{out}}|^2 \\ |a_d^{\text{in}}|^2 - |a_d^{\text{out}}|^2 \end{pmatrix}. \tag{123}$$

This equivalence condition between the flux to the left and right of the vertex and the flux to the down and up of the vertex is a property of the underlying Bloch waves basis that states the solutions in the neighborhood of the vertex, can be expressed in terms of one another, as in the system of equations in (50).

In the example shown in Figure 12, for each value of κ_y, there are two corresponding values of κ_x. The choice of κ_x determines the direction of energy flow. To distinguish between waves traveling in opposite horizontal directions, we introduce the following notation: eigenfunction solutions with a Poynting vector heading to the right are indexed with $\rightarrow$, while those with a Poynting vector heading to the left are indexed with $\leftarrow$. Explicitly:

$$\begin{cases} \psi_{nm}^{\rightarrow}(z_e; k, \kappa_y) = \mathrm{e}^{i(\kappa_x^{\rightarrow} n + \kappa_y m)} \left(a_e^{\rightarrow,\text{out}} \mathrm{e}^{ikz_e} + a_e^{\rightarrow,\text{in}} \mathrm{e}^{-ikz_e} \right), & J_x > 0, \\ \psi_{nm}^{\leftarrow}(z_e; k, \kappa_y) = \mathrm{e}^{i(\kappa_x^{\leftarrow} n + \kappa_y m)} \left(a_e^{\leftarrow,\text{out}} \mathrm{e}^{ikz_e} + a_e^{\leftarrow,\text{in}} \mathrm{e}^{-ikz_e} \right), & J_x < 0. \end{cases} \tag{124}$$

Choosing the value of κ_x ($\kappa_x^{\rightarrow}$ or $\kappa_x^{\leftarrow}$) thus inherently determines the wave direction. For this reason, the κ_x dependence is omitted in the final notation of the eigenfunctions.

4.4 Constructing Gaussian Beams

As was formulated above, plane wave solutions travel in the direction of the wave vector $\boldsymbol{\kappa}$, which does not necessarily agree with the direction of energy flow given by the Poynting vector $\boldsymbol{J}$ in (123). This can be observed when considering Gaussian beam solutions constructed via Fourier series with the eigenfunctions, shown above,

as a basis. The solution of the Gaussian beam with focal point at $n = n'$, expressed in components $\mathbf{\Phi}_{nm}(z) = (\Phi_{nm,l}(z), \Phi_{nm,r}(z), \Phi_{nm,d}(z), \Phi_{nm,u}(z))^T$, is given as,

$$\mathbf{\Phi}_{nm}(z;k) = \frac{1}{\sqrt{2\pi}} \int_{\Omega} \alpha_{n'}(\kappa_y;k) \boldsymbol{\psi}^{\rightarrow}_{nm}(z,\kappa_y;k) d\kappa_y, \tag{125}$$

where the integral is performed over the domain $\Omega = \Omega(k)$ of the iso-frequency contour. Solutions outside Ω are evanescent and so contribute nothing in the far field. The expansion coefficients $\alpha_{n'}$ describing the beam profile at the focal point in terms of the eigenfunctions, given by the inverse transform,

$$\alpha_{n'}(\kappa_y;k) = \frac{1}{\sqrt{2\pi}} \sum_{m=-\infty}^{\infty} \left\{ \int_0^l \bar{\psi}^{\rightarrow}_{n'm,u}(z,\kappa_y;k) \Phi_{n'm,u}(z;\kappa_y) dz \right\}. \tag{126}$$

Here, $\bar{\psi}^{\rightarrow}_{n'm,u}$ is the complex conjugate of the right moving eigenfunction expressed for all m at horizontal location $n = n'$ along the upward edges u and $\Phi_{n'm,u}(z)$ is the beam profile for all m with focal point $n = n'$ expressed on edge u. We choose the beam profile to be Gaussian, such that

$$\Phi_{n'm,u}(z) = \frac{1}{\sqrt{\sigma\sqrt{\pi}}} e^{-\left(\frac{z+ml}{\sqrt{2}\sigma}\right)^2} e^{i\kappa'_y l}, \tag{127}$$

where σ is the width of the beam and the phase $e^{i\kappa'_y l}$ determines the tilt angle of the beam with respect to the horizontal axis of the lattice. Since the space on the graph is discretised, so too are the integrals. Figure 21 illustrates how varying the parameters σ and κ'_y affects the shape and direction of the resulting Gaussian beam for a given iso-frequency contour $\Omega(k)$.

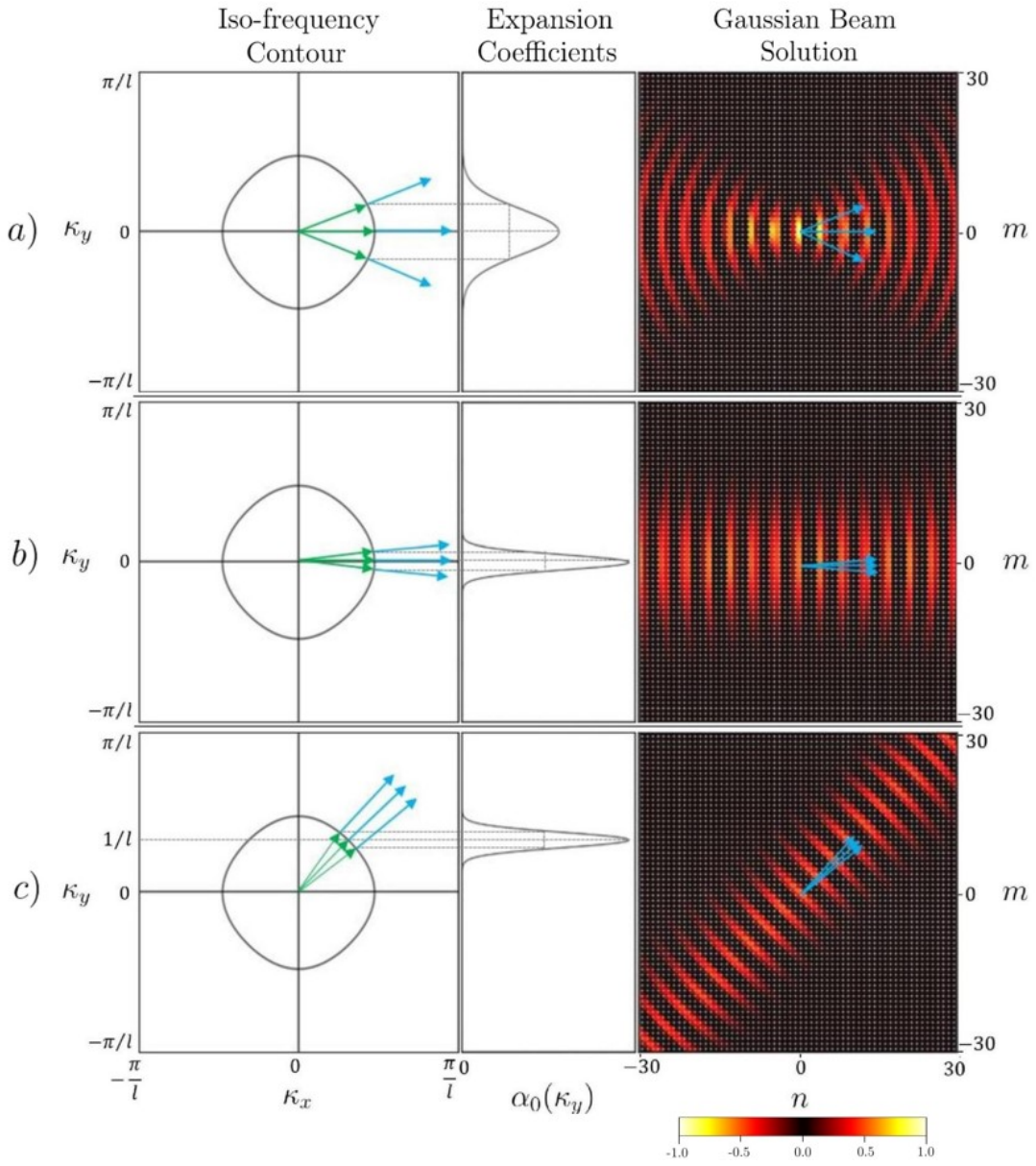

Figure 21: Iso-frequency contour for a square periodic quantum graph with equivilent edge lengths $\ell = \ell_x = \ell_y$ and Kirchhoff-Neumann vertex boundary conditions. The frequency is set at $k = 1/l$ together with the expansion coefficients $\alpha_{n'=0}$ in equation (126) and the resulting real components of the Gaussian beam profile $\mathbf{\Phi}_{nm}$ with focal point set to $n' = 0$. The beam profiles, equation (127), shown here are characterised by the parameters $\kappa'_y = 0$, 0 and $1/l$ and beam widths $\sigma = 2.2l$, $6.6l$ and $6.6l$ for a), b) and c), respectively.

4.5 Engineering Negative Refraction

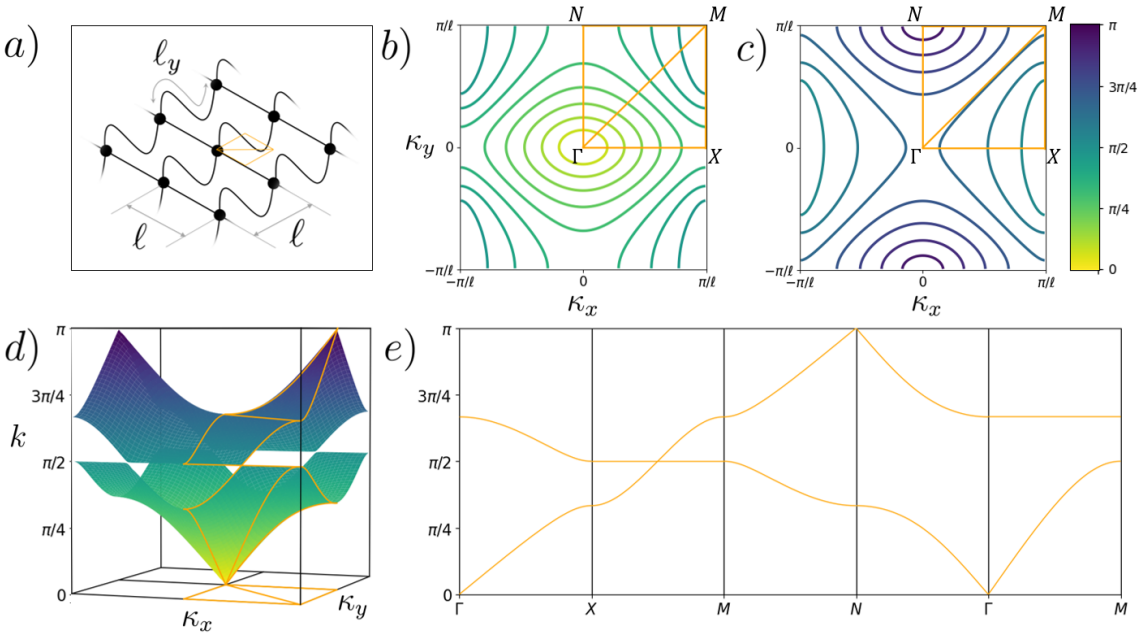

Figure 22: a) Illustrates the neighbourhood of a given vertex within a 2D square periodic quantum graph with period ℓ, with a vertex decoration formed of a single edge of length $\ell_{res} = 1$. b) shows a contour plot of the first band within the Brillouin Zone with the points of symmetry Γ, X, N, M labeled and connected by an orange line. c) shows the contour plot of the second band. d) shows the band diagram over a frequency domain of $k \in [0, \pi/\ell]$. e) shows the momentum solutions between the points of symmetry within the BZ as well as a bandgap highlighted in blue.

In this section we demonstrate non-resonant negative refraction by manipulating the underlying graph edge metric, rather than the vertex scattering matrix - as in section 2.4. Each vertex is connected horizontally and vertically by finite edges to the left(l), right(r), down(d) and up(u) of the vertex, with metric $\mathcal{L} = \{\ell_x, \ell_x, \ell_y, \ell_y\}$. Here we consider the properties of a lattice where the edge metric is not equal to the lattice period, $\ell_x \neq \ell_y \neq \ell$, such that the waves can accumulate an arbitrary phase when propagating between vertices - See Figure 22 a). The edges within the star of the vertex $e \in \mathcal{S}$ are given a local edge coordinate that exist within the domains

$z_l \in [0, \ell_x]$, $z_r \in [0, \ell_x]$, $z_d \in [0, \ell_y]$ and $z_u \in [0, \ell_y]$, with $z_e = 0$ at the vertex. For this construction the dispersive properties of the graph are given by solving the secular equation (56) which gives,

$$\sin(k(\ell_x + \ell_y)) = \sin(k\ell_y)\cos(\kappa_x \ell) + \sin(k\ell_x)\cos(\kappa_y \ell), \tag{128}$$

Here the horizontal and vertical edge lengths ℓ_x and ℓ_y represent free variables that allow us to engineer the graphs disipitive properties. Key to this formulation that separates it from previous lattice configurations (as in Figure 11 and 14) is the freedom to break the rotational symmetry of the lattice by independently varying ℓ_x and ℓ_y. This is equivalent to varying the wave speed on a given edge as for a wave to travel throughout the lattice, it now has to travel a larger distance to cover the same number of lattice points. Naturally this leads to a large difference between the group and phase velocities of a solutions within the lattice leading in some cases to hyperbolic dispersion curves, as illustrated in by the second band in Figure 22 c) and d). At frequencies within the second band, clear anti-parallel phase and group velocity is observed, as described by Pendry and Veselago [5, 4]. To demonstrate these engineered properties, let us consider the scattering profile of an incident Gaussian beam on a metamaterial that posses the wave properties of anti-parallel phase and group velocity.

4.6 Modeling Metamaterial Interfaces

To exemplify the engineered refractive properties, consider two semi-infinite square periodic quantum graphs connected to span the infinite domain where each graph has variable edge lengths as illustrated in Figure 23. The two materials are connected along the y direction and material 1 exists for the set of unit cells $\boldsymbol{\mathcal{N}}_1 = (-\infty, ..., -2, -1\}$ and material 2 exists for the set of unit cells $\boldsymbol{\mathcal{N}}_2 = \{0, 1, ..., \infty)$. The full wave solution $\boldsymbol{\Psi}_{nm} = (\Psi_{nm,l}, \Psi_{nm,r}, \Psi_{nm,d}, \Psi_{nm,u})^T$ across the two materials

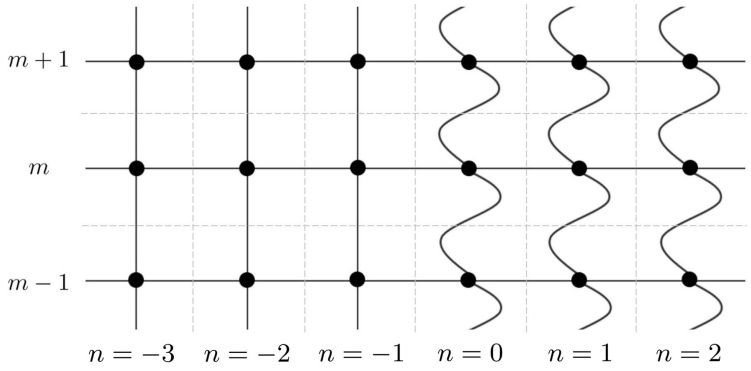

Figure 23: Illustrates two semi-infinite square periodic quantum graphs connected at an interface between $n = 0$ and $n = 1$. The right graph has hyperbolic dispersive properties given by the anisotropy of edge metric as defined by equation 128.

can be constructed by a linear superposition of counter propagating eigenfunction solutions $\boldsymbol{\psi}^{\rightleftharpoons}_{j,nm}$ in material $j = 1$ and 2, as expressed in equation (124), that is,

$$\begin{aligned}\boldsymbol{\Psi}_{nm}(z,\kappa_y;k) =& H_1(n)\left[A_1(\kappa_y;k)\boldsymbol{\psi}^{\rightarrow}_{1,nm}(z,\kappa_y;k) + B_1(\kappa_y;k)\boldsymbol{\psi}^{\leftarrow}_{1,nm}(z,\kappa_y;k)\right] + \\ & H_2(n)\left[A_2(\kappa_y;k)\boldsymbol{\psi}^{\rightarrow}_{2,nm}(z,\kappa_y;k) + B_2(\kappa_y;k)\boldsymbol{\psi}^{\leftarrow}_{2,nm}(z,\kappa_y;k)\right],\end{aligned} \tag{129}$$

where $H_j(n)$ is a discrete top hat function, that gives,

$$H_j(n) = \begin{cases} 1, & \forall n \in \boldsymbol{\mathcal{N}}_j \\ 0, & \forall n \notin \boldsymbol{\mathcal{N}}_j \end{cases} \tag{130}$$

for $j = 1, 2$ and the coefficients A_j and B_j are associated with left and right moving waves, respectively. Thus, solutions with coefficients A_1 and B_2 represent waves incident on the interface, while solutions with coefficients B_1 and A_2 represent waves scattered from the interface. To determine the coefficients, we must satisfy the boundary conditions at the material interface. Naturally the wave solutions are given for a single value of k between the two materials enforcing $k_1 = k_2 = k$. As the system stays periodic in the y direction, the Bloch phase tangential to the interface also remain constant across the interface leading to the boundary condition

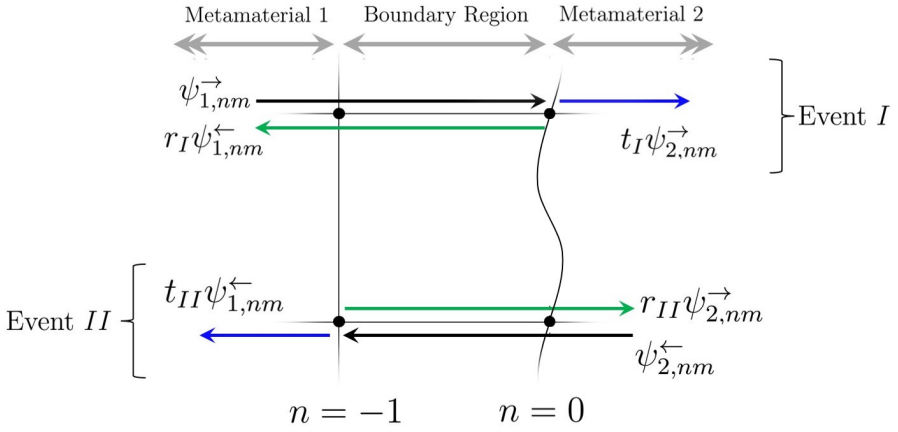

Figure 24: Boundary region between metamaterials 1 and 2, understood as all right(r) edges for $n=-1$ and all left (l) edges for $n=0$. Here, wave scattering from the boundary is divided into event I and II, where r_p and t_p represent reflection and transmission amplitudes for event $p=I$ or II.

$\kappa_{1,y}=\kappa_{2,y}=\kappa_y$. The remaining unknowns are then the wave vectors normal to the interface $\kappa^{\rightleftarrows}_{j,x}(k,\kappa_y)$ which is obtained from the dispersion curve for each material.

To determine the scattering coefficients A_j and B_j, we normalise the eigenfunction solutions of each material such that the magnitude of the horizontal flux of each component is equal given $\kappa^{\rightleftarrows}_{j,x}\in Re$, that is to say,

$$\begin{aligned} J(\psi^{\rightarrow}_{1,nm,l}) &= J(\psi^{\rightarrow}_{2,nm,l}) = 1 \\ J(\psi^{\leftarrow}_{1,nm,l}) &= J(\psi^{\leftarrow}_{2,nm,l}) = -1 \end{aligned}, \tag{131}$$

Equally, the same condition can be enforced on the right edges, r. With the scaling choice (131), flux conservation across the interface

$$J\left(A_1\psi^{\rightarrow}_{1,0m,l}+B_1\psi^{\leftarrow}_{1,0m,l}\right)=J\left(A_2\psi^{\rightarrow}_{2,0m,l}+B_2\psi^{\leftarrow}_{2,0m,l}\right) \tag{132}$$

reduces to

$$|A_1|^2+|B_2|^2=|B_1|^2+|A_2|^2 \tag{133}$$

and wave scattering at the interface can then be described in terms of a unitary scattering process. The corresponding interface scattering matrix $\boldsymbol{S}_{1,2}$ performing the mapping,

$$\begin{pmatrix} B_1 \\ A_2 \end{pmatrix} = \boldsymbol{S}_{1,2} \begin{pmatrix} A_1 \\ B_2 \end{pmatrix} \tag{134}$$

can then be constructed by decomposing the interface scattering into two events. Event I describes a wave incident from material 1 onto material 2 with amplitude $A_1 = 1$ and $B_2 = 0$, producing a reflected and transmitted wave with respective amplitudes r_I and t_I. Event II describes a wave incident from material 2 onto material 1 with amplitude $B_2 = 1$ and $A_1 = 0$, producing a reflected and transmitted wave with respective amplitudes r_{II} and t_{II}, see Figure 24. The interface scattering matrix takes on the form

$$\boldsymbol{S}_{1,2} = \begin{pmatrix} r_I & t_{II} \\ t_I & r_{II} \end{pmatrix}. \tag{135}$$

To evaluate the matrix elements, consider first event I. For simplicity we choose to evaluate the waves at location $n = 0$, at coordinate $z_l = 0$. Of course, the same condition can be evaluated anywhere on the boundary edge. Since the phase κ_y is the same in both materials, it is sufficient to evaluate the solutions at $m = 0$. Here,

$$\begin{aligned} \Psi_{(\forall n \leq -1)0,l}(0)|_{n=0} &= \left(a_{1,l}^{\rightarrow,\text{out}} + a_{1,l}^{\rightarrow,\text{in}}\right) + r_I \left(a_{1,l}^{\leftarrow,\text{out}} + a_{1,l}^{\leftarrow,\text{in}}\right) \\ \Psi_{(\forall n \geq 0)0,l}(0)|_{n=0} &= t_I \left(a_{2,l}^{\rightarrow,\text{out}} + a_{2,l}^{\rightarrow,\text{in}}\right). \end{aligned} \tag{136}$$

$\Psi_{(\forall n \leq -1)0,l}(0)|_{n=0}$ and $\Psi_{(\forall n \geq 0)0,l}(0)|_{n=0}$ both exist on the same edge in the boundary region, so to stay consistent, there must be an equivalence between the incoming and outgoing wave amplitudes of these solutions, that is,

$$\begin{aligned} t_I a_{2,l}^{\rightarrow,\text{out}} &= a_{1,l}^{\rightarrow,\text{out}} + r_I a_{1,l}^{\leftarrow,\text{out}} \\ t_I a_{2,l}^{\rightarrow,\text{in}} &= a_{1,l}^{\rightarrow,\text{in}} + r_I a_{1,l}^{\leftarrow,\text{in}}. \end{aligned} \tag{137}$$

This can be solved to give

$$\begin{aligned} r_I &= \frac{a_{2,l}^{\rightarrow,\text{out}} a_{1,l}^{\rightarrow,\text{in}} - a_{2,l}^{\rightarrow,\text{in}} a_{1,l}^{\rightarrow,\text{out}}}{a_{2,l}^{\rightarrow,\text{in}} a_{1,l}^{\leftarrow,\text{out}} - a_{1,l}^{\leftarrow,\text{in}} a_{2,l}^{\rightarrow,\text{out}}} \\ t_1 &= \frac{a_{1,l}^{\rightarrow,\text{in}} a_{1,l}^{\leftarrow,\text{out}} - a_{1,l}^{\leftarrow,\text{in}} a_{1,l}^{\rightarrow,\text{out}}}{a_{2,l}^{\rightarrow,\text{in}} a_{1,l}^{\leftarrow,\text{out}} - a_{1,l}^{\leftarrow,\text{in}} a_{2,l}^{\rightarrow,\text{out}}}. \end{aligned} \tag{138}$$

Exactly the same procedure can be done for event II where

$$\begin{aligned} \Psi_{(\forall n \leq -1)0,l}(0)|_{n=0} &= t_{II} \left(a_{1,l}^{\leftarrow,\text{out}} + a_{1,l}^{\leftarrow,\text{in}} \right) \\ \Psi_{(\forall n \geq 0)0,l}(0)|_{n=0} &= \left(a_{2,l}^{\leftarrow,\text{out}} + a_{2,l}^{\leftarrow,\text{in}} \right) + r_{II} \left(a_{2,l}^{\rightarrow,\text{out}} + a_{2,l}^{\rightarrow,\text{in}} \right), \end{aligned} \tag{139}$$

which yields the equivalence condition

$$\begin{aligned} t_{II} a_{1,l}^{\leftarrow,\text{out}} &= a_{2,l}^{\leftarrow,\text{out}} + r_{II} a_{2,l}^{\rightarrow,\text{out}} \\ t_{II} a_{1,l}^{\leftarrow,\text{in}} &= a_{2,l}^{\leftarrow,\text{in}} + r_{II} a_{2,l}^{\rightarrow,\text{in}} \end{aligned} \tag{140}$$

with solutions

$$\begin{aligned} r_{II} &= \frac{a_{1,l}^{\leftarrow,\text{out}} a_{2,l}^{\leftarrow,\text{in}} - a_{1,l}^{\leftarrow,\text{in}} a_{2,l}^{\leftarrow,\text{out}}}{a_{2,l}^{\rightarrow,\text{out}} a_{1,l}^{\leftarrow,\text{in}} - a_{2,l}^{\rightarrow,\text{in}} a_{1,l}^{\leftarrow,\text{out}}} \\ t_{II} &= \frac{a_{2,l}^{\rightarrow,\text{out}} a_{2,l}^{\leftarrow,\text{in}} - a_{2,l}^{\rightarrow,\text{in}} a_{2,l}^{\leftarrow,\text{out}}}{a_{2,l}^{\rightarrow,\text{out}} a_{1,l}^{\leftarrow,\text{in}} - a_{2,l}^{\rightarrow,\text{in}} a_{1,l}^{\leftarrow,\text{out}}}. \end{aligned} \tag{141}$$

The results of this unitary interface scattering is shown in Figure 25 for a Gaussian beam incident from material 1 with amplitude $A_1 = 1$ and no incident beam from material 2, that is, $B_2 = 0$. The Gaussian source point is set to $n' = -60$ and $m' = 0$, coming from the lower left of the figure. The beam solutions are constructed from the plane wave basis following the procedure in Section 4.4, where the wave function within the integrand of equation (125) is replaced by the incident and scattered field from equation (129). As before the solutions are plotted using the scatter plot outlined in section 2.4.2.

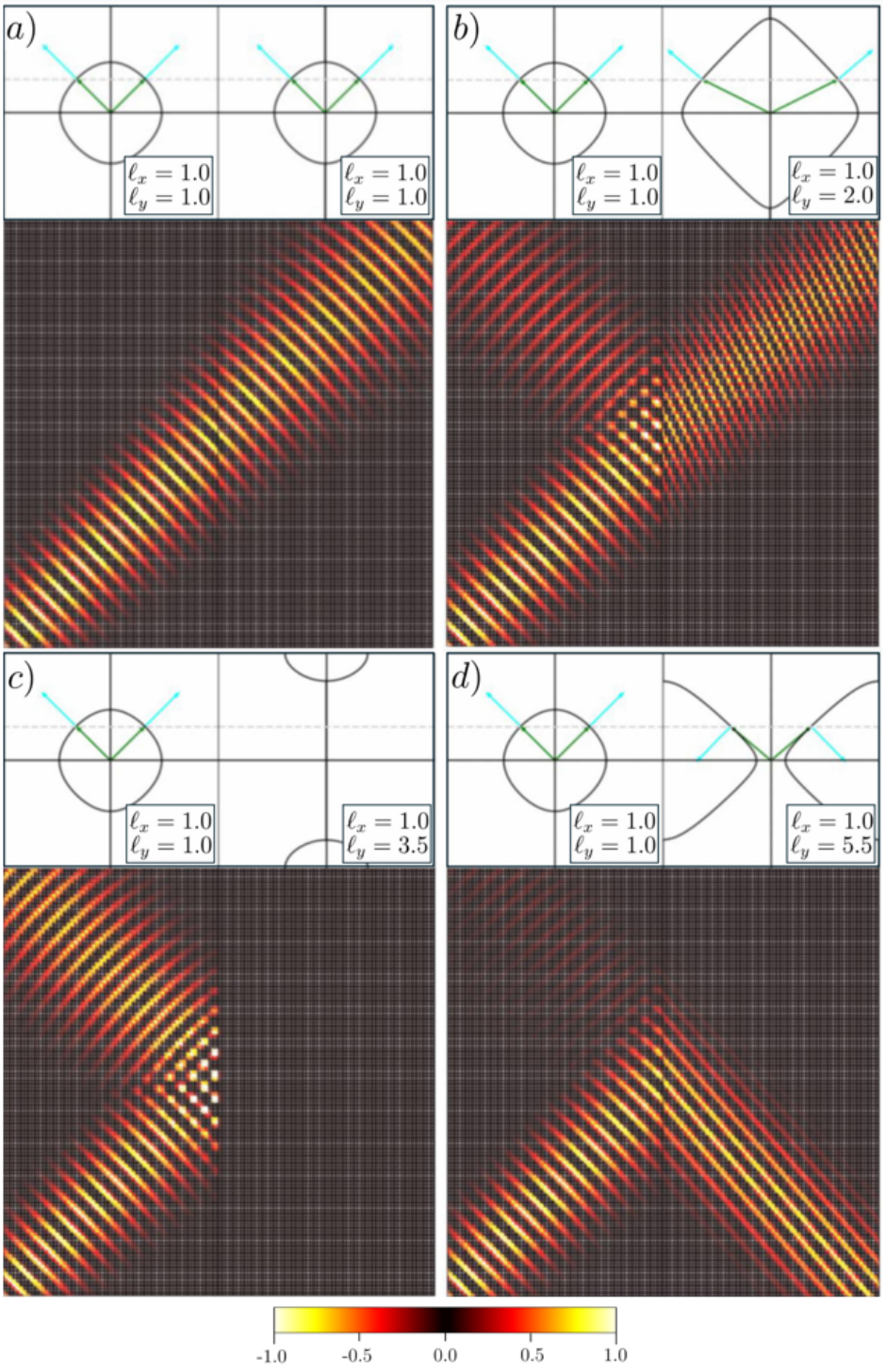

Figure 25: Shows the scattering of an incident Gaussian beam from metamaterial 1 onto metamaterial 2, where the scattering angles and amplitudes are a function of the graph metric. The metric that is varied is ℓ_y in metamaterial 2 as is stated in the inset of the iso-frequency contour. a) shows the case of a wave traveling between two identical metamaterials. b) shows positive refraction. c) shows total internal reflection. d) shows negative refraction

4.6.1 Modeling N-Layered Metamaterials

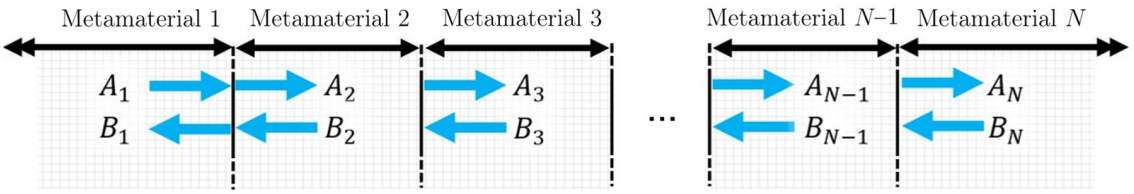

Figure 26: A system of N layered metamaterials with wave amplitudes, A_j and B_j, noted at each interface.

Consider now a system of N layered metamaterials as shown in Figure 26, each with their own properties as defined above. Each material spans a domain defined by the set of unit cells $\boldsymbol{\mathcal{N}}_j$. Here the wave function across all N materials is expressed as a linear superposition of counter propagating eigenfunction solutions of each material, that is,

$$\boldsymbol{\Psi}_{nm}(x,\kappa_y;k) = \sum_{j=1}^{N} H_j(n)\left[A_j(\kappa_y;k)\boldsymbol{\psi}^{\rightarrow}_{j,nm}(x,\kappa_y;k) + B_j(\kappa_y;k)\boldsymbol{\psi}^{\leftarrow}_{j,nm}(x,\kappa_y;k)\right]. \tag{142}$$

To evaluate the full wave function across all N materials, one must determine the coefficients A_j and B_j that satisfy the boundary conditions at all material interfaces. This is done by the Transfer Matrix Method [257]. In the previous section, the wave amplitudes between two materials were determined by constructing a scattering matrix mapping incoming to outgoing wave amplitudes between the metamaterials 1 and 2 as defined in equation (134). This matrix can be rearrange to give a transfer matrix that maps wave amplitudes from material 1 to material 2, $\tilde{\boldsymbol{S}}_{1,2}$.

$$\begin{pmatrix} A_2 \\ B_2 \end{pmatrix} = \tilde{\boldsymbol{S}}_{1,2}\begin{pmatrix} A_1 \\ B_1 \end{pmatrix} = \begin{pmatrix} t_I - \frac{r_I r_{II}}{t_{II}} & \frac{r_{II}}{t_{II}} \\ -\frac{r_I}{t_{II}} & \frac{1}{t_{II}} \end{pmatrix}\begin{pmatrix} A_1 \\ B_1 \end{pmatrix}. \tag{143}$$

This procedure can be generalised to any arbitrary materials j and $j+1$ giving

$$\begin{pmatrix} A_{j+1} \\ B_{j+1} \end{pmatrix} = \tilde{\boldsymbol{S}}_{1,2} \begin{pmatrix} A_j \\ B_j \end{pmatrix}. \tag{144}$$

Waves propagating across a given material j accumulate a Bloch phase which can be expressed in terms of the matrix

$$\boldsymbol{P}_j(\kappa_y;k) = \begin{pmatrix} e^{i\kappa^{\rightarrow}_{j,x}(\kappa_y;k)W_j} & 0 \\ 0 & e^{i\kappa^{\leftarrow}_{j,x}(\kappa_y;k)W_j} \end{pmatrix}, \tag{145}$$

where $W_j = (\max(\boldsymbol{\mathcal{N}}_j) - \min(\boldsymbol{\mathcal{N}}_j))l$ is the width of material j. Having now formulated both scattering and propagation, one can express the wave amplitudes in material N in terms of the wave amplitudes in material 1.

$$\begin{pmatrix} A_N \\ B_N \end{pmatrix} = \tilde{\boldsymbol{S}}_{N-1,N} \left(\boldsymbol{P}_{N-1}\tilde{\boldsymbol{S}}_{N-2,N-1}\right) ... \left(\boldsymbol{P}_3\tilde{\boldsymbol{S}}_{2,3}\right) \left(\boldsymbol{P}_2\tilde{\boldsymbol{S}}_{1,2}\right) \begin{pmatrix} A_1 \\ B_1 \end{pmatrix} := \tilde{\boldsymbol{S}}_{1,N} \begin{pmatrix} A_1 \\ B_1 \end{pmatrix}. \tag{146}$$

We can now rearrange this transfer operator $\tilde{\boldsymbol{S}}_{1,N}$ such that the entire system of layered materials acts as a single point scatterer by introducing the scattering matrix $\boldsymbol{S}_{1,N}$ defined as

$$\begin{pmatrix} B_1 \\ A_N \end{pmatrix} = \boldsymbol{S}_{1,N} \begin{pmatrix} A_1 \\ B_N \end{pmatrix}. \tag{147}$$

Now by setting the incident wave amplitudes A_1 and B_N, we determine the amplitudes of the scattered field by direct substitution into equation (147). Knowing the wave amplitudes in material 1, A_1 and B_1, it is trivial to determine all other amplitudes using $\boldsymbol{P}_{j-1}\tilde{\boldsymbol{S}}_{1,2}$. The results of this procedure is plotted in Figure 27 for a three layered material.

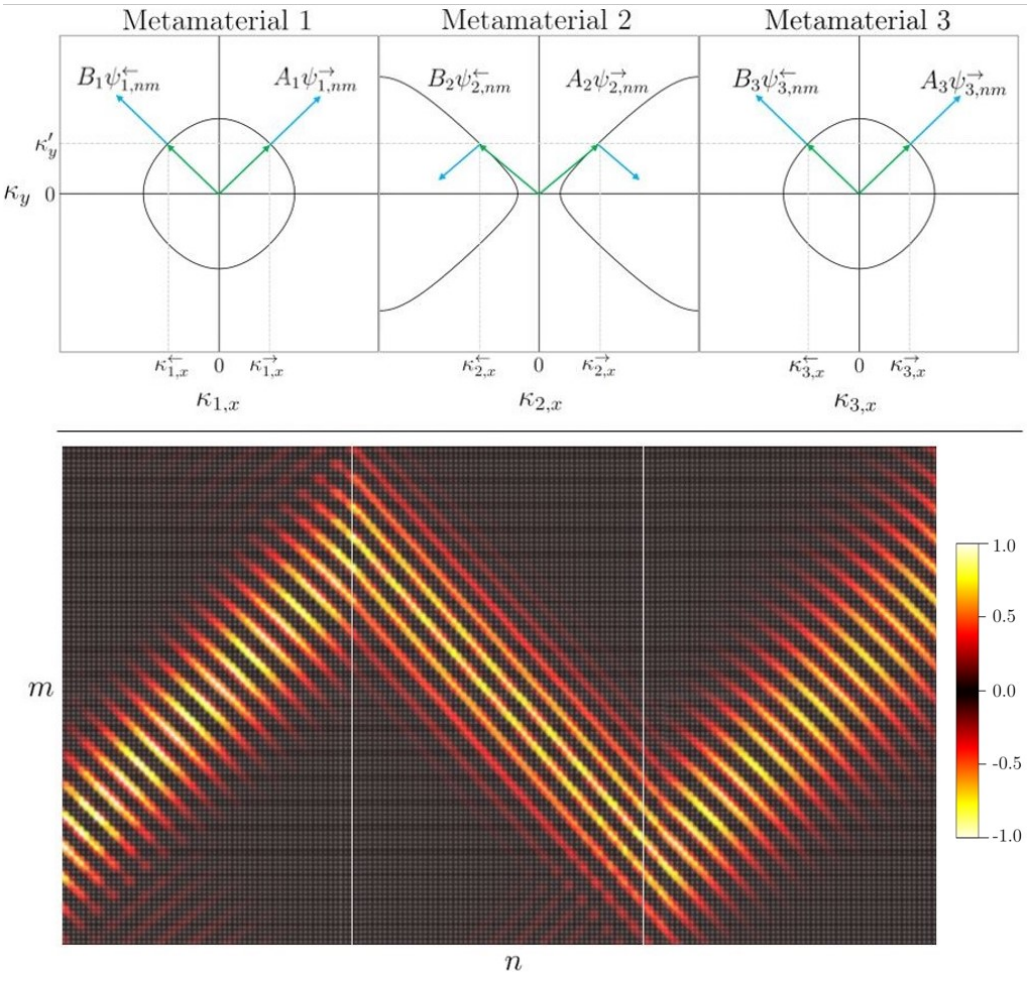

Figure 27: Top: The iso-frequency contours of three metamaterials with properties defined in Figure 25 for $k = 1/l$. Bottom: The real component of a Gaussian beam $\mathbf{\Phi}_{nm}$ incident from material 1 constructed from the full wave field Ψ_{nm} for an incident wave from metamaterial 1, $A_1 = 1$, and no incident wave from material 3, $B_3 = 0$.

Having now demonstrated that the scattering language of quantum graph theory can be used to give wave properties of anti-parallel phase and group velocity, we validate this methodology using more traditional numerical modeling techniques as well as demonstrate the effect experimentally.

4.7 Numerical and Experimental Validation

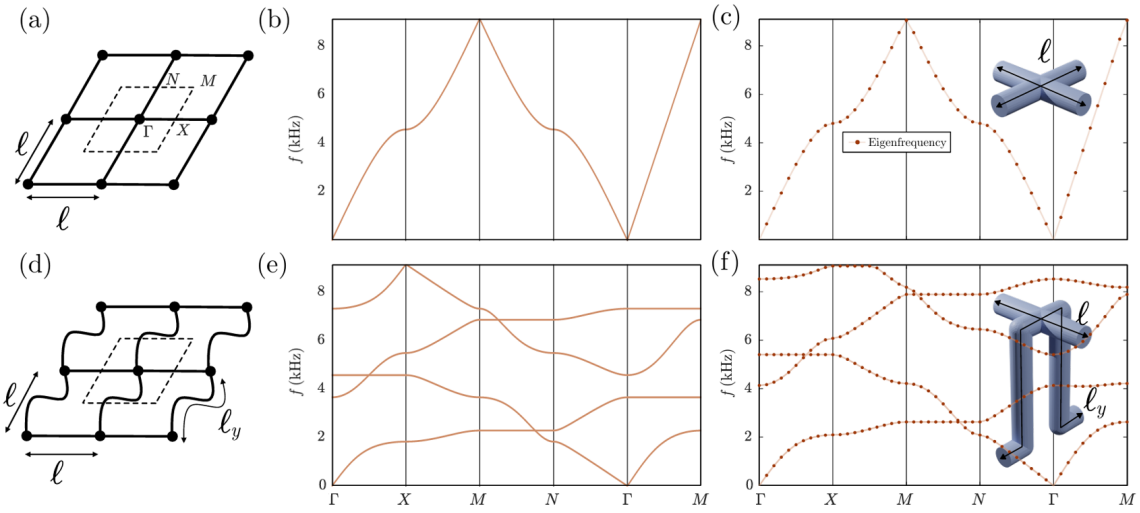

Figure 28: Comparisons of graph model and finite element dispersion curves. a) A section of the infinite isotropic graph structure ($\ell_x = \ell_y = \ell$). Vertices connect to nearest neighbours in a mesh of edges of length ℓ. The unit cell is shown as a rectangle around the central vertex. b) Corresponding dispersion curves along the Irreducible Brillouin Zone (IBZ) (directions marked in a)). c) Corresponding FEM dispersion curves for acoustic waves in a pipe network with pipes of radius 2 mm and $\ell_x = \ell_y = \ell = 20$ mm; the unit cell is shown in the inset. d) Anisotropic graph counterpart to a), such that $\ell_x = \ell$, $\ell_y = 4\ell$. e) Corresponding dispersion curves. f) Anisotropic counterpart to c), with coiled path in y such that $\ell_y = 4\ell$.

The above analytic solutions of the quantum graph model can be related to wave solutions of quasi 1D scalar fields. This is demonstrated in the by comparing with numerical solutions obtained via the finite element method (FEM) using COMSOL Multiphysics [258] for an acoustic field, see Figure 28 c) and f). Here, we set up an equivalent physical system of connected acoustic pipes in both the isotropic and anisotropic configuration. An edge in the graph model now corresponds to a pipe (of fixed radius) and a vertex corresponds to an intersection of pipes. The change in impedance at the connecting region serves as the scattering site which qualitatively

agrees with the Kirchhoff-Neumannboundary condition (57) in the graph model, providing we operate below the first cut-off frequency of the pipes. The graph structures accurately model the acoustic wave propagation in analogous pipe networks solved via FEM, as can be seen from comparing Figure 28 b) and e) with Figure 28 c) and f). Deviations start to occur with increasing frequency as expected, as we neglect spatial inhomogeneities such as bends in the graph model and other finite size effects [259]. This can be seen when comparing the upper bands in Figure 28(c) and (f). The graph model (in this form) is insensitive to the geometry of the anisotropic path, as it is parameterised only in terms of it's length, ℓ_y. Sharp bends can however be included in the graph model as in [260] and it can, of course, be recast to correspond directly to the acoustic pressure field p i.e. $\psi \mapsto p$ such that $k = \omega/c$ where ω is radian frequency and c the speed of sound. Entries in the scattering matrix are then scaled with the characteristic acoustic impedance to relate the pressure and velocity wave amplitudes in the time-harmonic regime [261]. Given the intricacies that arise in the experimental measurement we proceed with the generalised case.

To see the effect of negative refraction, we couple the two materials at a common interface along the y-direction as shown in Figure 23 with results presented in the next section. In the graph case, the coupling conditions can be given analytically by satisfying an equivalence condition between the eigenstates of the different lattices on the edges across the interface [253].

4.7.1 Characterising the metasurfaces

Experimentally characterising such a mesh would however require (potentially many) embedded microphones in the mesh; we are limited by the closure of the system i.e. there are no radiative loss channels to the surrounding free space. However, motivated by the graph model we open the system by connecting the underlying graph structure to a surface through a cavity - the pipe network now being embedded beneath the surface, shown in Figure 29 a), b) and c) for isotropic and anisotropic

configurations respectively. The open mouths of the waveguide pipes at the interface provide experimental access to probe the acoustic waveguide modes propagating within the waveguide. This structure is imbued with the dispersive characteristics of the underlying graph topology that we detect using scanning microphone techniques.

Acoustic characterisations are performed by measuring the evolution of an acoustic pulse along the surface of two samples. The samples are manufactured by CNC milling/drilling of several aluminium plates, creating the acoustic path of the fluid (air); the plates have grooves of square cross section and cylindrical holes that allow the meandering graph topology to be achieved without altering the unit cell length. To obtain the dispersive properties (dispersion curves and isofrequency contours), samples are excited by a tweeter (TFD Near-Field Loudspeaker) mounted adjacent to the side holes of the sample. The loudspeaker is driven by an arbitrary waveform generator (Keysight 33500B), producing single-cycle Sine-Gaussian pulses centred at $f_c = 5$ kHz, and a broadband amplifier (Cambridge Topaz AM5).

The acoustic pressure field is measured with a small aperture microphone (Brüel & Kjær Probe Type 4182 near-field microphone, with a preconditioning amplifier) positioned approximately 1 mm above the sample(s). Acoustic data are recorded by an oscilloscope (Picoscope 5000a) at sampling frequency $f_s = 312.5$ kHz. The microphone is mounted on a motorised xyz scanning stage (in-house with Aerotech controllers, a schematic of which is shown in Figure 30 c)), to spatially map the acoustic signal along an xy area of 34×25 unit cells, with 3 points per unit cell step-size. An average was taken over 20 measurements at each spatial position to improve the signal-to-noise ratio.

Acoustic data are analysed using Fourier techniques; the fast-Fourier Transform (FFT, operator $\mathcal{F}$) of the measured signal, voltage $V(\boldsymbol{x}, t)$ returns the real Fourier amplitude in terms of the wavenumber $\boldsymbol{k} = (k_x, k_y)$ and frequency f, $\mathcal{F}_x(|\mathcal{F}_t(V(\boldsymbol{x}, t))|)$; time-gated windowing is used to exclude reflected signals with zero-padding by a fac-

tor of 2 used in the spatial Fourier transform. The resultant experimental Fourier spectra are shown in Figure 29, along with predictions from the infinite 2D lattice from FEM simulations. The isotropic configuration (Figure 29 a)) has an acoustic surface wave spectra that closely follows (58), as seen in Figure 29 e) whilst, at the same frequency, the anisotropic configuration (Figure 29 c)) has a hyperbolic contour shown in Figure 29 f). The phase and group velocities are not co-linear, confirmed through the complex FFT which only shows wave solutions where energy propagates away from the source [262].

4.7.2 Engineering an Interface: Negative Refraction of Acoustic Surfaces Waves

Armed with the isofrequency contours (experimental, analytical, and numerical), it is possible to design refraction at an interface between two media in the conventional way through conservation of the tangential component of the wavevector to the interface (Snell's law); the direction of energy propagation is normal to the isofrequency contours in the direction of positive gradient with respect to wavevector. In this section we demonstrate negative refraction of acoustic waveguide modes using the graph model.

We create an interface between the isotropic and anisotropic configurations, labelled I and II respectively in Figure 30. The loudspeaker is mounted above a hole in sample I and the xy scanning area is 24×18 unit cells, with the source centred 5 unit cells away from the interface. Pyramidal absorbing foam is included to reduce reflections. The anisotropic sample is formed of two plates, as shown in Figure 30. We perform Fourier analysis outlined above and show comparisons between a frequency domain FEM simulation (the 'numerical experiment' with perfectly matched layer (PML) boundaries and monopole point source) and the experimental spatial response at fixed frequency. We show both the real pressure amplitude and phase of the solutions from FEM simulations and the experiment in Fig 30 a) and b) respectively.

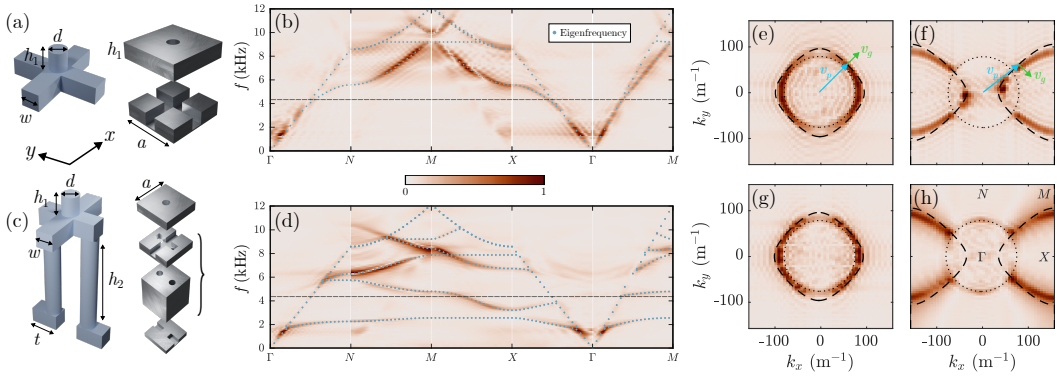

Figure 29: Unit Cell Schematics and Normalised Experimental Fourier Spectra. a) schematic of pipe network i.e. fluid path (blue regions) and milled plates. The graph network is fashioned from a square cross-section of width $w = 4\text{mm} = d$, the cavity radius connecting to the surface (height $h_1 = 5$ mm). The unit cell pitch is $a = 20$ mm. b) Experimental Fourier spectra, normalised per wavenumber along each path in the IBZ. Overlaid are FE solutions below the sound cone. Note the axis is rotated to be consistent with the experimental stage (i.e. $X \leftrightarrow N$). c) Anisotropic counterpart to a), with additional dimensions $h_2 = 12.5$ mm and $t = 7$ mm. The exploded view of the plate shows the combination of milling/drilling (plates highlighted by curly brackets are one). d) Corresponding Fourier spectra to c). e) and f) Numerical isofrequency contours obtained at 4.2 kHz (dashed line in b), c) and d)) for the configurations in a), b) and c) respectively. g) and h) Experimental counterparts - dotted circles show the sound cone and dashed lines show the analogous contours from the scaled graph model (closed system).

The negative refraction is shown through the interference of the wavefronts from the point source, highlighted by the discontinuities in phase; the refracted angles for each incident wavevector given by the direction of the group velocity, v_g, obtained from the dispersion curves [263]. The resulting wave patterns are similar to other hyperbolic metamaterials [264, 265]. In Figure 29 e) and f) we shown this by conserving the tangential component of an example incident wavevector whose phase velocity v_p is parallel to this direction, shown by the blue arrows. The green arrows

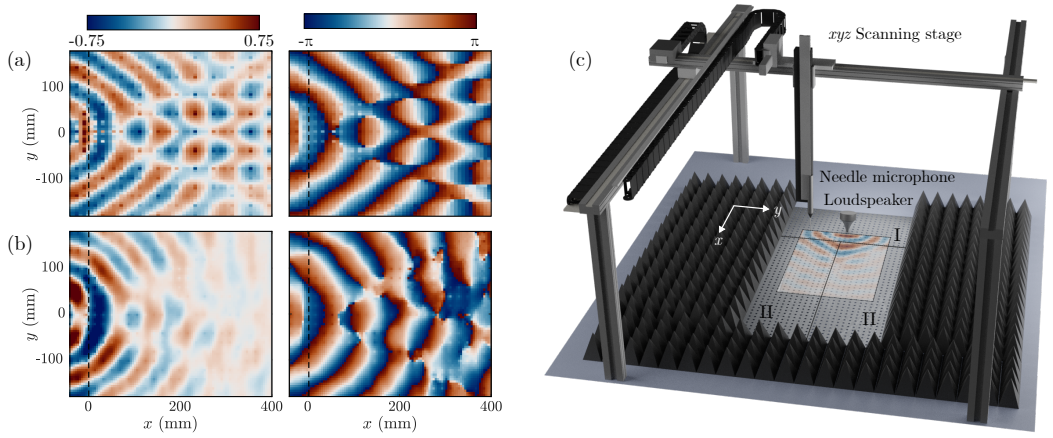

Figure 30: Comparisons of simulation and experiment. a) Frequency domain simulation with point source excitation and PML boundaries with normalised real pressure field (left) and phase (right) shown at 4.2 kHz. b) Experimental results (temporal Fourier transform) of normalised real pressure field (left) and phase (right) 4.2 kHz. c) Schematic of scanning stage and plate systems (I) and (II) that are aligned so the holes are in the same plane. Example spatial scan at 4.6 kHz is shown to highlight the scan area.

that are normal to the isofrequency contours and show the direction of the group velocity v_g. This is made obvious in Figure 31 a) where we show the absolute field calculated by point-source excitation at the vertex positions, for a similar set-up to the numerical and physical experiment. Figure 31 b) shows the equivalent absolute pressure field extracted from the FEM simulation at the intersection points between the square sections of milled plates that are not accessible with the microphone in the experiment, clearly showing negative refraction and demonstrating the utility of the graph model.

4.8 Chapter Summary

We have successfully applied quantum graph theory to the design of acoustic metamaterials as a network of interconnected space-coiled waveguides. We purposefully

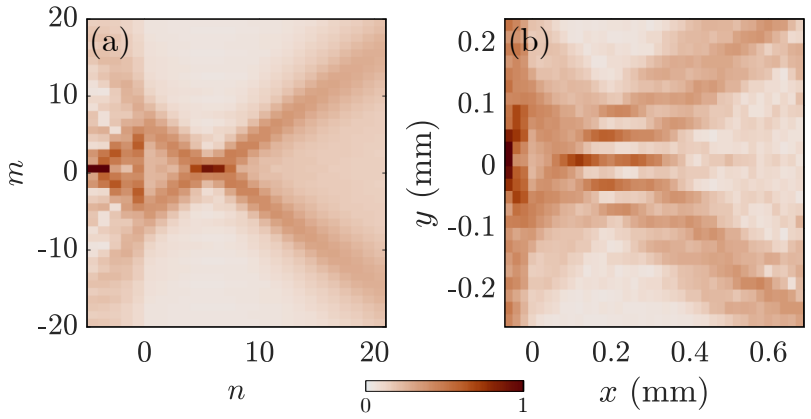

Figure 31: Comparison of graph model and FEM. a) Absolute field from graph model at vertices corresponding to plots in Figure 30. b) Normalised absolute pressure field from FEM solution extracted at equivalent vertex positions (intersections of square paths).

retain the generality of the model highlighting its usefulness all scalar wave regimes that can be reduced to systems of coupled 1D propagation problems. The analytic, or semi-analytic, nature of the graph model allows for rapid calculations and simulations, even when considering a large parameter space, providing valuable insight into the dispersive properties of mesh-like metamaterials. The graph properties were experimentally verified, by extending the model geometry to include an open system by way of connecting the structure to an acoustic metasurface of coupled resonant cavities, characterising two classes of structures (isotropic and anisotropic). We demonstrate negative refraction by engineering hyperbolic dispersion surfaces by varying bond lengths as entirely motivated by similar phenomena observed in the closed graph.

Connecting to free space introduces a radiative regime in which the waveguides leak. At the presented design frequency there is a region inside the first Brillouin Zone, the sound cone (dashed circle in Figure 29), in which the waveguide modes couple radiatively and thus we do not see the contour of the surface in this region. This is one limitation of the graph model utilised here, although lossy systems (i.e.

non-unitary scattering matrices) can be incorporated to address this. As such we anticipate exciting extensions and applications of the quantum graph model, forging a paradigm towards metamaterial design.

5 Modeling Fourier Filters via Quantum Graph Theory

Manipulating wave signals in the Fourier domain is a crucial technique in optical imaging. In this work, we introduce a novel component to this toolbox by describing a metamaterial that functions as an angular filter, capable of achieving perfect transmission at specific, customizable angles of incidence. This filter enables the selection of distinct wave-number components from an incoming wave-field within arbitrarily narrow windows. The underlying mechanism of the filter is based on inducing a resonance condition at an interface plane, which results in total reflectivity except at selected angles, where the interface becomes fully transparent.

The metamaterial is constructed using beyond-nearest-neighbor interactions between lattice sites in the interface plane. Here, we model this system using an infinite periodic quantum graph, where vertices are connected by edges of variable length.

5.1 Motivation

Recent advances in metamaterial design and manufacturing processes have greatly expanded the potential of wave-based analogue computing [266, 267]. These developments have enabled the implementation of mathematical operations such as differentiation and integration through the transmission functions of metamaterials and thin-film interfaces, reinvigorating interest in optical information processing [268]. Both Fourier domain manipulations using traditional $4f$-systems [269] and

direct manipulations in the object plane have been tested and applied. A key area of interest is edge detection, a fundamental task in autonomous image analysis that identifies and highlights object boundaries within an image. This technique has wide-ranging applications in fields such as medical imaging [270], remote sensing [271], surveillance [272], and autonomous vehicle navigation [273]. Unlike conventional software-based edge detection methods [274], wave-based analogue operations with filtering or modulation devices occur in real time, providing faster computation while reducing the noise inherent in digital image processing algorithms.

Fourier filters are essential tools in signal processing, designed to selectively transmit or block specific frequency components of an input signal. These filters operate in the frequency domain, performing operations akin to mathematical transformations that modify the spectral content of signals. In metasurfaces designed as Fourier filters, structured arrays of sub-wavelength spaced elements achieve precise control over wavefronts by tailoring their optical transfer functions (OTFs). This capability enables advanced operations such as differentiation and integration on incident light, facilitating complex signal processing tasks [120, 121, 122]. Fourier filters have broad applications in optics, acoustics, and electronics, including enhancing image contrast and resolution in imaging systems and improving signal processing in communication networks [123]. These filters are particularly valuable in optical communications, where they allow selective transmission and filtering of optical signals, reducing signal degradation and improving data integrity [124].

All wave-based techniques share a reliance on carefully designed filtering and modulation processes in the Fourier domain. In these methods, specific wavenumber components of an incoming signal are either filtered through an optically Fourier-transformed image or modified directly in the object plane by tuning the wavenumber or angle of incidence. Here, we present a novel metamaterial design capable of performing arbitrarily narrow filtering in wavenumber (or k-space), providing a key

building block for wave-number space analogue computing as well as other applications.

The key to the k-space filter's functionality is the introduction of beyond-nearest-neighbor connections between vertices in the 1D interface, which forms the filter. This concept draws inspiration from Brillouin's work on spring-mass models [275], where beyond-nearest-neighbor interactions have been applied to metamaterials for 3D bulk materials [276]. These interactions lead to Roton-like dispersion relations [276], which allow energy to flow in opposite directions at the same frequency. However, the transmission and reflection behavior of such structures in lower-dimensional settings has not been fully explored. By adapting this approach for a 1D interface, we can introduce novel filtering properties that have not been observed in previous works.

This chapter is structured as follows: In Section 5.2, we introduce the k-space filter within the scattering formalism of quantum graph theory. In Section 5.2.1, we consider the scattering environment initially as a square periodic quantum graph, with the lattice eigenfunctions acting as both the incident and scattered fields. The filter, or boundary, dividing two semi-infinite square periodic quantum graphs is formulated in Section 5.2.2, and the boundary's scattering properties and resulting graph solutions are analyzed and plotted in Section 5.3.1. At this stage, we acknowledge that a square periodic quantum graph is not an accurate representation of free space when considering higher and higher frequencies. To address this, we propose a new homogenization scheme as an open question in Section 5.4, which allows regions of the graph to be homogenized between existing lattice structures. Motivated by this potential scheme, we demonstrate in Section 5.5 that the scattering properties are maintained when considering various continuous scattering environments via FEM simulations, as well as a future application of the filter.

5.2 The k-space filter: A quantum graph formulation

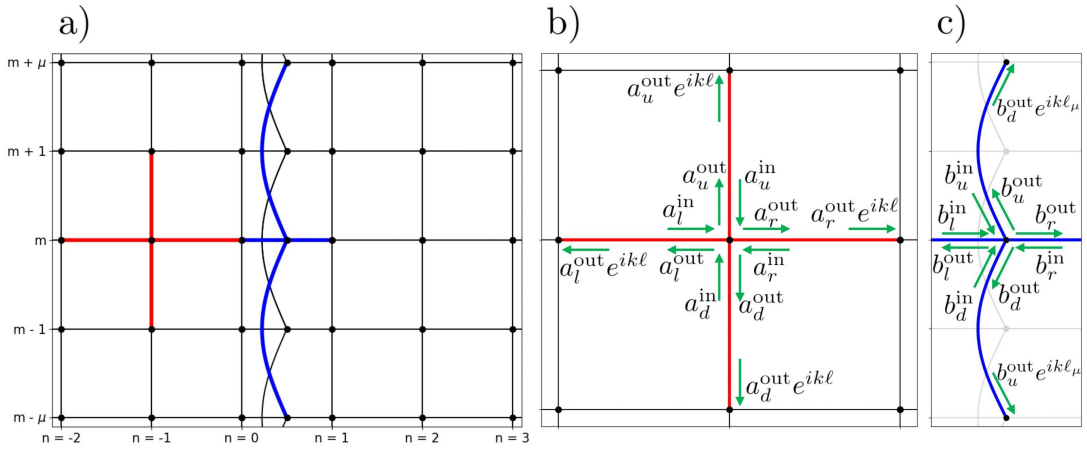

Figure 32: a) Two periodic half-spaces with an interface: the unit cell of the environment and the filter are shown in red and blue, respectively. b) The unit cell of the environment with local wave amplitudes $a_D^{\text{out/in}}$ at a specific vertex. c) The unit cell of the filter with local wave amplitudes $b_D^{\text{out/in}}$ at an interface vertex.

In this section, we describe the k-space filter using the formalism of quantum graphs. The overall setup is illustrated in Figure 32a). The system consists of two half-spaces—the environment—separated by an interface that functions as the filter. For simplicity, we focus on 2D lattices and 1D interfaces, although generalization to 3D is straightforward. The interface shown in Figure 32 breaks the horizontal periodicity, and its coupling to the environment will be treated using a scattering approach in section 5.2.2. It is important to note that the interface couples beyond-nearest-neighbor sites in the vertical direction.

5.2.1 The environment: Eigenfunction solutions of a periodic quantum graph

We briefly summarize the key equations for modeling wave transport on square periodic quantum graphs, using Kirchhoff-Neumann vertex boundary conditions to model free space. The plane waves on the mesh are described by the following

equation:

$$\begin{aligned}\boldsymbol{\psi}_{j,nm}(\hat{z},k,\kappa_y) =& A_j e^{i(\kappa_x^{\rightarrow} n+\kappa_y m)\ell}\left[e^{ik\hat{z}}\boldsymbol{\Sigma}+e^{-ik\hat{z}}\mathbb{I}\right]\mathbf{a}^{\rightarrow,\text{in}}+\\ & B_j e^{i(\kappa_x^{\leftarrow} n+\kappa_y m)\ell}\left[e^{ik\hat{z}}\boldsymbol{\Sigma}+e^{-ik\hat{z}}\mathbb{I}\right]\mathbf{a}^{\leftarrow,\text{in}}.\end{aligned} \tag{148}$$

Here, $\boldsymbol{\psi}_{j,nm} = (\psi_{j,nm,l}, \psi_{j,nm,r}, \psi_{j,nm,d}, \psi_{j,nm,u})^T$ is the vector of edge solutions to the left (l), right (r), down (d), and up (u) of vertex nm, with index $j = \{1, 2\}$ denoting the material number. A and B are complex wave amplitudes corresponding to right- or left-traveling plane waves, and $\hat{z} = \text{diag}(z_l, z_r, z_d, z_u)$ denotes a diagonal matrix of local edge coordinates, where $z_e \in [0, \ell]$. The matrix $\boldsymbol{\Sigma}$ defines the vertex scattering matrix, which is set to be Kirchhoff-Neumann as in equation (120). The vector $\mathbf{a}^{\rightleftharpoons,\text{in}} = (a_l^{\rightleftharpoons,\text{in}}, a_r^{\rightleftharpoons,\text{in}}, a_d^{\rightleftharpoons,\text{in}}, a_u^{\rightleftharpoons,\text{in}})^T$ represents the incoming wave amplitudes at a vertex within the lattice, given as the eigenvector of the graph quantum map, given in equation (55). The space of allowed solutions on the lattice lies on the band defined by the secular equation associated with the quantum map, given by equation (58), which, for Kirchhoff-Neumann boundary conditions, yields the horizontal wavenumber κ_x as:

$$\kappa_x^{\rightleftharpoons}(k,\kappa_y) = \pm\frac{1}{\ell}\text{arccos}(2\text{cos}(k\ell) - \text{cos}(\kappa_y\ell)). \tag{149}$$

The $+/-$ solutions represent right- and left-traveling waves, respectively, as discussed in section 4.3. We will now explore how these plane waves scatter from a boundary connecting two semi-infinite half-spaces.

5.2.2 The beyond-nearest-neighbor interface

Consider the scattering of an open, infinitely periodic quantum graph as a model for the interface, as illustrated in Figure 32c). This graph consists of vertices with the same period ℓ as the environment, and Kirchhoff-Neumann boundary conditions are

applied (120). The key difference from the bulk is that vertex m is not connected to its nearest neighbors $m \pm 1$, but rather to vertices $m \pm \mu$ by edges of varying length ℓ_μ. The wave solution on a given edge e is:

$$\psi_{m,e} = e^{i\kappa_y m\ell} \left(b_e^{\text{out}} e^{ikz_e} + b_e^{\text{in}} e^{-ikz_e} \right), \tag{150}$$

where $b_e^{\text{out/in}}$ are complex wave amplitudes, and the domain of the coordinates on each edge is $z_d \equiv z_u \in [0, \ell_\mu]$ and $z_l \equiv z_r \in [0, \infty)$.

The goal is to first determine the interface scattering matrix and then couple this matrix to the environment to determine the relationship between the incident (A_1, B_2) and scattered (B_1, A_2) fields at the interface. We begin by expressing the vertex scattering using equation (120) in block form:

$$\begin{pmatrix} b_l^{\text{out}} \\ b_r^{\text{out}} \end{pmatrix} = \begin{pmatrix} -1/2 & 1/2 \\ 1/2 & -1/2 \end{pmatrix} \begin{pmatrix} b_l^{\text{in}} \\ b_r^{\text{in}} \end{pmatrix} + \begin{pmatrix} 1/2 & 1/2 \\ 1/2 & 1/2 \end{pmatrix} \begin{pmatrix} b_d^{\text{in}} \\ b_u^{\text{in}} \end{pmatrix}, \tag{151}$$

and

$$\begin{pmatrix} b_d^{\text{out}} \\ b_u^{\text{out}} \end{pmatrix} = \begin{pmatrix} 1/2 & 1/2 \\ 1/2 & 1/2 \end{pmatrix} \begin{pmatrix} b_l^{\text{in}} \\ b_r^{\text{in}} \end{pmatrix} + \begin{pmatrix} -1/2 & 1/2 \\ 1/2 & -1/2 \end{pmatrix} \begin{pmatrix} b_d^{\text{in}} \\ b_u^{\text{in}} \end{pmatrix}. \tag{152}$$

The edge and Bloch phase dynamics in the vertical direction are given by:

$$\begin{pmatrix} b_d^{\text{in}} \\ b_u^{\text{in}} \end{pmatrix} = \begin{pmatrix} 0 & e^{i(k\ell_\mu - \kappa_y \mu\ell)} \\ e^{i(k\ell_\mu + \kappa_y \mu\ell)} & 0 \end{pmatrix} \begin{pmatrix} b_d^{\text{out}} \\ b_u^{\text{out}} \end{pmatrix}. \tag{153}$$

Substituting equation (153) into equation (152) generates the coupling matrix $\boldsymbol{\rho}_\mu$, which performs the mapping:

$$\begin{pmatrix} b_d^{\text{in}} \\ b_u^{\text{in}} \end{pmatrix} = \boldsymbol{\rho}_\mu \begin{pmatrix} b_l^{\text{in}} \\ b_r^{\text{in}} \end{pmatrix}, \tag{154}$$

where

$$\boldsymbol{\rho}_\mu = \frac{1}{2\left(e^{-ik\ell_\mu} - \cos(\kappa_y \mu \ell)\right)} \begin{pmatrix} e^{-i\kappa_y\mu\ell} - e^{ik\ell_\mu} & e^{-i\kappa_y\mu\ell} - e^{ik\ell_\mu} \\ e^{i\kappa_y\mu\ell} - e^{ik\ell_\mu} & e^{i\kappa_y\mu\ell} - e^{ik\ell_\mu} \end{pmatrix}, \tag{155}$$

Substituting equation (154) into (151) yields the interface scattering matrix $\boldsymbol{S}_\mu$:

$$\begin{pmatrix} b_l^{\text{out}} \\ b_r^{\text{out}} \end{pmatrix} = \boldsymbol{S}_\mu \begin{pmatrix} b_l^{\text{in}} \\ b_r^{\text{in}} \end{pmatrix} = \begin{pmatrix} r_\mu & t_\mu \\ t_\mu & r_\mu \end{pmatrix} \begin{pmatrix} b_l^{\text{in}} \\ b_r^{\text{in}} \end{pmatrix}, \tag{156}$$

where the filter transmission coefficient is given by:

$$t_\mu = \frac{i\sin(k\ell_\mu)}{\cos(\kappa_y\mu\ell) - e^{-ik\ell_\mu}}, \tag{157}$$

and the filter's reflection coefficient is conveniently given in terms of the transmission coefficient,

$$r_\mu = t_\mu - 1. \tag{158}$$

With the interface scattering matrix determined, we can now embed the interface into the environment and analyze the scattered field.

5.3 The Full System

With the interface scattering matrix $\boldsymbol{S}_\mu$ derived, we can now couple the wave dynamics between the environment and the interface to solve for the scattered field. The leads extending from the interface are truncated to a finite length and attached at the midpoint, $z_r = z_l = \ell/2$, of the horizontal edges of the environment, as shown

in Figure 32a). On the connecting edges, the eigenfunctions of the mesh act as the inputs and outputs for the interface scattering matrix. Specifically, we have:

$$b_l^{\text{out}} = e^{-ik\ell/2}\left[A_1 a_r^{\rightarrow,\text{in}} + B_1 a_r^{\leftarrow,\text{in}}\right], \tag{159a}$$

$$b_l^{\text{in}} = e^{-ik\ell/2}\left[A_1 a_r^{\rightarrow,\text{out}} + B_1 a_r^{\leftarrow,\text{out}}\right], \tag{159b}$$

$$b_r^{\text{out}} = e^{+ik\ell/2}\left[A_2 e^{i\kappa_x^{\rightarrow}\ell} a_l^{\rightarrow,\text{in}} + B_2 e^{i\kappa_x^{\leftarrow}\ell} a_l^{\leftarrow,\text{in}}\right], \tag{159c}$$

$$b_r^{\text{in}} = e^{+ik\ell/2}\left[A_2 e^{i\kappa_x^{\rightarrow}\ell} a_l^{\rightarrow,\text{out}} + B_2 e^{i\kappa_x^{\leftarrow}\ell} a_l^{\leftarrow,\text{out}}\right]. \tag{159d}$$

By substituting the above expressions into equation (156), we can obtain the full interface scattering matrix embedded within the environment. This matrix is referred to as the filter scattering matrix, $\boldsymbol{S}_F$, which performs the mapping:

$$\begin{pmatrix} B_1 \\ A_2 \end{pmatrix} = \boldsymbol{S}_F \begin{pmatrix} A_1 \\ B_2 \end{pmatrix}, \tag{160}$$

where

$$\begin{aligned} \boldsymbol{S}_F = &\left[\boldsymbol{S}_\mu \boldsymbol{M}^{\rightarrow,\text{out}} - e^{-ik\ell}\boldsymbol{M}^{\rightarrow,\text{in}}\right]^{-1} \\ &\left[e^{-ik\ell}\boldsymbol{M}^{\leftarrow,\text{in}} - \boldsymbol{S}_\mu \boldsymbol{M}^{\leftarrow,\text{out}}\right], \end{aligned} \tag{161}$$

and

$$\boldsymbol{M}^{\rightleftharpoons,\text{out/in}} = \begin{pmatrix} a_l^{\rightleftharpoons,\text{out/in}} & 0 \\ 0 & e^{i\kappa_x^{\rightleftharpoons}\ell} a_r^{\rightleftharpoons,\text{out/in}} \end{pmatrix}. \tag{162}$$

The scattering matrix $\boldsymbol{S}_F$ thus determines how incoming plane wave eigenfunctions of the bulk, with fixed parameters (k, κ_y), are coupled into outgoing eigenfunctions for the same set of parameters.

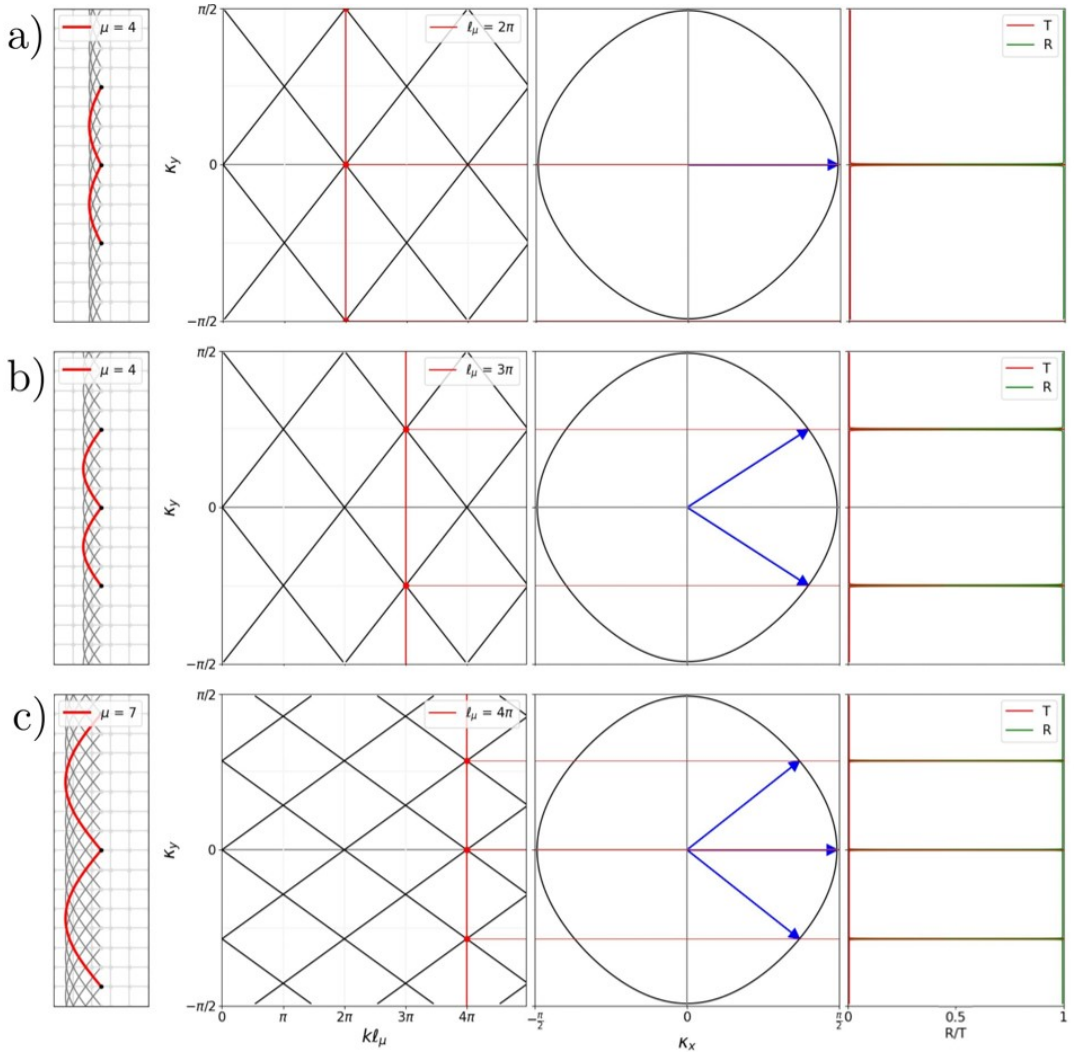

Figure 33: Left: The real-space lattice with a boundary formed by beyond-nearest-neighbor connections, where vertex m is connected to vertex $m \pm \mu$. Left-Middle: The condition space for unit transmission given by equation (166), where the choice of edge length ℓ_μ is plotted in red. The points of intersection define the values of κ_y (angles) that allow unit transmission. Middle-Right: The iso-frequency contour of the lattice with resonant angles projected (blue arrows). Right: The transmission and reflection amplitudes as functions of κ_y, shown in red and green, respectively. a) shows the condition for $\mu = 4$ and $\ell_\mu = 2\pi\ell$. b) shows the condition for $\mu = 4$ and $\ell_\mu = 3\pi\ell$. c) shows the condition for $\mu = 7$ and $\ell_\mu = 4\pi\ell$.

5.3.1 The interface acting as a filter in κ_y space - results

The scattering properties of the beyond-nearest-neighbor metamaterial forming the interface exhibit unique characteristics that allow it to act as a perfect filter in κ_y space under certain conditions. Specifically, the transmission coefficient t_μ at the interface behaves like a Kronecker-delta function at specific κ_y values, whenever the interface edge connections of length ℓ_μ are a half-integer multiple of the wavelength. In this case, the transmission coefficient is given by:

$$t_\mu = \begin{cases} 1, & \text{if } k\ell_\mu = p\pi \text{ and } \kappa_y = \kappa_y^{(q)} = q\pi/\mu\ell \\ 0, & \text{if } k\ell_\mu = p\pi \text{ and } \kappa_y \neq \kappa_y^{(q)}, \end{cases} \tag{163}$$

where $p, q \in \mathbb{Z}$, and $\kappa_y^{(q)}$ represents a discrete set of tangential wave vectors. To understand this, consider the transmission coefficient in equation (157). When $k\ell_\mu = p\pi$, the numerator in equation (157) vanishes, leading to total reflection. This represents a resonance in the beyond-nearest-neighbor connection. The solution at the connecting vertices can be found by solving equation (150) with Eqs. (153) and (154), leading to:

$$\psi_{m,d}(0) = \psi_{m,u}(0) = 0. \tag{164}$$

These represent Dirichlet boundary conditions for the standing wave solutions on the edges of length ℓ_μ, causing the resonances in these edges to decouple from the overall wave dynamics. This pipe harmonic is plotted in Figure 34 a). The vertices forming the filter thus act as a barrier for wave transmission, preventing energy from flowing between the two half-spaces.

However, if $\kappa_y = q\pi/\mu\ell$, the numerator and denominator cancel, resulting in discrete cases of unitary transmission, i.e.,

$$\frac{i\sin(k\ell_\mu)}{\cos(\kappa_y\mu\ell) - e^{-ik\ell_\mu}} = 1, \tag{165}$$

or equivalently,

$$\cos(k\ell_\mu) = \cos(\kappa_y\mu\ell). \tag{166}$$

In this case, the connecting vertices have wave amplitudes given by:

$$\psi_{m,d}(0) = \psi_{m,u}(0) = e^{i\kappa_y m\ell}\left(b_l^{\text{in}} + b_r^{\text{in}}\right), \tag{167}$$

which results in a shift from Dirichlet to periodic boundary conditions for the resonance states, allowing energy transmission. The fields within the filter are plotted in Figure 34 b).

Notably, the number of angular values that can be filtered, as well as which values are filtered, can be controlled by adjusting the beyond-nearest-neighbor parameter μ and the length ℓ_μ, thus altering k. The conditions for unit transmission are illustrated graphically in Figure 33 for various values of μ and ℓ_μ.

According to standard Fourier analysis, the width of solutions allowed through the filter is inversely proportional to the width of the transmission coefficient. In other words, the filter only allows plane waves at resonance (where the amplitude vanishes). However, if we consider wave solutions near resonance, i.e., $k\ell_\mu = p\pi \pm \epsilon$ with ϵ small, the transmission peak broadens, allowing for the transmission of beams with finite widths. Results for different values of μ, ℓ_μ, and ϵ are shown in Figure 35. In each case, a relatively broad beam enters from the left, with most waves being reflected at the interface.

In Figure 35a), we explore the case of next-to-nearest-neighbor connections ($\mu = 2$),

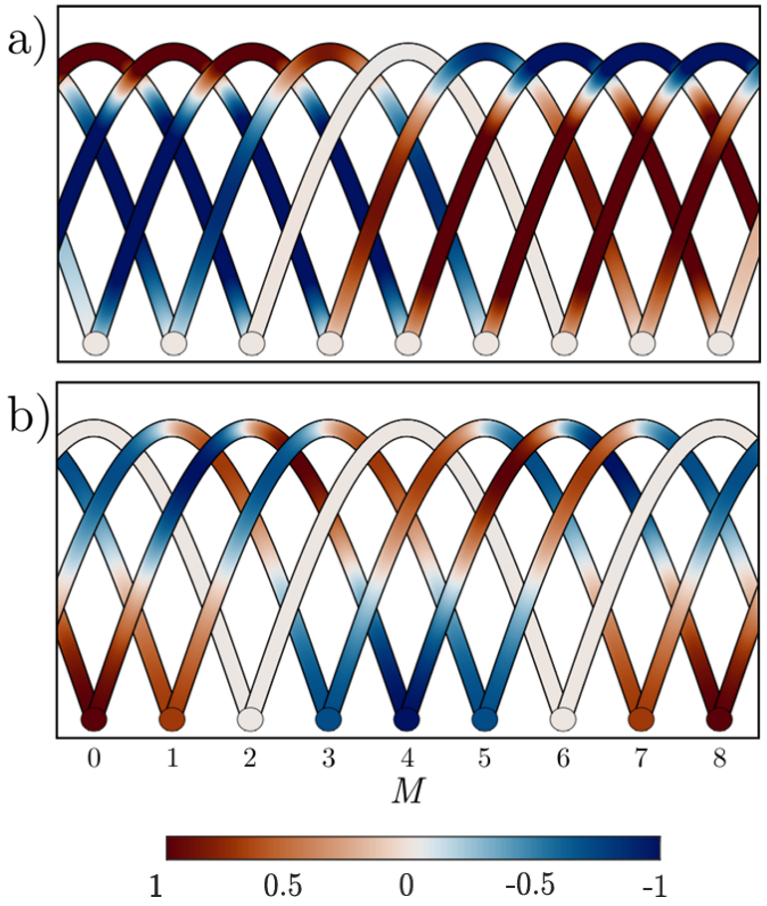

Figure 34: Field plots (a) and (b) show the real component of the wave field $\Re\{\psi_{m,e}(z_{m,e})\}$ within the filter bonds for $\mu = 4$ and $\ell_\mu = 3\pi$ at a frequency $k = 1/\ell$. (a)/(b) show the field off/on resonance respectively

which results in solutions for $\kappa_y = 0$ (i.e., $q = 0$) only. Note that the κ_y values are constrained to the real contour defined by equation (149). Solutions outside this contour represent evanescent modes that do not carry energy away from the boundary. By increasing μ from $\mu = 4$ in Figure 35b) to $\mu = 7$ in Figure 35c), more angles can be transmitted.

5.4 A Continuous Model and An Open Question

The Fourier filter described so far has been formulated within the discrete scattering framework of quantum graph theory. In this setup, the scattering environment is

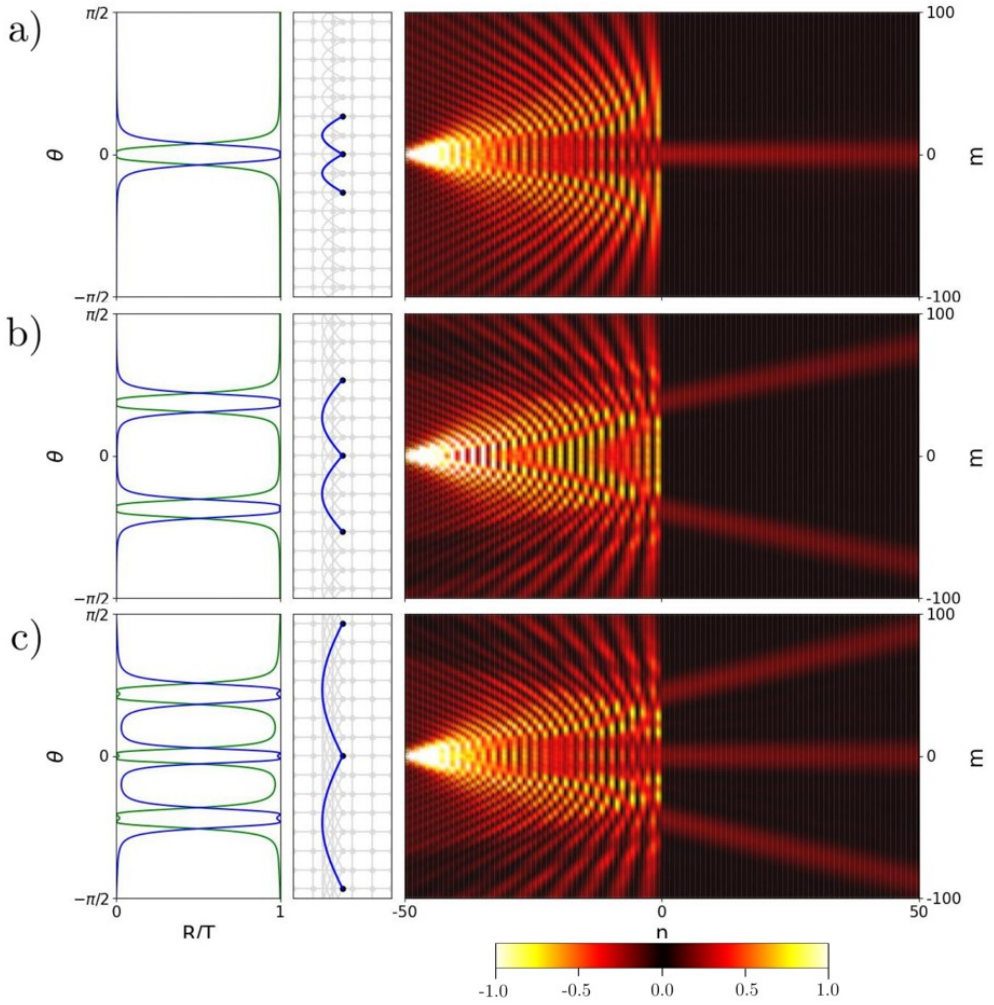

Figure 35: Left: Reflection $R = |B_1|^2$ and transmission $T = |A_2|^2$ coefficients, shown in green and blue respectively, as functions of the incident phase angles $\theta = \arctan(\kappa_y/\kappa_x)$. Middle: Filter configuration used. Right: Resulting wave field for parameters a) $\mu = 2$, $\ell_\mu = 2\pi - \epsilon$, $\epsilon = 0.05$; b) $\mu = 4$, $\ell_\mu = 3\pi - \epsilon$, $\epsilon = 0.1$; c) $\mu = 7$, $\ell_\mu = 4\pi - \epsilon$, $\epsilon = 0.3$.

modeled using a square periodic quantum graph, which approximates a 2D real space in the long-wavelength regime, as shown in Figure 36a). The filter itself is modeled through beyond-nearest-neighbour connections between vertices, allowing for a resonant effect that selectively permits wave transmission at specific angles while blocking all others. Although the quantum graph formalism is an elegant and effective mathematical tool, it remains an approximation of the continuous

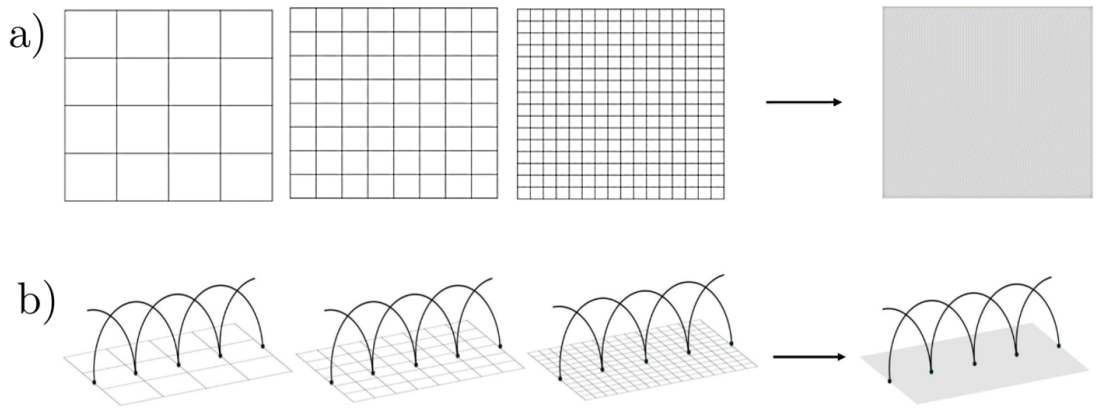

Figure 36: a) The well-known homogenisation procedure for a single lattice of constant period ℓ, which allows for the correct reproduction of the Hamiltonian on Euclidean space in the limit $\ell \to 0$ [224]. b) The yet unknown homogenisation procedure for determining the continuum limit solutions of a graph that maintains a given period throughout homogenisation.

systems encountered in the real world. The real world is not strictly discrete, and understanding how quantum graph models relate to continuous wave phenomena is essential for practical applications.

To bridge this gap, it is necessary to develop a homogenisation scheme that transitions from the quantum graph framework to real-space solutions, allowing the scattering properties to be studied in a continuous domain. Currently, the process of homogenising a quantum graph while retaining the beyond-nearest-neighbour connections—critical for the filter's resonance effect—remains an open question, as illustrated in Figure 36b). The mathematical tools required for such a homogenisation process have not yet been developed, but they would provide valuable insights into the behavior of the filter in continuous media.

In the absence of a formal homogenisation process, computer simulations offer a powerful alternative for exploring how the quantum graph-inspired Fourier filter behaves in real-world continuous systems.

5.5 Implementation - FEM Simulations

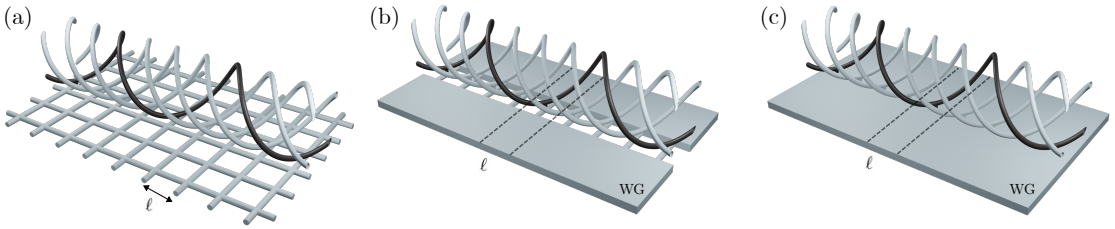

Figure 37: Discrete and continuous spaces, coupled by the filter. (a) A square periodic lattice with period ℓ with the filter attached at the midpoint of the lattice as helices that facilitate BNN connections - one helix is highlighted in black resembling the bond in Fig. 23(a). (b) Two rectangular acoustic waveguides coupled by a grating of thin tubes with period ℓ, coupled at the midpoint to the filter. (c) A rectangular acoustic waveguide with periodic holes spaced by length ℓ, the openings of which are coupled to the filter.

Having formulated the scattering properties of the quantum graph k-space filter, we turn to an equivalent network of acoustic pipes [254]; we consider the wave field to correspond directly to an acoustic pressure field $\psi \mapsto p$ such that $k = \omega/c$ with c the speed of sound. The parameters of the acoustic pipe directly incorporate the non-dimensional form of the graph model such that $\ell = 1$ m, and we choose the pipe radius to be $r = 0.078$ m; we choose these purely for convenience and note that the resonant frequencies scale linearly with the length scale. An edge in the graph model thereby corresponds to a pipe of fixed radius, and a vertex corresponds to an intersection of pipes as in [254].

We first focus on a description of the environment in which the filter is coupled to a discrete square mesh, in-line with a graph formalism as employed above and in [253, 277, 254]. The network of pipes considered is illustrated in Fig. 37(a); the filter is comprised of $\mu = 4$ helices of length $\ell_\mu = 3\pi$ m. They are connected by small tubes (of height $h = 0.1$ m, $r = 0.078$ m) to the underlying pipe network at a distance $\ell/2$ between vertices. We utilise the Finite Element Method (FEM) using

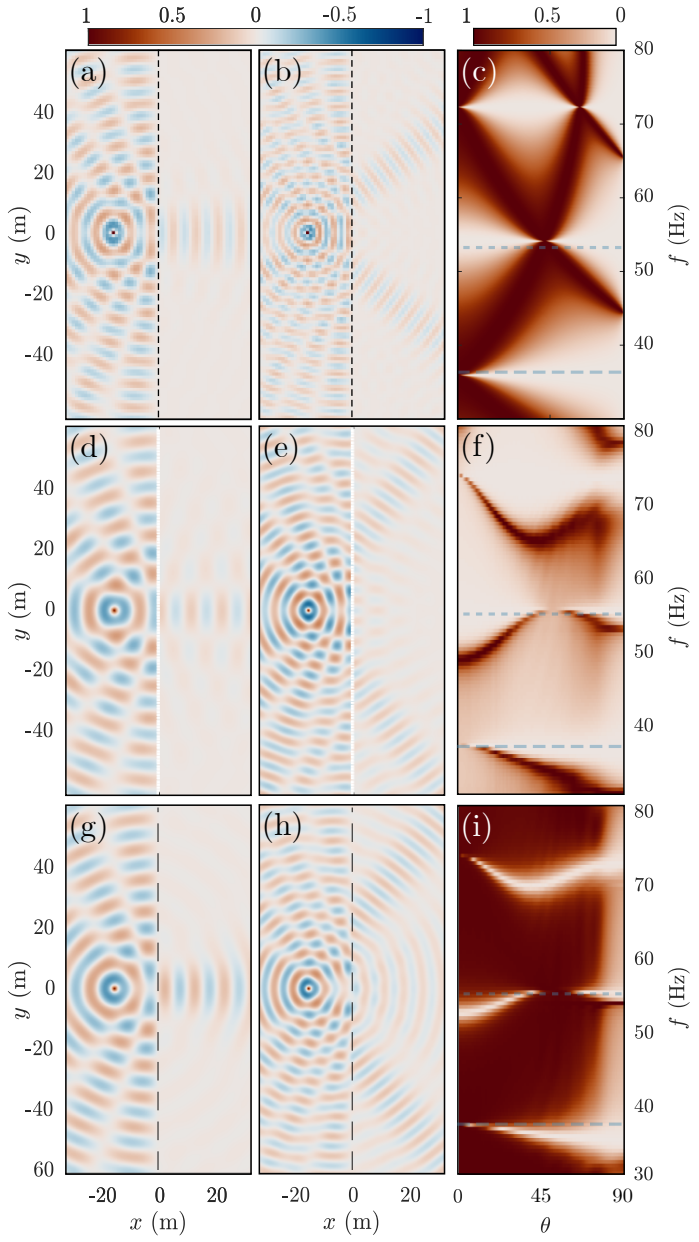

Figure 38: Graph and FEM simulations. (a,b) FEM simulations of a discrete lattice with point source excitation at the frequencies marked by horizontal dashed lines in (c). The interface is marked by the vertical dashed black line. (c) Transmission coefficient as a function of frequency and angle as predicted from the graph model. (d,e) as (a,b), but for the continuous waveguides joined by the filter (Fig. 37(b)). (f) as (c) but from FEM predictions. (g,h,i) as (d,e,f) but for the continuous waveguide (Fig. 37(c)).

COMSOL Multiphysics [258] to perform scattering simulations in a finite domain (with absorbing outer boundaries). A $60\ell \times 120\ell$ domain is generated and a frequency domain simulation is performed under point source excitation at $(-15\ell, 0)$, over a range of frequencies. The resulting discrete angle transmission is shown in Fig. 38 (a,b) at two different frequencies where we note the effect of discrete angle transmission for both one and two angles. We compare this with the predicted transmission coefficient as a function of angle and frequency from a pure graph model as shown in Fig. 38(c) and find excellent agreement.

A reasonable criticism of the lattice representation may be that the square periodic graph does not truly represent free space and that this model will break down for frequencies at which the properties of the lattice dominate the scattered field. We propose simply replacing the discrete lattice on either side of the filter with a continuous acoustic waveguide. The motivation being that, the filter shall couple the solutions on either side of the interface, irrespective of the underlying dispersive properties of the media. The design illustrated in Fig. 37(b), which is comprised of two semi-infinite acoustic rectangular waveguides (of thickness r). The waveguides are coupled via a periodic array of tubes (of radius r, separation ℓ), with the helical BNN filter placed atop at $\ell/2$, reminiscent of a diffraction grating. Here, we consider frequencies well below the grating diffraction limit, such that the transmitted field across the grating supports only one mode i.e. the grating is non-diffractive at the frequencies considered. We show in Fig. 38(d,e) FEM simulations for this configuration. The scattering properties of the filter still dominate the transmission profile, leading to both single and double angle transmission at resonant frequencies. Note the slight change in direction for the double angle transmission, which is due to the difference in dispersive properties of the slab waveguide when compared to the dissipative properties of the square periodic lattice. Figure 38(f) shows the transmission coefficient $|T(f, \theta)|^2$ as a function of frequency and angle, obtained numerically from FEM simulations with incident plane waves at single frequencies.

Finally we push the model yet further and propose a fully continuous, infinite acoustic rectangular waveguide that supports an acoustic pressure field. In the waveguide there is a periodic array of holes in the top layer, connected to the filter, shown in Fig. 37(c). This allows for unperturbed wave transmission throughout the waveguide. Despite the graph model not incorporating a continuous medium between the vertices of the filter, a similar transmission profile is indeed present within this device; transmission across the array is still governed by the resonant characteristics of the filter. The main difference is that the effective Dirichlet conditions at the junctions (as shown in Fig. 23) leading to full reflection are not enforceable at all frequencies. On resonance, however, we see full transmission at similar angles and frequencies to the discrete cases. Figure 38(g,h) shows point source simulations at frequencies similar to Fig. 38(d,e) and Fig. 38(i) shows $|T(f,\theta)|^2$ evaluated in a similar manner to Fig. 38(f).

To this end, we propose a continuous model of the filter, which we simulate using COMSOL Multiphysics. The 2D real space is modeled as a 3D waveguide formed by two slabs with Neumann boundary conditions, allowing acoustic waves to propagate freely between them. To mimic the quantum graph topology, a periodic arrangement of holes is introduced in the top slab, spaced by a distance ℓ. These holes are connected by thin tubes, which approximate 1D wave transport below the cut-off frequency, thus emulating the beyond-nearest-neighbour connections found in the discrete graph. This setup mirrors the discrete scattering system with a continuous-space analog.

The CAD design of this device, was implemented and simulated in COMSOL, yielding remarkable results. In the long-wavelength regime, the simulations revealed the same angular selectivity for wave transmission, confirming the resonance effect of the Fourier filter. This demonstrates that the Fourier filter effect, initially predicted using quantum graph theory, persists in real-world continuous environments. More

importantly, it validates the quantum graph model as a powerful tool for predicting wave behavior in metamaterials. Moreover, these simulations open new possibilities for designing wave devices in continuous systems, where principles derived from quantum graph theory can guide the development of novel materials and filtering mechanisms.

5.5.1 A Proposed Application

Fourier filters are widely used in image processing tasks such as edge detection, where the primary goal is to highlight sharp transitions corresponding to object boundaries. A novel application of a specialized Fourier filter, which selectively allows wave transmission at specific angles while blocking others, can be utilized to infer the geometry of hidden objects. By illuminating an object with a wave source and filtering the scattered waves based on their angles, the object's contours can be reconstructed, as illustrated in Figure 39. This method is particularly valuable in scenarios requiring high angular precision, offering an alternative to traditional isotropic Fourier filters, which affect all directions uniformly [274].

In medical diagnostics, this approach can complement existing Fourier-based techniques employed in MRI and CT scans, where edge detection is critical for identifying structures such as tissues, blood vessels, or tumors. Traditional filters often face challenges in detecting edges at specific orientations, but an angularly selective filter could enhance precision by isolating scattered waves at particular angles, thus improving the clarity of geometrically complex features [278]. This method holds promise not only for non-invasive medical imaging but also for industrial applications, offering improved capabilities for both fields.

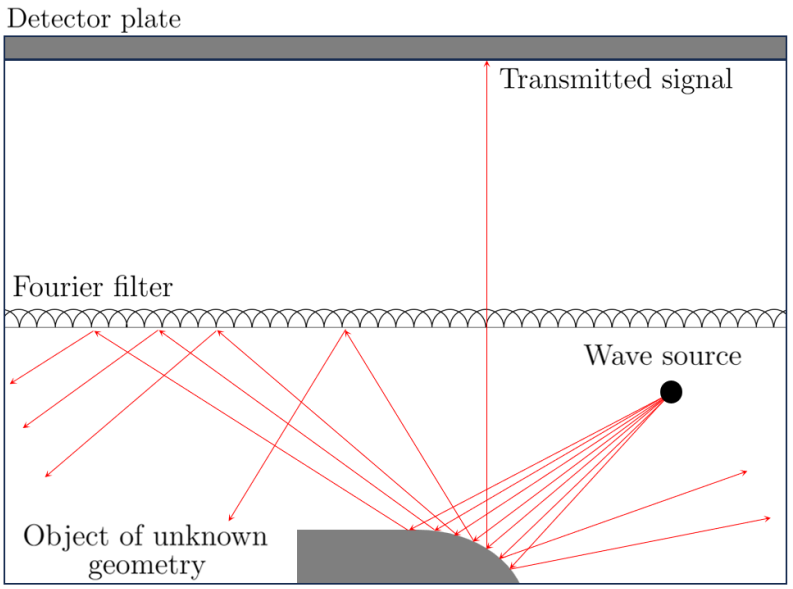

Figure 39: An object of unknown geometry illuminated by a wave source, with the resulting wave scattering shown as a ray diagram. The Fourier filter, placed above the object and wave source, allows only waves at particular angles to pass through to the detector plate. By rotating either the object or the filter, the geometry of the hidden object can be inferred.

5.6 Chapter Summary

We introduce a novel angular filter and demonstrate its functionality via a quantum graph approach designed for wave transmission at customizable angles. The filter maintains unit reflectivity due to a resonance condition that switches off at a set of discrete angles (or κ_y values). The chapter treats the wave problem as an infinite square periodic quantum graph, whose eigenfunction solutions represent both the incident and scattered fields in free space. The filter is constructed from an infinite 1D periodic interface with non-local vertex connections. The coupling of the environment and the interface is explored via a scattering approach, allowing one to determine the reflection and transmission coefficients of the filter for different parameter configurations. The filtering effect can be traced back to a change in the effective boundary condition for the resonant state switching from Dirichlet to

periodic at specific wave angles. While formal homogenisation of a periodic quantum graph, with additional non-local vertex connections remains an open question, COMSOL simulations of a continuous waveguide system confirm that the filter's resonance effect persists even in the continuum. This confirmation makes the proposed device practical for real world implementation. We envisage that the proposed filter will find applications in optical computing and edge detection with benefits for medical imaging, remote sensing, surveillance, and autonomous vehicle navigation, among others.

6 Conclusion

This thesis has extended the discrete scattering formalism of quantum graph theory to explore wave propagation in complex finite and infinite periodic systems. By demonstrating that periodic quantum graphs can be structured to produce non-trivial wave phenomena analogous to those observed in metamaterials, this work highlights the potential of quantum graphs as a powerful tool for metamaterial design. The effectiveness of this scattering approach was validated through numerical simulations and experimental results in the acoustic regime, establishing a new paradigm for the modeling and study of metamaterials across scalar wave systems.

In Chapter 2, we established the foundation of the scattering formalism in quantum graph theory. By treating vertices as point scatterers with tunable boundary conditions, we demonstrated how wave behavior could be controlled by manipulating vertex properties. Special cases such as Kirchhoff-Neumann, Dirichlet, and δ-type boundary conditions were analysed to show their impact on wave propagation and the eigenstructure of the graph. Additionally, we extended the formalism to infinite periodic quantum graphs, showing how frequency-dependent boundary conditions lead to resonant effects and the creation of band gaps. These concepts laid the groundwork for the remainder of the thesis by illustrating how lattice geometry and

boundary conditions can influence wave transmission, providing key insights into band structure engineering.

In Chapter 3, we introduced a novel three-step procedure to generate the Green's function for both closed and open quantum graphs. This procedure capitalized on the scattering approach, enabling the closed-form calculation of Green's functions even in the presence of complex resonances. The results provided new insights into bound states, perfect scars, and scattering properties in quantum graphs, addressing challenges posed by divergent trajectory-based methods. We extended this approach to periodic graphs and derived the Green's function for infinite lattice systems, showcasing its versatility in modeling periodic structures. The method proved to be a powerful analytical tool, bridging the gap between finite and periodic systems, and setting the stage for its application to the study of metamaterials.

In Chapter 4, we applied quantum graph theory to the design of acoustic metamaterials, demonstrating how the network of interconnected waveguides could be modeled as a graph with space-coiled wave propagation. The flexibility and efficiency of the model allowed for the exploration of large parameter spaces and dispersive properties, and its predictions were experimentally verified using an acoustic metasurface connected to the graph structure. Notably, we designed a system that exhibited negative refraction without explicitly requiring a negative refractive index, driven entirely by the hyperbolic dispersion observed in the anisotropic configuration. This chapter underscored the practical utility of quantum graphs in modeling metamaterials, while also highlighting a limitation of the current approach when considering radiative losses, pointing towards future improvements involving lossy systems.

In Chapter 5, we presented a novel angular filter designed using quantum graph theory. This filter allows wave transmission at customizable angles while maintaining unit reflectivity, a result of the resonance conditions engineered into the periodic quantum graph structure. By coupling an infinite 1D periodic interface with non-

local vertex connections, we demonstrated the filter's selective wave transmission and reflection properties, driven by a shift in boundary conditions from Dirichlet to periodic at specific angles. Although formal homogenization of such structures remains an open question, COMSOL simulations of a continuous waveguide system confirmed that the quantum graph filter's functionality persisted in continuous systems, making it a promising candidate for real-world applications. The proposed filter is expected to have significant impact in fields such as optical computing, edge detection, medical imaging, and autonomous navigation, among others.

This thesis makes several important contributions to both the theory and application of quantum graphs. First, it extends the mathematical framework of quantum graph theory, offering new tools for analyzing scattering and resonance phenomena in both finite and periodic systems. The development of the Green's function procedure and the study of vertex boundary conditions were particularly notable in advancing the theoretical understanding of quantum graphs. Second, we applied these theoretical insights to the design of metamaterials and wave filtering devices, demonstrating their practicality in real-world scenarios. The acoustic metamaterial and angular wave filter presented in this work showcase the potential of quantum graphs in innovative waveguide and filtering technologies.

Several open questions remain, particularly regarding the formal homogenization of quantum graphs with non-local vertex connections. Future work should explore the integration of lossy systems to better model radiative regimes, as well as the experimental realization of quantum graph-based devices in other scalar wave regimes such as electromagnetism. The groundwork laid by this thesis will serve as a foundation for future advancements in quantum graph theory and its applications to complex wave systems, with potential to impact a wide range of technological fields.

A Derivation of coefficients in the Green's function in terms of the resolvent matrix of the quantum map

For any given edge $e \in \mathcal{E}$, we will denote its complement as

$$\mathcal{E}^e \equiv \mathcal{E} \setminus \{e\} \ . \tag{168}$$

Analogously, we write $\mathcal{B}^e = \mathcal{B} \setminus \{e\}$ if $e \in \mathcal{B}$ or $\mathcal{L}^e = \mathcal{L} \setminus \{e\}$ if $e \in \mathcal{L}$. For any given edge e, we may now write the quantum map in block form (after appropriate reordering of the directed edges), that is,

$$\mathbf{U} = \begin{pmatrix} \mathbf{U}_{ee} & \mathbf{U}_{e\mathcal{B}^e} \\ \mathbf{U}_{\mathcal{B}^e e} & \mathbf{U}_{\mathcal{B}^e\mathcal{B}^e} \end{pmatrix} \ , \tag{169}$$

where $\mathbf{U}_{ee}$, $\mathbf{U}_{e\mathcal{B}^e}$, $\mathbf{U}_{\mathcal{B}^e e}$ and $\mathbf{U}_{\mathcal{B}^e\mathcal{B}^e}$ are matrices of dimension 2×2, $2 \times 2(N_\mathcal{B} - 1)$, $2(N_\mathcal{B}-1)\times 2$ and $2(N_\mathcal{B}-1)\times 2(N_\mathcal{B}-1)$, respectively. Eliminating the $\mathbf{a}_\mathcal{B}^{\text{in}}$ components in (23), we can write the quantization condition with the help of the unitary 2×2 matrix $\mathbf{U}(k)^{\text{red},e}$ defined as

$$\mathbf{U}^{\text{red},e} = \mathbf{U}_{ee} + \mathbf{U}_{e\mathcal{B}^e} \left(\mathbb{I} - \mathbf{U}_{\mathcal{B}^e\mathcal{B}^e}\right)^{-1} \mathbf{U}_{\mathcal{B}^e e}. \tag{170}$$

We also define an alternative reduced secular function

$$\xi(k)^{\text{red},e} \equiv \det\left(\mathbb{I} - \mathbf{U}(k)^{\text{red},e}\right), \tag{171}$$

which is related to $\xi(k)$ defined in (24) through the identity

$$\xi(k) = \xi(k)^{\text{red},e} \det\left(\mathbb{I} - \mathbf{U}(k)_{\mathcal{B}^e\mathcal{B}^e}\right). \tag{172}$$

The relation above is obtained using the decomposition

$$\mathbb{I} - \mathbf{U} = \begin{pmatrix} \mathbb{I} - \mathbf{U}^{\mathrm{red,e}} & -\mathbf{U}_{e\mathcal{B}^e} \left(\mathbb{I} - \mathbf{U}_{\mathcal{B}^e\mathcal{B}^e}\right)^{-1} \\ 0 & \mathbb{I} \end{pmatrix} \begin{pmatrix} \mathbb{I} & 0 \\ -\mathbf{U}_{\mathcal{B}^e e} & \mathbb{I} - \mathbf{U}_{\mathcal{B}^e\mathcal{B}^e} \end{pmatrix}. \tag{173}$$

Note that the reduced quantum map $\mathbf{U}^{\mathrm{red},e}$ is related to the quantum scattering matrix $\boldsymbol{\sigma}(k)$ introduced in equation (74) by

$$\mathbf{U}^{\mathrm{red,e}} = \begin{pmatrix} \mathbf{U}^{\mathrm{red,e}}_{e^+e^+} & \mathbf{U}^{\mathrm{red,e}}_{e^+e^-} \\ \mathbf{U}^{\mathrm{red,e}}_{e^-e^+} & \mathbf{U}^{\mathrm{red,e}}_{e^-e^-} \end{pmatrix} = e^{ik\ell_e} \begin{pmatrix} \sigma_{\mathrm{TH}} & \sigma_{\mathrm{TT}} \\ \sigma_{\mathrm{HH}} & \sigma_{\mathrm{HT}} \end{pmatrix}. \tag{174}$$

In order to obtain the second line in (78), we note that the denominator in these expressions can be written in terms of the reduced secular function of the compact graph, that is,

$$\left[(1 - e^{ik\ell_{e'}}\sigma_{\mathrm{HT}})(1 - e^{ik\ell_{e'}}\sigma_{\mathrm{TH}}) - e^{2ik\ell_{e'}}\sigma_{\mathrm{HH}}\sigma_{\mathrm{TT}}\right] = \xi(k)^{\mathrm{red},e'}\ , \tag{175}$$

where we use the e' notation as in section 3.2.1.

By writing out the resolvent of the reduced 2×2 quantum map, that is,

$$\frac{\mathbb{I}}{\mathbb{I} - \mathbf{U}^{\mathrm{red},e'}} \equiv \begin{pmatrix} 1 - \mathbf{U}^{\mathrm{red},e'}_{e'_+e'_+} & -\mathbf{U}^{\mathrm{red},e'}_{e'_+e'_-} \\ -\mathbf{U}^{\mathrm{red},e'}_{e'_-e'_+} & 1 - \mathbf{U}^{\mathrm{red},e'}_{e'_-e'_-} \end{pmatrix}^{-1} = \frac{1}{\xi^{\mathrm{red},e'}} \begin{pmatrix} 1 - \mathbf{U}^{\mathrm{red},e'}_{e'_-e'_-} & \mathbf{U}^{\mathrm{red},e'}_{e'_+e'_-} \\ \mathbf{U}^{\mathrm{red},e'}_{e'_-e'_+} & 1 - \mathbf{U}^{\mathrm{red},e'}_{e'_+e'_+} \end{pmatrix}, \tag{176}$$

we can relate the terms in (78) to matrix elements of the inverse of the reduced quantum map using again (174). The expressions as given in equation (78) are now obtained observing in addition

$$\frac{\mathbb{I}}{\mathbb{I} - \mathbf{U}^{\mathrm{red},e'}} = \left[\frac{\mathbb{I}}{\mathbb{I} - \mathbf{U}}\right]_{e'e'}, \tag{177}$$

which follows, for example, from the decomposition (173).

B Details on the pole contribution to the Green's function in compact graphs

In this appendix, we want to give a detailed derivation of equations (83) and (84) that define the pole contribution of the Green's function at an energy eigenvalue $E_n = k_n^2$. With the orthogonal projector $\mathbf{Q} = \mathbb{I} - \mathbf{P}$ let us start by writing

$$\begin{aligned}\frac{\mathbf{U}(k_+)}{\mathbb{I}-\mathbf{U}(k_+)} =& -\mathbb{I} + \frac{1}{\chi(k_+)}\mathbf{P} \\ &+ \mathbf{P}\frac{\mathbb{I}}{\mathbb{I}-\mathbf{U}(k_+)}\mathbf{Q} + \mathbf{Q}\frac{\mathbb{I}}{\mathbb{I}-\mathbf{U}(k_+)}\mathbf{P} + \mathbf{Q}\frac{\mathbb{I}}{\mathbb{I}-\mathbf{U}(k_+)}\mathbf{Q}\end{aligned} \tag{178}$$

where

$$\chi(k_+) = \left(\mathbf{b}^{\text{in}\dagger}\frac{\mathbb{I}}{\mathbb{I}-\mathbf{U}(k_+)}\mathbf{b}^{\text{in}}\right)^{-1} \tag{179}$$

and we have used that $\mathbf{P} = \mathbf{b}^{\text{in}}\mathbf{b}^{\text{in}\dagger}$ is a rank one projector. We will show that, as $k_+ \to k_n$, the only singular term in (178) is contained in $\frac{1}{\chi(k_+)}\mathbf{P}$. Writing

$$\frac{\mathbb{I}}{\mathbb{I}-\mathbf{U}(k_+)}\left(\mathbf{P}+\mathbf{Q}\right)\left(\mathbf{I}-\mathbf{U}(k_+)\right) = \mathbb{I}\,, \tag{180}$$

and multiplying it from left and right with either $\mathbf{P}$ or $\mathbf{Q}$ results in four equations that may be solved for

$$\chi(k_+) = \mathbf{b}^{\text{in}\dagger}\left[\mathbb{I}-\mathbf{U}(k_+)-\mathbf{U}(k_+)\mathbf{Q}\frac{\mathbb{I}}{\mathbb{I}-\mathbf{Q}\mathbf{U}(k_+)\mathbf{Q}}\mathbf{Q}\mathbf{U}(k_+)\right]\mathbf{b}^{\text{in}} \tag{181a}$$

$$\mathbf{P}\frac{\mathbb{I}}{\mathbb{I}-\mathbf{U}(k_+)}\mathbf{Q} = \frac{1}{\chi(k_+)}\mathbf{P}\mathbf{U}(k_+)\mathbf{Q}\frac{\mathbb{I}}{\mathbb{I}-\mathbf{Q}\mathbf{U}(k_+)\mathbf{Q}}\mathbf{Q} \tag{181b}$$

$$\mathbf{Q}\frac{\mathbb{I}}{\mathbb{I}-\mathbf{U}(k_+)}\mathbf{P} = \frac{1}{\chi(k_+)}\mathbf{Q}\frac{\mathbb{I}}{\mathbb{I}-\mathbf{Q}\mathbf{U}(k_+)\mathbf{Q}}\mathbf{Q}\mathbf{U}(k_+)\mathbf{P} \tag{181c}$$

$$\mathbf{Q}\frac{\mathbb{I}}{\mathbb{I}-\mathbf{U}(k_+)}\mathbf{Q} = \mathbf{Q} + \frac{1}{\chi(k_+)}\mathbf{Q}\frac{\mathbb{I}}{\mathbb{I}-\mathbf{Q}\mathbf{U}(k_+)\mathbf{Q}}\mathbf{Q}\mathbf{U}(k_+)\mathbf{P}\mathbf{U}(k_+)\mathbf{Q}\frac{\mathbb{I}}{\mathbb{I}-\mathbf{Q}\mathbf{U}(k_+)\mathbf{Q}}\mathbf{Q} \tag{181d}$$

using standard properties of orthogonal projectors such as $\mathbf{P}^2 = \mathbf{P}$, $\mathbf{Q}^2 = \mathbf{Q}$, and $\mathbf{PQ} = \mathbf{QP} = 0$. Now let us write $k = k_n + \delta k$ and consider $\delta k \to 0$ using the Taylor expansion

$$\mathbf{U}(k_n + \delta k) = \mathbf{U}(k_n) + \frac{d\mathbf{U}}{dk}(k_n)\ \delta k + O((\delta k)^2)\ . \tag{182}$$

The derivative of the quantum map $\mathbf{U}(k)$ can be performed explicitly. The latter depends on the wave number via phases $e^{ik\ell_e}$ on each edge e, and in general also via an explicit k dependence of the vertex scattering matrices. For the vertex scattering matrices of the form (9), one finds, using standard matrix algebra,

$$\frac{d}{dk}\mathbf{\Sigma}^{(v)}(k) = \frac{1}{2k}\left(\mathbb{I} - \mathbf{\Sigma}^{(v)}(k)^2\right)\ . \tag{183}$$

Then the derivative of $\mathbf{U}(k) = e^{ik\mathbf{L}}\mathbf{\Pi\Sigma}$ gives

$$\frac{d\mathbf{U}}{dk}(k) = i\mathbf{L}\mathbf{U}(k) + \frac{1}{2k}\left[e^{ik\mathbf{L}}\mathbf{\Pi} - \mathbf{U}(k)e^{-ik\mathbf{L}}\mathbf{\Pi}\mathbf{U}(k)\right]\ . \tag{184}$$

At this stage we may identify that the constant C stated in (84) is just

$$C = \frac{1}{i}\mathbf{b}^{\mathrm{in}\dagger}\ \frac{d\mathbf{U}}{dk}(k_n)\mathbf{b}^{\mathrm{in}}\ . \tag{185}$$

The expressions (182) and (184) have the following implications

$$\mathbf{PU}(k + \delta k)\mathbf{Q} = O(\delta k) \tag{186a}$$

$$\mathbf{QU}(k + \delta k)\mathbf{P} = O(\delta k) \tag{186b}$$

$$\chi(k + \delta k) = -\,iC\delta k + O((\delta k)^2) \tag{186c}$$

such that $\mathbf{P}\frac{\mathbb{I}}{\mathbb{I}-\mathbf{U}(k)}\mathbf{Q}$, $\mathbf{Q}\frac{\mathbb{I}}{\mathbb{I}-\mathbf{U}(k)}\mathbf{P}$ and $\mathbf{Q}\frac{\mathbb{I}}{\mathbb{I}-\mathbf{U}(k)}\mathbf{Q}$ are not singular in the limit $\delta k \to 0$ and we are left with the singular part

$$\frac{\mathbf{U}(k_n + \delta k)}{\mathbb{I} - \mathbf{U}(k_n + \delta k)} = \frac{1}{-iC\delta k}\mathbf{P} + O((\delta k)^0) \tag{187}$$

which is equivalent to the equation (83) we wanted to prove in this appendix.

C Details of the derivation of the Green's function in open scattering graphs

In this appendix, we give details how the Green's function (86) for an open scattering graph $\mathcal{G}$ can be derived from the Green's function (79) of an auxiliary compact graph $\mathcal{G}_{\text{aux}}$ by sending the edge lengths of those edges turning into leads to infinity. Note that one has to send the lengths to infinity while the imaginary part of k_+ is positive. The auxiliary graph $\mathcal{G}_{\text{aux}}$ is obtained from the open graph $\mathcal{G}$ by replacing each lead by an edge of finite length with a vertex of degree one at the other end. For simplicity, we will put Neumann-Kirchhoff conditions at the vertices of degree one, the final results will not depend on this choice. For the sake of this derivation, we will bend the use of notation and continue to refer to 'leads' and 'bonds' of the auxiliary graph. Let us also introduce the $N_{\mathcal{L}}$-dimensional diagonal matrix $\mathbf{L}_{\mathcal{L}} = \text{diag}(\ell_{\text{e}} : \text{e} \in \mathcal{L})$ that contains the edge lengths of the leads. We start from the Green's function for the auxiliary graph (79). It contains four matrix elements of the matrix $\mathbf{R} = \frac{\mathbf{U}^{\text{aux}}}{\mathbb{I}-\mathbf{U}^{\text{aux}}}$ where we denote the $(2(N_{\mathcal{B}}+N_{\mathcal{L}})$-dimensional) quantum map of the auxiliary graph by $\mathbf{U}^{\text{aux}}$ in order to distinguish it from the $(2N_{\mathcal{B}}+N_{\mathcal{L}}$-dimensional) quantum map $\mathbf{U}$ of the open graph. We suppress the dependence on k_+ here, as it can be reintroduced easily at the end of the calculation. The standard way to continue the calculation would be to decompose the involved matrices into blocks that correspond to three sets of directed edges: directed bonds $\mathcal{B}$, outgoing leads $\mathcal{L}_+$ and incoming leads $\mathcal{L}_-$. For the quantum map of the auxiliary graph the structure of the graph then implies

$$\mathbf{U}^{\text{aux}} = \begin{pmatrix} \mathbf{U}^{\text{aux}}_{\mathcal{L}_+\mathcal{L}_+} & \mathbf{U}^{\text{aux}}_{\mathcal{L}_+\mathcal{L}_-} & \mathbf{U}^{\text{aux}}_{\mathcal{L}_+\mathcal{B}} \\ \mathbf{U}^{\text{aux}}_{\mathcal{L}_-\mathcal{L}_+} & \mathbf{U}^{\text{aux}}_{\mathcal{L}_-\mathcal{L}_-} & \mathbf{U}^{\text{aux}}_{\mathcal{L}_-\mathcal{B}} \\ \mathbf{U}^{\text{aux}}_{\mathcal{B}\mathcal{L}_+} & \mathbf{U}^{\text{aux}}_{\mathcal{B}\mathcal{L}_-} & \mathbf{U}^{\text{aux}}_{\mathcal{B}\mathcal{B}} \end{pmatrix} = \begin{pmatrix} 0 & \mathbf{T}_{\mathcal{L}}\mathbf{U}_{\mathcal{L}\mathcal{L}} & \mathbf{T}_{\mathcal{L}}\mathbf{U}_{\mathcal{L}\mathcal{B}} \\ \mathbf{T}_{\mathcal{L}} & 0 & 0 \\ 0 & \mathbf{U}_{\mathcal{B}\mathcal{L}} & \mathbf{U}_{\mathcal{B}\mathcal{B}} \end{pmatrix} \tag{188}$$

where four blocks vanish due to the connectivity of the auxiliary graph, the other four blocks can been identified with corresponding blocks of the quantum map of the open graph and we introduced $\mathbf{T}_{\mathcal{L}} \equiv e^{ik_+\mathbf{L}_{\mathcal{L}}}$, an $N_{\mathcal{L}}$-dimensional diagonal matrix that contains the auxiliary lengths of the leads in the phase. Note, that $\mathbf{T}_{\mathcal{L}} \to 0$ as the auxiliary lengths are sent to infinity. Writing the identity $\mathbf{U}^{\text{aux}} = \mathbf{R} - \mathbf{U}^{\text{aux}}\mathbf{R}$ in terms of its blocks one may express the blocks of $\mathbf{R}$ in the form

$$\begin{aligned}\mathbf{R} &= \begin{pmatrix} \mathbf{R}_{\mathcal{L}_+\mathcal{L}_+} & \mathbf{R}_{\mathcal{L}_+\mathcal{L}_-} & \mathbf{R}_{\mathcal{L}_+\mathcal{B}} \\ \mathbf{R}_{\mathcal{L}_-\mathcal{L}_+} & \mathbf{R}_{\mathcal{L}_-\mathcal{L}_-} & \mathbf{R}_{\mathcal{L}_-\mathcal{B}} \\ \mathbf{R}_{\mathcal{B}\mathcal{L}_+} & \mathbf{R}_{\mathcal{B}\mathcal{L}_-} & \mathbf{R}_{\mathcal{B}\mathcal{B}} \end{pmatrix} \\ &= \begin{pmatrix} \mathbf{T}_{\mathcal{L}}\boldsymbol{\sigma}\frac{\mathbb{I}}{\mathbb{I}-\mathbf{T}_{\mathcal{L}}^2\boldsymbol{\sigma}}\mathbf{T}_{\mathcal{L}} & \mathbf{T}_{\mathcal{L}}\boldsymbol{\sigma}\frac{\mathbb{I}}{\mathbb{I}-\mathbf{T}_{\mathcal{L}}^2\boldsymbol{\sigma}} & \mathbf{T}_{\mathcal{L}}\frac{\mathbb{I}}{\mathbb{I}-\boldsymbol{\sigma}\mathbf{T}_{\mathcal{L}}^2}\boldsymbol{\rho}^{\text{out}} \\ \frac{\mathbb{I}}{\mathbb{I}-\mathbf{T}_{\mathcal{L}}^2\boldsymbol{\sigma}}\mathbf{T}_{\mathcal{L}} & \frac{\mathbf{T}_{\mathcal{L}}^2\boldsymbol{\sigma}}{\mathbb{I}-\mathbf{T}_{\mathcal{L}}^2\boldsymbol{\sigma}} & \mathbf{T}_{\mathcal{L}}^2\frac{\mathbb{I}}{\mathbb{I}-\boldsymbol{\sigma}\mathbf{T}_{\mathcal{L}}^2}\boldsymbol{\rho}^{\text{out}} \\ \boldsymbol{\rho}^{\text{in}}\frac{\mathbb{I}}{\mathbb{I}-\mathbf{T}_{\mathcal{L}}^2\boldsymbol{\sigma}}\mathbf{T}_{\mathcal{L}} & \boldsymbol{\rho}^{\text{in}}\frac{\mathbb{I}}{\mathbb{I}-\mathbf{T}_{\mathcal{L}}^2\boldsymbol{\sigma}} & \frac{\mathbf{U}_{\mathcal{B}\mathcal{B}}}{\mathbb{I}-\mathbf{U}_{\mathcal{B}\mathcal{B}}} + \boldsymbol{\rho}^{\text{in}}\mathbf{T}_{\mathcal{L}}^2\frac{\mathbb{I}}{\mathbb{I}-\boldsymbol{\sigma}\mathbf{T}_{\mathcal{L}}^2}\boldsymbol{\rho}^{\text{out}} \end{pmatrix}\end{aligned} \tag{189}$$

where $\boldsymbol{\sigma} \equiv \mathbf{U}_{\mathcal{L}\mathcal{L}} + \mathbf{U}_{\mathcal{L}\mathcal{B}}\frac{\mathbb{I}}{\mathbb{I}-\mathbf{U}_{\mathcal{B}\mathcal{B}}}\mathbf{U}_{\mathcal{B}\mathcal{L}}$ is the scattering matrix of the open graph, $\boldsymbol{\rho}^{\text{in}} = \frac{\mathbb{I}}{\mathbb{I}-\mathbf{U}_{\mathbf{B}\mathbf{B}}}\mathbf{U}_{\mathcal{B}\mathcal{L}}$ and $\boldsymbol{\rho}^{\text{out}} = \mathbf{U}_{\mathcal{L}\mathcal{B}}\frac{\mathbb{I}}{\mathbb{I}-\mathbf{U}_{\mathbf{B}\mathbf{B}}}$.

To proceed one chooses two points $\mathbf{z} = (z_e, e)$ and $\mathbf{z}' = (z_{e'}, e')$ on the auxiliary graph $\mathcal{G}^{\text{aux}}$ and expresses the Green's function (79) of $\mathcal{G}^{\text{aux}}$ in terms of appropriate matrix elements of $\mathbf{R}$ and then performs the limit $\mathbf{T}_{\mathcal{L}} \to 0$. Let us do this explicitly for $e, e' \in \mathcal{L}$ and write (79) for this case in the form

$$\begin{aligned}2k_+i\, G^{\text{aux}}(\mathbf{z},\mathbf{z}',E_+) =& \delta_{e,e'}\, e^{ik_+|z_e - z'_{e'}|} + e^{ik_+(z_e - z'_{e'})}\left[\mathbf{T}_{\mathcal{L}}^{-1}\mathbf{R}_{\mathcal{L}_+\mathcal{L}_+}\mathbf{T}_{\mathcal{L}}\right]_{ee'} \\ &+ e^{-ik_+(z_e - z'_{e'})}\left[\mathbf{R}_{\mathcal{L}_-\mathcal{L}_-}\right]_{ee'} + e^{ik_+(z_e + z'_{e'})}\left[\mathbf{T}_{\mathcal{L}}^{-1}\mathbf{R}_{\mathcal{L}_+\mathcal{L}_-}\right]_{ee'} \\ &+ e^{ik_+(z_e + z'_{e'})}\left[\mathbf{R}_{\mathcal{L}_-\mathcal{L}_+}\mathbf{T}_{\mathcal{L}}\right]_{ee'} \\ =& \delta_{e,e'}\, e^{ik_+|z_e - z'_{e'}|} + e^{ik_+(z_e - z'_{e'})}\left[\frac{\boldsymbol{\sigma}\mathbf{T}_{\mathcal{L}}^2}{\mathbb{I}-\boldsymbol{\sigma}\mathbf{T}_{\mathcal{L}}^2}\right]_{ee'} \\ &+ e^{-ik_+(z_e - z'_{e'})}\left[\frac{\mathbf{T}_{\mathcal{L}}^2\boldsymbol{\sigma}}{\mathbb{I}-\mathbf{T}_{\mathcal{L}}^2\boldsymbol{\sigma}}\right]_{ee'} + e^{ik_+(z_e + z'_{e'})}\left[\boldsymbol{\sigma}\frac{\mathbb{I}}{\mathbb{I}-\mathbf{T}_{\mathcal{L}}^2\boldsymbol{\sigma}}\right]_{ee'} \\ &+ e^{ik_+(z_e + z'_{e'})}\left[\frac{\mathbb{I}}{\mathbb{I}-\mathbf{T}_{\mathcal{L}}^2\boldsymbol{\sigma}}\mathbf{T}_{\mathcal{L}}^2\right]_{ee'}\end{aligned} \tag{190}$$

where we may now send the edge lengths of the leads to infinity $\mathbf{T}_{\mathcal{L}} \to 0$. This results in

$$2k_+ i\ G(\mathbf{z}, \mathbf{z}', E_+) = \delta_{e,e'}\, e^{ik_+|z_e - z'_{e'}|} + e^{ik_+(z_e + z'_{e'})} \boldsymbol{\sigma}_{ee'} \tag{191}$$

which is equivalent to the given expression for the open Green's function (86) if both points are on the leads. The other cases can be derived in the same way. This calculation is equivalent to formally expanding the Green's function of the auxiliary graph as a sum over trajectories. Sending the lengths of the leads to infinity is equivalent to only summing over trajectories that never travel through any lead from one end to the other - summing just these trajectories then gives back (86).

D Regularity of the scattering matrix $\boldsymbol{\sigma}$ at a bound state in the continuum

Following on from the discussion in section 3.3, we show here that the singularity of the scattering matrix $\boldsymbol{\sigma}(k)$ and the coupling matrix $\boldsymbol{\rho}(k)$, Eqs. (34) and (36), in the presence of a perfect scar (described by the eigenvector $\mathbf{b}_0$) can be lifted and that the solution is regular across a whole k interval containing k_0.

D.1 Closed expressions for $\mathbf{P}\boldsymbol{\rho}(k)$

First, we decompose the internal graph amplitudes of a scattering solution (35), that is, $\mathbf{a}(k)^{\text{in}}_{\mathcal{B}} = \boldsymbol{\rho}(k)\mathbf{a}^{\text{in}}_{\mathcal{L}}$, into components parallel and orthogonal to $\mathbf{b}_0$,

$$\mathbf{P}\,\mathbf{a}(k)^{\text{in}}_{\mathcal{B}} + \mathbf{Q}\,\mathbf{a}(k)^{\text{in}}_{\mathcal{B}} = (\mathbf{P}\boldsymbol{\rho}(k) + \mathbf{Q}\boldsymbol{\rho}(k))\,\mathbf{a}^{\text{in}}_{\mathcal{L}}, \tag{192}$$

where the projection operator and its orthogonal component are defined in (92) and (93). Starting from equation (94), we write

$$\begin{aligned}\mathbf{P}\,(\mathbb{I}-\mathbf{U}(k)_{\mathcal{B}\mathcal{B}})\,(\mathbf{P}+\mathbf{Q})\,\mathbf{a}^{\text{in}}_{\mathcal{B}} &= \mathbf{P}\mathbf{U}(k)_{\mathcal{B}\mathcal{L}}\,\mathbf{a}^{\text{in}}_{\mathcal{L}},\\ \mathbf{Q}\,(\mathbb{I}-\mathbf{U}(k)_{\mathcal{B}\mathcal{B}})\,(\mathbf{P}+\mathbf{Q})\,\mathbf{a}^{\text{in}}_{\mathcal{B}} &= \mathbf{Q}\mathbf{U}(k)_{\mathcal{B}\mathcal{L}}\,\mathbf{a}^{\text{in}}_{\mathcal{L}},\end{aligned}$$

which yields

$$\left(\mathbf{b}^{\text{in}\,\dagger}_{\mathcal{B}}\,(\mathbb{I}-\mathbf{U}(k)_{\mathcal{B}\mathcal{B}})\,\mathbf{b}^{\text{in}}_{\mathcal{B}}\right)\cdot\mathbf{P}\,\mathbf{a}^{\text{in}}_{\mathcal{B}}-\mathbf{P}\mathbf{U}(k)_{\mathcal{B}\mathcal{B}}\mathbf{Q}\,\mathbf{a}^{\text{in}}_{\mathcal{B}} = \mathbf{P}\mathbf{U}(k)_{\mathcal{B}\mathcal{L}}\,\mathbf{a}^{\text{in}}_{\mathcal{L}}, \quad (193a)$$

$$-\mathbf{Q}\mathbf{U}(k)_{\mathcal{B}\mathcal{B}}\mathbf{P}\,\mathbf{a}^{\text{in}}_{\mathcal{B}}+\mathbf{Y}_Q(k)\mathbf{Q}\,\mathbf{a}^{\text{in}}_{\mathcal{B}} = \mathbf{Q}\mathbf{U}(k)_{\mathcal{B}\mathcal{L}}\,\mathbf{a}^{\text{in}}_{\mathcal{L}}, \quad (193b)$$

where $\mathbf{Y}_Q(k)$ has been defined in (96) We have defined $\mathbf{Y}_Q(k)^{-1}$ in (97) as the inverse on the reduced space spanned by $\mathbf{Q}$. Note that these definitions are here extended to wave numbers close to k_0 while $\mathbf{P}$ and $\mathbf{Q}$ do not depend on k. We used the general relation $\mathbf{PAP}=\left(\mathbf{b}^{\text{in}\,\dagger}_{\mathcal{B}}\mathbf{A}\mathbf{b}^{\text{in}}_{\mathcal{B}}\right)\cdot\mathbf{P}$ for a square matrix $\mathbf{A}$. After rearranging (193b) by multiplying with $\mathbf{Y}_Q(k)^{-1}$ and replacing $\mathbf{a}(k)^{\text{in}}_{\mathcal{B}}$ by $\boldsymbol{\rho}(k)\,\mathbf{a}^{\text{in}}_{\mathcal{L}}$, we obtain

$$\mathbf{Q}\boldsymbol{\rho}(k)=\mathbf{Y}_Q(k)^{-1}\mathbf{U}(k)_{\mathcal{B}\mathcal{B}}\mathbf{P}\boldsymbol{\rho}(k)+\mathbf{Y}_Q(k)^{-1}\mathbf{U}(k)_{\mathcal{B}\mathcal{L}}\,. \quad (194)$$

Given that $\mathbf{b}^{\text{in}\,\dagger}_{\mathcal{B}}\,(\mathbb{I}-\mathbf{U}(k)_{\mathcal{B}\mathcal{B}})\,\mathbf{b}^{\text{in}}_{\mathcal{B}}$ in (193a) is a scalar and after replacing $\mathbf{Q}\,\mathbf{a}^{\text{in}}_{\mathcal{B}}$ by $\mathbf{Q}\boldsymbol{\rho}(k)\,\mathbf{a}^{\text{in}}_{\mathcal{L}}$ using (194), one obtains after some further manipulations

$$\mathbf{P}\boldsymbol{\rho}(k)=\mathbf{P}\frac{\mathbb{I}+\mathbf{U}(k)_{\mathcal{B}\mathcal{B}}\mathbf{Y}_Q(k)^{-1}}{\mathbf{b}^{\text{in}\,\dagger}_{\mathcal{B}}\,[\mathbb{I}-\mathbf{U}(k)_{\mathcal{B}\mathcal{B}}-\mathbf{U}(k)_{\mathcal{B}\mathcal{B}}\mathbf{Y}_Q(k)^{-1}\mathbf{U}(k)_{\mathcal{B}\mathcal{B}}]\,\mathbf{b}^{\text{in}}_{\mathcal{B}}}\mathbf{U}(k)_{\mathcal{B}\mathcal{L}}. \quad (195)$$

In order to analyse the scattering solutions in the vicinity of the bound state, we consider wave numbers k close to k_0 in the limit $\delta k\equiv k-k_0\to 0$ in the matrices $\boldsymbol{\sigma}(k)$ and $\boldsymbol{\rho}(k)$. By construction we have $\mathbf{Y}_Q(k)\mathbf{b}^{\text{in}}_{\mathcal{B}}=0$ and $\mathbf{Y}_Q(k)^{-1}$ has been defined on the subspace spanned by the projector $\mathbf{Q}$ in order to remove the pole at k_0. For wave numbers k sufficiently close to k_0 this definition remains well defined due to

the (assumed) non-degeneracy of $\mathbf{U}(k)$ as the matrix is then free of poles.

D.2 Expansion of $\mathbf{P}\boldsymbol{\rho}(k)$ around $k = k_0$

We will show in the following that, as $k \to k_0$ in (195), the denominator,

$$\mathbf{b}_{\mathcal{B}}^{\text{in}\,\dagger} \left[\mathbb{I} - \mathbf{U}(k)_{\mathcal{B}\mathcal{B}} - \mathbf{U}(k)_{\mathcal{B}\mathcal{B}}\mathbf{Y}_Q(k)^{-1}\mathbf{U}(k)_{\mathcal{B}\mathcal{B}}\right] \mathbf{b}_{\mathcal{B}}^{\text{in}}, \tag{196}$$

vanishes but so does the numerator. We will show this for vertex scattering matrices of the form (9) by performing a Taylor expansion of both expressions around $k = k_0$. For this, we need to find explicit expressions for the derivative of the blocks of the quantum map $\mathbf{U}(k)$. The calculation of these is similar to the one performed in Appendix B using equation (183). When this equation is applied here to the full quantum map $\mathbf{U}$, one obtains

$$\frac{d}{dk}\mathbf{U}(k) = \begin{pmatrix} 0 & 0 \\ 0 & i\mathbf{L} \end{pmatrix} \mathbf{U}(k) + \frac{1}{2k}\left[\begin{pmatrix} \mathbb{I} & 0 \\ 0 & e^{ik\mathbf{L}}\mathbf{\Pi} \end{pmatrix} - \mathbf{U}(k)\begin{pmatrix} \mathbb{I} & 0 \\ 0 & e^{-ik\mathbf{L}}\mathbf{\Pi} \end{pmatrix}\mathbf{U}(k)\right], \tag{197}$$

where $\mathbf{L}$ and $\exp(-ik\mathbf{L})$ are $2N_B$- dimensional diagonal matrices with diagonal entries ℓ_e and $\exp(-ik\ell_e)$, respectively. Setting $k = k_0 + \delta k$, we find the expansions

$$\begin{aligned}
\mathbf{U}(k_0+\delta k)_{\mathcal{B}\mathcal{B}} =& \mathbf{U}(k_0)_{\mathcal{B}\mathcal{B}} + i\delta k \mathbf{L}\mathbf{U}(k_0)_{\mathcal{B}\mathcal{B}} \\
&+ \frac{\delta k}{2k_0}\left(e^{ik_0\mathbf{L}}\mathbf{\Pi} - \mathbf{U}(k_0)_{\mathcal{B}\mathcal{B}}e^{-ik_0\mathbf{L}}\mathbf{\Pi}\mathbf{U}(k_0)_{\mathcal{B}\mathcal{B}}\right) \\
&- \frac{\delta k}{2k_0}\mathbf{U}(k_0)_{\mathcal{B}\mathcal{L}}\mathbf{U}(k_0)_{LB} + O((\delta k)^2) \qquad (198a) \\
\mathbf{U}(k_0+\delta k)_{\mathcal{B}\mathcal{L}} =& \mathbf{U}(k_0)_{\mathcal{B}\mathcal{L}} + i\delta k \mathbf{L}\mathbf{U}(k_0)_{\mathcal{B}\mathcal{L}} \\
&- \frac{\delta k}{2k_0}\mathbf{U}(k_0)_{\mathcal{B}\mathcal{B}}e^{-ik_0\mathbf{L}}\mathbf{\Pi}\mathbf{U}(k_0)_{\mathcal{B}\mathcal{L}} \\
&- \frac{\delta k}{2k_0}\mathbf{U}(k_0)_{\mathcal{B}\mathcal{L}}\mathbf{U}(k_0)_{\mathcal{L}\mathcal{L}} + O((\delta k)^2)\ . \qquad (198b)
\end{aligned}$$

As $\mathbf{b}_{\mathcal{B}}^{\text{in}}$ is a normalized eigenvector of $\mathbf{U}(k_0)_{\mathcal{BB}}$ with eigenvalue one and as $\mathbf{U}(k_0)_{\mathcal{LB}}\mathbf{b}_{\mathcal{B}}^{\text{in}} = 0$, $\mathbf{b}_{\mathcal{B}}^{\text{in}\dagger}\mathbf{U}(k_0)_{\mathcal{BL}} = 0$ due to the unitarity of $\mathbf{U}(k_0)$, one gets

$$\mathbf{b}_{\mathcal{B}}^{\text{in}\dagger}\mathbf{U}(k_0+\delta k)_{\mathcal{BB}}\mathbf{b}_{\mathcal{B}}^{\text{in}} = 1 + i\delta k\mathbf{b}_{\mathcal{B}}^{\text{in}\dagger}\left(\mathbf{L} + \frac{\sin(k_0\mathbf{L})}{k_0}\mathbf{\Pi}\right)\mathbf{b}_{\mathcal{B}}^{\text{in}} + O((\delta k)^2) \tag{199}$$

and

$$\mathbf{b}_{\mathcal{B}}^{\text{in}\dagger}\mathbf{U}(k_0+\delta k)_{\mathcal{BB}}\mathbf{Y}_Q(k_0+\delta k)^{-1}\mathbf{U}(k_0+\delta k)_{BB}\mathbf{b}_{\mathcal{B}}^{\text{in}} = O((\delta k)^2). \tag{200}$$

The last two equations together give

$$\begin{aligned}\mathbf{b}_{\mathcal{B}}^{\text{in}\dagger}\left[\mathbb{I} - \mathbf{U}(k)_{\mathcal{BB}} - \mathbf{U}(k)_{\mathcal{BB}}\mathbf{Y}_Q(k)^{-1}\mathbf{U}(k)_{\mathcal{BB}}\right]\mathbf{b}_{\mathcal{B}}^{\text{in}} \\ = \; -i\delta k\; \mathbf{b}_{\mathcal{B}}^{\text{in}\dagger}\left[\mathbf{L} + \frac{\sin(\mathbf{L}k_0)}{k_0}\mathbf{\Pi}\right]\mathbf{b}_{\mathcal{B}}^{\text{in}} \; + \; O((\delta k)^2)\,.\end{aligned} \tag{201}$$

Analogously one finds

$$\mathbf{P}\mathbf{U}(k_0+\delta k)_{\mathcal{BL}} = i\mathbf{P}\mathbf{L}\mathbf{U}(k_0)_{\mathcal{BL}}\delta k - \mathbf{P}\frac{\delta k}{2k_0}e^{-ik_0\mathbf{L}}\mathbf{\Pi}\mathbf{U}(k_0)_{\mathcal{BL}} + O((\delta k)^2) \tag{202}$$

and

$$\begin{aligned}&\mathbf{P}\mathbf{U}(k_0+\delta k)_{\mathcal{BB}}\mathbf{Q} = \\ &\qquad \delta k\; \mathbf{P}\left[i\mathbf{L}\mathbf{U}(k_0)_{\mathcal{BB}} + \frac{1}{2k_0}\mathbf{\Pi}\left(e^{ik_0\mathbf{L}} - e^{-ik_0\mathbf{L}}\mathbf{U}(k_0)_{\mathcal{BB}}\right)\right]\mathbf{Q} + O((\delta k)^2)\end{aligned} \tag{203}$$

which together yield

$$\begin{aligned}&\mathbf{P}(\mathbb{I} + \mathbf{U}(k)_{\mathcal{BB}}\mathbf{Y}_Q(k)^{-1})\mathbf{U}(k)_{\mathcal{BL}} = \\ &\qquad\qquad i\delta k\; \mathbf{P}\left[\mathbf{L} - \frac{1}{2k_0 i}\mathbf{\Pi}e^{-ik_0\mathbf{L}}\right]\mathbf{U}(k_0)_{\mathcal{BL}} \\ &+i\delta k\; \mathbf{P}\left[\left(\mathbf{L}\mathbf{U}(k_0)_{\mathcal{BB}} + \mathbf{\Pi}\frac{e^{ik_0\mathbf{L}} - e^{-ik_0\mathbf{L}}\mathbf{U}(k_0)_{\mathcal{BB}}}{2k_0 i}\right)\mathbf{Y}_Q(k_0)^{-1}\right]\mathbf{U}(k_0)_{\mathcal{BL}} + O((\delta k)^2)\,.\end{aligned} \tag{204}$$

Finally, we show that the term $\mathbf{b}_{\mathcal{B}}^{\text{in}\dagger}\left(\mathbf{L}+\frac{1}{k_0}\sin(k_0\mathbf{L})\mathbf{\Pi}\right)\mathbf{b}_{\mathcal{B}}^{\text{in}}$ in (201) does not vanish. This is essential for the limit $\lim_{\delta k\to 0}\mathbf{P}\boldsymbol{\rho}(k+\delta k)$ to be well defined (and finite). Indeed one has

$$\mathbf{b}_{\mathcal{B}}^{\text{in}\dagger}\left(\mathbf{L}+\frac{\sin(k_0\mathbf{L})}{k_0}\mathbf{\Pi}\right)\mathbf{b}_{\mathcal{B}}^{\text{in}}=\sum_{e\in\mathcal{B}}\ell_e(|b_{e_+}|^2+|b_{e_-}|^2)+\frac{\sin(k_0\ell_e)}{k_0}\left(b_{e_+}^*b_{e_-}+b_{e_-}^*b_{e_+}\right) \tag{205}$$

which is a sum over positive terms as (for $k_0>0$)

$$\left|\frac{\sin(k_0\ell_e)}{k_0\ell_e}\left(b_{e_+}^*b_{e_-}+b_{e_-}^*b_{e_+}\right)\right| \quad < \quad \left|\left(b_{e_+}^*b_{e_-}+b_{e_-}^*b_{e_+}\right)\right| \quad \leq \quad |b_{e_+}|^2 \;+\; |b_{e_-}|^2$$

using the Cauchy-Schwartz inequality.

This means that the limit $\mathbf{P}\boldsymbol{\rho}(k_0)\equiv\lim_{\delta k\to 0}\mathbf{P}\boldsymbol{\rho}(k_0+\delta k)$ is well defined and we obtain to leading order

$$\mathbf{P}\boldsymbol{\rho}(k_0)=\frac{\mathbf{P}\left[\frac{1}{2i}\mathbf{\Pi}e^{-ik_0\mathbf{L}}-k_0\mathbf{L}-\left(k_0\mathbf{L}\mathbf{U}_{\mathcal{B}\mathcal{B}}+\mathbf{\Pi}\frac{e^{ik_0\mathbf{L}}-e^{-ik_0\mathbf{L}}\mathbf{U}_{\mathcal{B}\mathcal{B}}}{2i}\right)\mathbf{Y}_Q^{-1}\right]}{\mathbf{b}_{\mathcal{B}}^{\text{in}\dagger}\left[k_0\mathbf{L}+\sin(k_0\mathbf{L})\mathbf{\Pi}\right]\mathbf{b}_{\mathcal{B}}^{\text{in}}}\mathbf{U}(k_0)_{\mathcal{B}\mathcal{L}}. \tag{206}$$

For quantum graphs with vertex matching conditions leading to vertex scattering matrices not depending on the wave number, (such as Neumann- Kirchhoff boundary conditions), this simplifies further to

$$\mathbf{P}\boldsymbol{\rho}(k_0)=-\mathbf{P}\mathbf{L}\;\frac{\mathbb{I}+\mathbf{U}(k_0)_{\mathcal{B}\mathcal{B}}\mathbf{Y}_Q(k_0)^{-1}}{\mathbf{b}_{\mathcal{B}}^{\text{in}\dagger}\mathbf{L}\;\mathbf{b}_{\mathcal{B}}^{\text{in}}}\mathbf{U}(k_0)_{\mathcal{B}\mathcal{L}}\;. \tag{207}$$

Likewise, it can be shown that $\mathbf{Q}\boldsymbol{\rho}$ in (194) and the scattering matrix in (37) are also well defined in an interval containing k_0. In the limit $k\to k_0$, we obtain for the latter the result (99) as expected.

In this regularization, we have explicitly used equation (183) which is valid precisely for scattering matrices that come from a self-adjoint matching condition. So one may

wonder whether it is valid for the large amount of physical quantum graph models that define the quantum graph in terms of arbitrary prescribed scattering matrices (as for instance in [229]). In most of these physical cases, the scattering matrices are assumed to be constant with respect to k which implies that the right-hand side of equation (183) vanishes. It is easy to see that this leads to some simplifications in the following formulas and leads to a well-defined regularized scattering matrix. If one prescribes scattering matrices with some dependency on the wave number then the regularity of the scattering matrices in the presence of bound states cannot be guaranteed in general. However if the scattering matrix is an effective description derived from a more detailed self-adjoint system (whether that is a graph or a different type of model), then there exists a well-defined scattering matrix both physically and mathematically basically because the spectral decomposition of self-adjoint operators is always based on orthogonal projections, such that scattering states are always orthogonal to bound states. Showing the regularity in this case will require an analogous projection method but will generally require its own analysis. Vice versa a non-regular scattering matrix may be an indicator that a model is not physical in all respects (which does not necessarily mean that the model is bad as long as its limitations are known).

Our assumption that the perfect scar is non-degenerate may also be lifted but leads to more cumbersome calculations – if the perfect scars do not overlap, one may regularise by first regularizing the scattering matrices of the corresponding non-overlapping subgraphs and then build up the full scattering matrix from there. Otherwise the rank one projector $\mathbf{P}$ needs to be replaced by higher rank projectors.

Bibliography

[1] L. Solymar and E. Shamonina. *Waves in metamaterials*. Oxford University Press, 2009.

[2] R.S. Kshetrimayum. A brief intro to metamaterials. *IEEE Potentials*, 23(5):44–46, 2005.

[3] Rakesh Kumar, Manoj Kumar, Jasgurpreet Singh Chohan, and Santosh Kumar. Overview on metamaterial: History, types and applications. *Materials Today: Proceedings*, 56:3016–3024, 2022. 3rd International Conference on Contemporary Advances in Mechanical Engineering.

[4] V. G. Veselago. The electrodynamics of substances with simultaneously negative values of permittivity and permeability. *Soviet Physics Uspekhi*, 10(4):509–514, 1968.

[5] J. B. Pendry. Negative refraction makes a perfect lens. *Physical Review Letters*, 85(18):3966–3969, 2000.

[6] D. R. Smith, D. C. Vier, N. Kroll, and S. Schultz. Direct calculation of permeability and permittivity for a left-handed metamaterial. *Applied Physics Letters*, 77(14):2246–2248, 2000.

[7] David R Smith, John B Pendry, and Mike CK Wiltshire. Metamaterials and negative refractive index. *science*, 305(5685):788–792, 2004.

[8] Vladimir M Shalaev. Optical negative-index metamaterials. *Nature photonics*, 1(1):41–48, 2007.

[9] George V Eleftheriades and Omar F Siddiqui. Negative refraction and focusing in hyperbolic transmission-line periodic grids. *IEEE transactions on microwave theory and techniques*, 53(1):396–403, 2005.

[10] Xiang Zhang and Zheng Liu. Superlenses to overcome the diffraction limit. *Nature Materials*, 7:435–441, 2008.

[11] G.V. Eleftheriades, A.K. Iyer, and P.C. Kremer. Planar negative refractive index media using periodically l-c loaded transmission lines. *IEEE Transactions on Microwave Theory and Techniques*, 50(12):2702–2712, 2002.

[12] William Henry Bragg and William Lawrence Bragg. The reflection of x-rays by crystals. *Proceedings of the Royal Society of London. Series A, Containing Papers of a Mathematical and Physical Character*, 88(605):428–438, 1913.

[13] Philip Hofmann. *Solid state physics: an introduction*. John Wiley & Sons, 2015.

[14] Charles Kittel. *Introduction to solid state physics*. John Wiley & sons, inc, 2005.

[15] Ertugrul Cubukcu, Koray Aydin, Ekmel Ozbay, Stavroula Foteinopoulou, and Costas M Soukoulis. Negative refraction by photonic crystals. *Nature*, 423(6940):604–605, 2003.

[16] Mark S Wheeler, J Stewart Aitchison, and Mohammad Mojahedi. Negative refraction in a photonic crystal with a metallic cross lattice basis. *Physical Review B*, 71(15):155106, 2005.

[17] Dmitry N Chigrin, Stefan Enoch, Clivia M Sotomayor Torres, and Gérard Tayeb. Self-guiding in two-dimensional photonic crystals. *Optics express*, 11(10):1203–1211, 2003.

[18] Amir H Safavi-Naeini and Oskar Painter. Design of optomechanical cavities and waveguides on a simultaneous bandgap phononic-photonic crystal slab. *Optics express*, 18(14):14926–14943, 2010.

[19] Yan Pennec, B Djafari Rouhani, EH El Boudouti, C Li, Y El Hassouani, Jerome O Vasseur, Nikos Papanikolaou, Sarah Benchabane, Vincent Laude, and Alejandro Martinez. Simultaneous existence of phononic and photonic band gaps in periodic crystal slabs. *Optics express*, 18(13):14301–14310, 2010.

[20] Ranjan Singh, Wei Cao, Ibraheem Al-Naib, Longqing Cong, Withawat Withayachumnankul, and Weili Zhang. Ultrasensitive terahertz sensing with high-q fano resonances in metasurfaces. *Applied Physics Letters*, 105(17), 2014.

[21] Ertugrul Basar, Marco Di Renzo, Julien De Rosny, Merouane Debbah, Mohamed-Slim Alouini, and Rui Zhang. Wireless communications through reconfigurable intelligent surfaces. *IEEE access*, 7:116753–116773, 2019.

[22] Hou-Tong Chen, Willie J Padilla, Joshua MO Zide, Arthur C Gossard, Antoinette J Taylor, and Richard D Averitt. Active terahertz metamaterial devices. *Nature*, 444(7119):597–600, 2006.

[23] Wai Lam Chan, Jason Deibel, and Daniel M Mittleman. Imaging with terahertz radiation. *Reports on progress in physics*, 70(8):1325, 2007.

[24] Tadao Nagatsuma, Guillaume Ducournau, and Cyril C Renaud. Advances in terahertz communications accelerated by photonics. *Nature Photonics*, 10(6):371–379, 2016.

[25] Emanuel Colella, Luca Bastianelli, Mohsen Khalily, Franco Moglie, Zhen Peng, and Gabriele Gradoni. Quantum optimisation of reconfigurable surfaces in complex propagation environments. In *2024 18th European Conference on Antennas and Propagation (EuCAP)*, pages 1–5. IEEE, 2024.

[26] Emilio Calvanese Strinati, George C Alexandropoulos, Vincenzo Sciancalepore, Marco Di Renzo, Henk Wymeersch, Dinh-Thuy Phan-Huy, Maurizio Crozzoli, Raffaele d'Errico, Elisabeth De Carvalho, Petar Popovski, et al.

Wireless environment as a service enabled by reconfigurable intelligent surfaces: The rise-6g perspective. In *2021 Joint European Conference on Networks and Communications & 6G Summit (EuCNC/6G Summit)*, pages 562–567. IEEE, 2021.

[27] Wenshan Cai, Uday K Chettiar, Alexander V Kildishev, and Vladimir M Shalaev. Optical cloaking with metamaterials. *Nature photonics*, 1(4):224–227, 2007.

[28] Ulf Leonhardt. Optical conformal mapping. *science*, 312(5781):1777–1780, 2006.

[29] Jensen Li and John B Pendry. Hiding under the carpet: a new strategy for cloaking. *Physical review letters*, 101(20):203901, 2008.

[30] John B Pendry, David Schurig, and David R Smith. Controlling electromagnetic fields. *science*, 312(5781):1780–1782, 2006.

[31] Jun Xu, Xu Jiang, Nicholas Fang, Elodie Georget, Redha Abdeddaim, Jean-Michel Geffrin, Mohamed Farhat, Pierre Sabouroux, Stefan Enoch, and Sébastien Guenneau. Molding acoustic, electromagnetic and water waves with a single cloak. *Scientific reports*, 5(1):10678, 2015.

[32] Yihao Yang, Huaping Wang, Faxin Yu, Zhiwei Xu, and Hongsheng Chen. A metasurface carpet cloak for electromagnetic, acoustic and water waves. *Scientific reports*, 6(1):1–6, 2016.

[33] Badreddine Assouar, Bin Liang, Ying Wu, Yong Li, Jian-Chun Cheng, and Yun Jing. Acoustic metasurfaces. *Nature Reviews Materials*, 3(12):460–472, 2018.

[34] Steven A Cummer, Johan Christensen, and Andrea Alù. Controlling sound with acoustic metamaterials. *Nature Reviews Materials*, 1(3):1–13, 2016.

[35] Stéphane Brûlé, EH Javelaud, Stefan Enoch, and Sébastien Guenneau. Experiments on seismic metamaterials: molding surface waves. *Physical review letters*, 112(13):133901, 2014.

[36] Thomas Vasileiadis, Jeena Varghese, Visnja Babacic, Jordi Gomis-Bresco, Daniel Navarro Urrios, and Bartlomiej Graczykowski. Progress and perspectives on phononic crystals. *Journal of Applied Physics*, 129(16):160901, 2021.

[37] Gianni Campoli, MS Borleffs, S Amin Yavari, R Wauthle, Harrie Weinans, and Amir Abbas Zadpoor. Mechanical properties of open-cell metallic biomaterials manufactured using additive manufacturing. *Materials & Design*, 49:957–965, 2013.

[38] Leo-Paul Euvé, Kim Pham, and Agnès Maurel. Negative refraction of water waves by hyperbolic metamaterials. *Journal of Fluid Mechanics*, 961:A16, 2023.

[39] Alexander L Rakhmanov, Alexandre M Zagoskin, Sergey Savel'ev, and Franco Nori. Quantum metamaterials: Electromagnetic waves in a josephson qubit line. *Physical Review B*, 77(14):144507, 2008.

[40] Manvir S Kushwaha, Peter Halevi, Leonard Dobrzynski, and Bahram Djafari-Rouhani. Acoustic band structure of periodic elastic composites. *Physical review letters*, 71(13):2022, 1993.

[41] Olivia McGee, Huan Jiang, Feng Qian, Zian Jia, Lifeng Wang, Han Meng, Dimitrios Chronopoulos, Yanyu Chen, and Lei Zuo. 3d printed architected hollow sphere foams with low-frequency phononic band gaps. *Additive Manufacturing*, 30:100842, 2019.

[42] Huan Jiang and Yanyu Chen. Lightweight architected hollow sphere foams for simultaneous noise and vibration control. *Journal of Physics D: Applied Physics*, 52(32):325303, 2019.

[43] C Sugino, M Ruzzene, and A Erturk. Merging mechanical and electromechanical bandgaps in locally resonant metamaterials and metastructures. *Journal of the Mechanics and Physics of Solids*, 116:323–333, 2018.

[44] Christophe Droz, Olivier Robin, Mohamed Ichchou, and Noureddine Atalla. Improving sound transmission loss at ring frequency of a curved panel using tunable 3d-printed small-scale resonators. *The Journal of the Acoustical Society of America*, 145(1):EL72–EL78, 2019.

[45] Alice L Vanel, Richard V Craster, and Ory Schnitzer. Asymptotic modeling of phononic box crystals. *SIAM Journal on Applied Mathematics*, 79(2):506–524, 2019.

[46] Weimin Kuang, Zhilin Hou, Youyan Liu, and Hai Li. The band gaps of cubic phononic crystals with different shapes of scatterers. *Journal of Physics D: Applied Physics*, 39:2076–2071, 2006.

[47] Osama R Bilal and Mahmoud I Hussein. Trampoline metamaterial: Local resonance enhancement by springboards. *Applied Physics Letters*, 103(11):111901, 2013.

[48] Osama R Bilal, David Ballagi, and Chiara Daraio. Architected lattices for simultaneous broadband attenuation of airborne sound and mechanical vibrations in all directions. *Physical Review Applied*, 10(5):054060, 2018.

[49] Waiel Elmadih, Dimitrios Chronopoulos, and Jian Zhu. Metamaterials for simultaneous acoustic and elastic bandgaps. *Scientific reports*, 11(1):14635, 2021.

[50] Krupali Donda, Yifan Zhu, Shi-Wang Fan, Liyun Cao, Yong Li, and Badreddine Assouar. Extreme low-frequency ultrathin acoustic absorbing metasurface. *Applied Physics Letters*, 115(17), 2019.

[51] Jinliang Song, Dawei Hu, Shengmin Luo, Wanshu Liu, Dongfang Wang, Quansheng Sun, and Guoping Zhang. Energy-absorption behavior of metallic hollow sphere structures under impact loading. *Engineering Structures*, 226:111350, 2021.

[52] Ying Liu, He-xiang Wu, Xin-chun Zhang, and B Wang. The influence of lattice structure on the dynamic performance of metal hollow sphere agglomerates. *Mechanics Research Communications*, 38(8):569–573, 2011.

[53] HB Zeng, Stephane Pattofatto, Han Zhao, Yannick Girard, and Valia Fascio. Impact behaviour of hollow sphere agglomerates with density gradient. *International journal of mechanical sciences*, 52(5):680–688, 2010.

[54] R Winkler, M Merkel, A Öchsner, and W Günter. On the vibration analysis of adhesively bonded hollow sphere structures. *Materialwissenschaft und Werkstofftechnik: Entwicklung, Fertigung, Prüfung, Eigenschaften und Anwendungen technischer Werkstoffe*, 39(2):139–142, 2008.

[55] Nikos Aravantinos-Zafiris, Nikos Kanistras, and Mihail M Sigalas. Acoustoelastic phononic metamaterial for isolation of sound and vibrations. *Journal of Applied Physics*, 129(10), 2021.

[56] Suxia Yang, John H Page, Zhengyou Liu, Michael L Cowan, Che Ting Chan, and Ping Sheng. Focusing of sound in a 3d phononic crystal. *Physical review letters*, 93(2):024301, 2004.

[57] J Bucay, E Roussel, Jerome O Vasseur, Pierre A Deymier, AC Hladky-Hennion, Yan Pennec, Krishna Muralidharan, Bahram Djafari-Rouhani, and Bertrand Dubus. Positive, negative, zero refraction, and beam splitting in a solid/air phononic crystal: Theoretical and experimental study. *Physical Review B*, 79(21):214305, 2009.

[58] Ahmet Cicek, Olgun Adem Kaya, and Bulent Ulug. Wide-band all-angle acoustic self-collimation by rectangular sonic crystals with elliptical bases. *Journal of Physics D: Applied Physics*, 44(20):205104, 2011.

[59] Johan Christensen, Antonio I Fernandez-Dominguez, Fernando de Leon-Perez, Luis Martin-Moreno, and FJ Garcia-Vidal. Collimation of sound assisted by acoustic surface waves. *Nature Physics*, 3(12):851–852, 2007.

[60] N Swinteck, J-F Robillard, S Bringuier, J Bucay, K Muralidharan, Jerome O Vasseur, K Runge, and PA Deymier. Phase-controlling phononic crystal. *Applied Physics Letters*, 98(10), 2011.

[61] Manzhu Ke, Zhengyou Liu, Chunyin Qiu, Wengang Wang, Jing Shi, Weijia Wen, and Ping Sheng. Negative-refraction imaging with two-dimensional phononic crystals. *Physical Review B*, 72(6):064306, 2005.

[62] A Sukhovich, B Merheb, Krishna Muralidharan, Jérôme Olivier Vasseur, Yan Pennec, Pierre A Deymier, and JH Page. Experimental and theoretical evidence for subwavelength imaging in phononic crystals. *Physical review letters*, 102(15):154301, 2009.

[63] Jensen Li, Lee Fok, Xiaobo Yin, Guy Bartal, and Xiang Zhang. Experimental demonstration of an acoustic magnifying hyperlens. *Nature materials*, 8(12):931–934, 2009.

[64] Ezekiel L Walker, Yuqi Jin, Delfino Reyes, and Arup Neogi. Sub-wavelength lateral detection of tissue-approximating masses using an ultrasonic metamaterial lens. *Nature Communications*, 11(1):5967, 2020.

[65] HH Huang, CT Sun, and GL Huang. On the negative effective mass density in acoustic metamaterials. *International Journal of Engineering Science*, 47(4):610–617, 2009.

[66] H Nassar, H Chen, AN Norris, MR Haberman, and GL Huang. Non-reciprocal wave propagation in modulated elastic metamaterials. *Proceedings of the Royal Society A: Mathematical, Physical and Engineering Sciences*, 473(2202):20170188, 2017.

[67] Muhammad and C W Lim. From photonic crystals to seismic metamaterials: A review via phononic crystals and acoustic metamaterials. *Archives of Computational Methods in Engineering*, pages 1–62, 2021.

[68] Stéphane Brûlé, Stefan Enoch, and Sébastien Guenneau. Emergence of seismic metamaterials: Current state and future perspectives. *Physics Letters A*, 384(1):126034, 2020.

[69] Ivan I Argatov and Federico J Sabina. Transient scattering of a rayleigh wave by a cluster of subwavelength resonators—towards asymptotic modeling of seismic surface metabarriers. *International Journal of Engineering Science*, 194:103963, 2024.

[70] Marco Miniaci, Anastasiia Krushynska, Federico Bosia, and Nicola M Pugno. Large scale mechanical metamaterials as seismic shields. *New Journal of Physics*, 18(8):083041, 2016.

[71] Daniel J Colquitt, Ian S Jones, Natalia V Movchan, Alexander B Movchan, and Ross C McPhedran. Dynamic anisotropy and localization in elastic lattice systems. *Waves in Random and Complex Media*, 22(2):143–159, 2012.

[72] KH Madine and DJ Colquitt. Negative refraction and mode trapping of flexural–torsional waves in elastic lattices. *Philosophical Transactions of the Royal Society A*, 380(2237):20210379, 2022.

[73] Shahab Amanat, Reza Rafiee-Dehkharghani, Maryam Bitaraf, and Dipanshu Bansal. Analytical and numerical investigation of finite and infinite periodic

lattices for mitigation of seismic waves in layered grounds. *International Journal of Engineering Science*, 173:103655, 2022.

[74] Steven A Cummer and David Schurig. One path to acoustic cloaking. *New journal of physics*, 9(3):45, 2007.

[75] Shu Zhang, Chunguang Xia, and Nicholas Fang. Broadband acoustic cloak for ultrasound waves. *Physical review letters*, 106(2):024301, 2011.

[76] M Garau, MJ Nieves, G Carta, and M Brun. Transient response of a gyro-elastic structured medium: unidirectional waveforms and cloaking. *International Journal of Engineering Science*, 143:115–141, 2019.

[77] Nicolas Stenger, Manfred Wilhelm, and Martin Wegener. Experiments on elastic cloaking in thin plates. *Physical review letters*, 108(1):014301, 2012.

[78] Lucian Zigoneanu, Bogdan-Ioan Popa, and Steven A Cummer. Three-dimensional broadband omnidirectional acoustic ground cloak. *Nature materials*, 13(4):352–355, 2014.

[79] Andrew N Norris, Feruza A Amirkulova, and William J Parnell. Active elastodynamic cloaking. *Mathematics and Mechanics of Solids*, 19(6):603–625, 2014.

[80] Victor Manuel García-Chocano, Lorenzo Sanchis, Ana Díaz-Rubio, J Martínez-Pastor, Francisco Cervera, Rafael Llopis-Pontiveros, and Jose Sánchez-Dehesa. Acoustic cloak for airborne sound by inverse design. *Applied physics letters*, 99(7), 2011.

[81] Jian Zhu, Tianning Chen, Xinpei Song, Chen Chen, Zhiqiang Liu, and Junzhe Zhang. Three-dimensional large-scale acoustic invisibility cloak with layered metamaterials for underwater operation. *Physica Scripta*, 94(11):115003, 2019.

[82] Joseph N Grima, Szymon Winczewski, Luke Mizzi, Michael C Grech, Reuben Cauchi, Ruben Gatt, Daphne Attard, Krzysztof W Wojciechowski, Jarosław Rybicki, et al. Tailoring graphene to achieve negative poisson's ratio properties. *Adv. Mater*, 27(8):1455–1459, 2015.

[83] Fernando Fraternali, Gerardo Carpentieri, and Ada Amendola. On the mechanical modeling of the extreme softening/stiffening response of axially loaded tensegrity prisms. *Journal of the Mechanics and Physics of Solids*, 74:136–157, 2015.

[84] Jeffrey Ian Lipton, Robert MacCurdy, Zachary Manchester, Lillian Chin, Daniel Cellucci, and Daniela Rus. Handedness in shearing auxetics creates rigid and compliant structures. *Science*, 360(6389):632–635, 2018.

[85] Katia Bertoldi, Vincenzo Vitelli, Johan Christensen, and Martin Van Hecke. Flexible mechanical metamaterials. *Nature Reviews Materials*, 2(11):1–11, 2017.

[86] ST Szyniszewski, BH Smith, JF Hajjar, BW Schafer, and SR Arwade. The mechanical properties and modeling of a sintered hollow sphere steel foam. *Materials & Design (1980-2015)*, 54:1083–1094, 2014.

[87] Chuanqi Yang, Kuijian Yang, Yunpeng Tian, Minghui Fu, and Lingling Hu. Theoretical analysis on the stiffness of compression–torsion coupling metamaterials. *Extreme Mechanics Letters*, 46:101336, 2021.

[88] Tobias Frenzel, Muamer Kadic, and Martin Wegener. Three-dimensional mechanical metamaterials with a twist. *Science*, 358(6366):1072–1074, 2017.

[89] Wynn S Sanders and LJ Gibson. Mechanics of hollow sphere foams. *Materials Science and Engineering: A*, 347(1-2):70–85, 2003.

[90] T-J Lim, B Smith, and DL McDowell. Behavior of a random hollow sphere metal foam. *Acta Materialia*, 50(11):2867–2879, 2002.

[91] Adam Anglart. *Experimental study and modeling of metamaterials for water surface waves*. PhD thesis, Université Paris sciences et lettres, 2021.

[92] Agnès Maurel, Kim Pham, and Jean-Jacques Marigo. Scattering of gravity waves by a periodically structured ridge of finite extent. *Journal of Fluid Mechanics*, 871:350–376, 2019.

[93] Mohamed Farhat, Sebastien Guenneau, Stefan Enoch, and Alexander Movchan. All-angle-negative-refraction and ultra-refraction for liquid surface waves in 2d phononic crystals. *Journal of computational and applied mathematics*, 234(6):2011–2019, 2010.

[94] Ben Wilks, Fabien Montiel, and Sarah Wakes. Rainbow reflection and broadband energy absorption of water waves by graded arrays of vertical barriers. *Journal of Fluid Mechanics*, 941:A26, 2022.

[95] Benjamin Carter. *Water-wave propagation through very large floating structures*. PhD thesis, Loughborough University, 2012.

[96] Chiang C Mei. Resonant reflection of surface water waves by periodic sandbars. *Journal of Fluid Mechanics*, 152:315–335, 1985.

[97] Robert Schittny, Muamer Kadic, Sebastien Guenneau, and Martin Wegener. Experiments on transformation thermodynamics: molding the flow of heat. *Physical review letters*, 110(19):195901, 2013.

[98] Mauro Bracconi, Matteo Ambrosetti, Matteo Maestri, Gianpiero Groppi, and Enrico Tronconi. A fundamental analysis of the influence of the geometrical properties on the effective thermal conductivity of open-cell foams. *Chemical Engineering and Processing-Process Intensification*, 129:181–189, 2018.

[99] Zian Jia, Zhen Wang, David Hwang, and Lifeng Wang. Prediction of the effective thermal conductivity of hollow sphere foams. *ACS Applied Energy Materials*, 1(3):1146–1157, 2018.

[100] Muhammad Raza, Yichao Liu, El Hang Lee, and Yungui Ma. Transformation thermodynamics and heat cloaking: a review. *Journal of Optics*, 18(4):044002, 2016.

[101] Ying Li, Wei Li, Tiancheng Han, Xu Zheng, Jiaxin Li, Baowen Li, Shanhui Fan, and Cheng-Wei Qiu. Transforming heat transfer with thermal metamaterials and devices. *Nature Reviews Materials*, 6(6):488–507, 2021.

[102] Jae Choon Kim, Zongqing Ren, Anil Yuksel, Ercan M Dede, Prabhakar R Bandaru, Dan Oh, and Jaeho Lee. Recent advances in thermal metamaterials and their future applications for electronics packaging. *Journal of Electronic Packaging*, 143(1):010801, 2021.

[103] Tiancheng Han, Xue Bai, John TL Thong, Baowen Li, and Cheng-Wei Qiu. Full control and manipulation of heat signatures: cloaking, camouflage and thermal metamaterials. *Adv. Mater*, 26(11):1731–1734, 2014.

[104] Ercan M Dede, Tsuyoshi Nomura, and Jaewook Lee. Thermal-composite design optimization for heat flux shielding, focusing, and reversal. *Structural and Multidisciplinary Optimization*, 49:59–68, 2014.

[105] Stanislav B Glybovski, Sergei A Tretyakov, Pavel A Belov, Yuri S Kivshar, and Constantin R Simovski. Metasurfaces: From microwaves to visible. *Physics reports*, 634:1–72, 2016.

[106] Nanfang Yu, Patrice Genevet, Mikhail A Kats, Francesco Aieta, Jean-Philippe Tetienne, Federico Capasso, and Zeno Gaburro. Light propagation with phase discontinuities: generalized laws of reflection and refraction. *science*, 334(6054):333–337, 2011.

[107] Ben A Munk. *Frequency selective surfaces: theory and design*. John Wiley & Sons, 2005.

[108] Rong-Rong Xu, Zhi-Yuan Zong, and Wen Wu. Low-frequency miniaturized dual-band frequency selective surfaces with close band spacing. *Microwave and Optical Technology Letters*, 51(5):1238–1240, 2009.

[109] Xiao-Dong Hu, Xi-Lang Zhou, Lin-Sheng Wu, Liang Zhou, and Wen-Yan Yin. A miniaturized dual-band frequency selective surface (fss) with closed loop and its complementary pattern. *IEEE Antennas and Wireless Propagation Letters*, 8:1374–1377, 2009.

[110] MA Hiranandani, AB Yakovlev, and AA Kishk. Artificial magnetic conductors realised by frequency-selective surfaces on a grounded dielectric slab for antenna applications. *IEE Proceedings-Microwaves, antennas and propagation*, 153(5):487–493, 2006.

[111] Younes Ra'di, Constantin R Simovski, and Sergei A Tretyakov. Thin perfect absorbers for electromagnetic waves: theory, design, and realizations. *Physical Review Applied*, 3(3):037001, 2015.

[112] Yongzhi Cheng, Helin Yang, Zhengze Cheng, and Boxun Xiao. A planar polarization-insensitive metamaterial absorber. *Photonics and Nanostructures-Fundamentals and Applications*, 9(1):8–14, 2011.

[113] Jin-Yuan Xue, Shu-Xi Gong, Peng-Fei Zhang, Wei Wang, and Fei-Fei Zhang. A new miniaturized fractal frequency selective surface with excellent angular stability. *Progress In Electromagnetics Research Letters*, 13:131–138, 2010.

[114] Lei Lu, Shaobo Qu, Hua Ma, Fei Yu, Song Xia, Zhuo Xu, and Peng Bai. A polarization-independent wide-angle dual directional absorption metamaterial absorber. *Progress In Electromagnetics Research M*, 27:91–201, 2012.

[115] Filippo Costa, Simone Genovesi, and Agostino Monorchio. On the bandwidth of high-impedance frequency selective surfaces. *IEEE Antennas and Wireless Propagation Letters*, 8:1341–1344, 2009.

[116] Douglas J Kern, Douglas H Werner, Agostino Monorchio, Luigi Lanuzza, and Michael J Wilhelm. The design synthesis of multiband artificial magnetic conductors using high impedance frequency selective surfaces. *IEEE Transactions on antennas and propagation*, 53(1):8–17, 2005.

[117] Xingjie Ni, Alexander V Kildishev, and Vladimir M Shalaev. Metasurface holograms for visible light. *Nature communications*, 4(1):2807, 2013.

[118] Hou-Tong Chen, Antoinette J Taylor, and Nanfang Yu. A review of metasurfaces: physics and applications. *Reports on progress in physics*, 79(7):076401, 2016.

[119] Xiaofang Yu and Shanhui Fan. Anomalous reflections at photonic crystal surfaces. *Physical Review E*, 70(5):055601, 2004.

[120] TJ Davis, Fatima Eftekhari, DE Gómez, and Ann Roberts. Metasurfaces with asymmetric optical transfer functions for optical signal processing. *Physical review letters*, 123(1):013901, 2019.

[121] Alexander V Kildishev, Alexandra Boltasseva, and Vladimir M Shalaev. Planar photonics with metasurfaces. *Science*, 339(6125):1232009, 2013.

[122] Yang Zhao, Xing-Xiang Liu, and Andrea Alù. Recent advances on optical metasurfaces. *Journal of Optics*, 16(12):123001, 2014.

[123] Vin-Cent Su, Cheng Hung Chu, Greg Sun, and Din Ping Tsai. Advances in optical metasurfaces: fabrication and applications. *Optics express*, 26(10):13148–13182, 2018.

[124] Lei Zhang, Shengtao Mei, Kun Huang, and Cheng-Wei Qiu. Advances in full control of electromagnetic waves with metasurfaces. *Advanced Optical Materials*, 4(6):818–833, 2016.

[125] Alexandre Silva, Francesco Monticone, Giuseppe Castaldi, Vincenzo Galdi, Andrea Alù, and Nader Engheta. Performing mathematical operations with metamaterials. *Science*, 343(6167):160–163, 2014.

[126] Dmitry A. Bykov, Leonid L. Doskolovich, Evgeni A. Bezus, and Victor A. Soifer. Optical computation of the laplace operator using phase-shifted bragg grating. *Opt. Express*, 22(21):25084–25092, Oct 2014.

[127] Han Meng, Waiel Elmadih, Huan Jiang, Tristan Lawrie, Yanyu Chen, and Dimitrios Chronopoulos. Broadband vibration attenuation achieved by additively manufactured 3d rainbow hollow sphere foams. *Applied Physics Letters*, 119(18), 2021.

[128] Zhenhuan Tian, J Bennett, J Yang, T Lawrie, W Elmadih, A Bardalai, C Gerada, Jian Zhu, and D Chronopoulos. Experimental investigation of mechanical, acoustic and hybrid metamaterial designs for enhanced and multi-band electric motor noise dissipation. *Engineering Structures*, 271:114945, 2022.

[129] A Srikantha Phani and Mahmoud I Hussein. *Dynamics of Lattice Materials*. Wiley Online Library, 2017.

[130] Richard V Craster, Julius Kaplunov, and Aleksey V Pichugin. High-frequency homogenization for periodic media. *Proceedings of the Royal Society A: Mathematical, Physical and Engineering Sciences*, 466(2120):2341–2362, 2010.

[131] Daniel Leykam, Alexei Andreanov, and Sergej Flach. Artificial flat band systems: from lattice models to experiments. *Advances in Physics: X*, 3(1):1473052, 2018.

[132] Ke Wang, Yi Chen, Muamer Kadic, Changguo Wang, and Martin Wegener. Nonlocal interaction engineering of 2d roton-like dispersion relations in acoustic and mechanical metamaterials. *Communications Materials*, 3(1):35, 2022.

[133] Julio Andrés Iglesias Martínez, Michael Fidelis Groß, Yi Chen, Tobias Frenzel, Vincent Laude, Muamer Kadic, and Martin Wegener. Experimental observation of roton-like dispersion relations in metamaterials. *Science advances*, 7(49):eabm2189, 2021.

[134] Esmaeal Ghavanloo and S Ahmad Fazelzadeh. Wave propagation in one-dimensional infinite acoustic metamaterials with long-range interactions. *Acta Mechanica*, 230(12):4453–4461, 2019.

[135] GJ Chaplain, IR Hooper, AP Hibbins, and TA Starkey. Reconfigurable elastic metamaterials: Engineering dispersion with beyond nearest neighbors. *Physical Review Applied*, 19(4):044061, 2023.

[136] Yi Chen, Jonathan LG Schneider, Michael F Groß, Ke Wang, Sebastian Kalt, Philip Scott, Muamer Kadic, and Martin Wegener. Observation of chirality-induced roton-like dispersion in a 3d micropolar elastic metamaterial. *Advanced Functional Materials*, page 2302699, 2023.

[137] Arash Kazemi, Kshiteej J Deshmukh, Fei Chen, Yunya Liu, Bolei Deng, Henry Chien Fu, and Pai Wang. Non-local phononic crystals for dispersion customization and undulation-point dynamics. *arXiv preprint arXiv:2302.00591*, 2023.

[138] Vikram S Deshpande, Norman A Fleck, and Michael F Ashby. Effective properties of the octet-truss lattice material. *Journal of the Mechanics and Physics of Solids*, 49(8):1747–1769, 2001.

[139] A Srikantha Phani, J Woodhouse, and NA Fleck. Wave propagation in two-

dimensional periodic lattices. *The Journal of the Acoustical Society of America*, 119(4):1995–2005, 2006.

[140] R de L Kronig and William George Penney. Quantum mechanics of electrons in crystal lattices. *Proceedings of the royal society of London. series A, containing papers of a mathematical and physical character*, 130(814):499–513, 1931.

[141] Pavel Exner. Lattice kronig-penney models. *Physical review letters*, 74(18):3503, 1995.

[142] John M Ziman. *Electrons and phonons: the theory of transport phenomena in solids*. Oxford university press, 2001.

[143] Graeme W Milton. New metamaterials with macroscopic behavior outside that of continuum elastodynamics. *New Journal of Physics*, 9(10):359, 2007.

[144] MJ Nieves and BL Sharma. Interaction of in-plane waves with a structured penetrable line defect in an elastic lattice. *International Journal of Engineering Science*, 197:104011, 2024.

[145] Wenming Wei, Shuwei Ren, Dimitrios Chronopoulos, and Han Meng. Optimization of connection architectures and mass distributions for metamaterials with multiple resonators. *Journal of Applied Physics*, 129(16):165101, 2021.

[146] David M Pozar. *Microwave engineering: theory and techniques*. John wiley & sons, 2021.

[147] Christophe Caloz and Tatsuo Itoh. Application of the transmission line theory of left-handed (lh) materials to the realization of a microstrip" lh line". In *IEEE Antennas and Propagation Society International Symposium (IEEE Cat. No. 02CH37313)*, volume 2, pages 412–415. IEEE, 2002.

[148] Pekka Alitalo, Stanislav Maslovski, and Sergei Tretyakov. Three-dimensional

isotropic perfect lens based on lc-loaded transmission lines. *Journal of Applied Physics*, 99(6), 2006.

[149] Junuthula Narasimha Reddy. An introduction to the finite element method. *New York*, 27:14, 1993.

[150] Jichun Li and Yunqing Huang. *Time-domain finite element methods for Maxwell's equations in metamaterials*, volume 43. Springer Science & Business Media, 2012.

[151] Linus Pauling. The diamagnetic anisotropy of aromatic molecules. *The Journal of chemical physics*, 4(10):673–677, 1936.

[152] Klaus Ruedenberg and Charles W Scherr. Free-electron network model for conjugated systems. i. theory. *The Journal of Chemical Physics*, 21(9):1565–1581, 1953.

[153] CA Coulson. Note on the applicability of the free-electron network model to metals. *Proceedings of the Physical Society. Section A*, 67(7):608, 1954.

[154] Elliott W Montroll. Quantum theory on a network. i. a solvable model whose wavefunctions are elementary functions. *Journal of Mathematical Physics*, 11(2):635–648, 1970.

[155] J.-P. Roth. Spectre du laplacien sur un graphe. *Comptes rendus de l'Académie des sciences Paris*, 296:793, 1983.

[156] S Alexander. Superconductivity of networks. a percolation approach to the effects of disorder. *Physical Review B*, 27(3):1541, 1983.

[157] Joachim von Below. Sturm-liouville eigenvalue problems on networks. *Mathematical Methods in the Applied Sciences*, 10(4):383–395, 1988.

[158] Serge Nicaise. Some results on spectral theory over networks, applied to nerve impulse transmission. In *Polynômes Orthogonaux et Applications: Proceedings of the Laguerre Symposium held at Bar-le-Duc, October 15–18, 1984*, pages 532–541. Springer, 1985.

[159] Gregory Berkolaiko and Peter Kuchment. *Introduction to Quantum Graphs*, volume 186 of *Mathematical Surveys and Monographs*. American Mathematical Society, 2013.

[160] Peter Kuchment and Hongbiao Zeng. Convergence of spectra of mesoscopic systems collapsing onto a graph. *Journal of Mathematical Analysis and Applications*, 258(2):671–700, 2001.

[161] Jacob Rubinstein and Michelle Schatzman. Variational problems on multiply connected thin strips i: Basic estimates and convergence of the laplacian spectrum. *Archive for Rational Mechanics and Analysis*, 160:271–308, 2001.

[162] Pavel Exner and Olaf Post. Convergence of spectra of graph-like thin manifolds. *Journal of Geometry and Physics*, 54(1):77–115, 2005.

[163] Kirill D Cherednichenko, Yulia Yu Ershova, and Alexander V Kiselev. Norm-resolvent convergence for neumann laplacians on manifold thinning to graphs. *Mathematics*, 12(8):1161, 2024.

[164] Vadim Kostrykin and Robert Schrader. Kirchhoff's rule for quantum wires. *Journal of Physics A: Mathematical and General*, 32(4):595, 1999.

[165] JM Harrison, Uzy Smilansky, and B Winn. Quantum graphs where back-scattering is prohibited. *Journal of Physics A: Mathematical and Theoretical*, 40(47):14181, 2007.

[166] Taksu Cheon. Reflectionless and equiscattering quantum graphs. *Proc. ICQNM*, pages 18–22, 2011.

[167] Ram Band, Holger Schanz, and Gilad Sofer. Differences between robin and neumann eigenvalues on metric graphs. In *Annales Henri Poincaré*, pages 1–40. Springer, 2023.

[168] G. Tanner. Unitary-stochastic matrix ensembles and spectral statistics. *Journal of Physics A: Mathematical and General*, 34(41):8485–8500, 2001.

[169] Tsampikos Kottos and Uzy Smilansky. Periodic orbit theory and spectral statistics for quantum graphs. *Annals of Physics*, 274(1):76–124, 1999.

[170] Pavel Kurasov and Marlena Nowaczyk. Geometric properties of quantum graphs and vertex scattering matrices. *Opuscula Math.*, 30(3):295–309, 2010.

[171] Uzy Smilansky and Gilad Sofer. Time evolution and the schrödinger equation on time dependent quantum graphs. *Journal of Physics A: Mathematical and Theoretical*, 57(6):065204, 2024.

[172] G. Berkolaiko and P. Kuchment. *Introduction to Quantum Graphs*, volume 186 of *Mathematical Surveys and Monographs*. American Mathematical Society, Providence, Rhode Island, 2013.

[173] Samuel DM Adams, Richard V Craster, and Sebastien Guenneau. Bloch waves in periodic multi-layered acoustic waveguides. *Proceedings of the Royal Society A: Mathematical, Physical and Engineering Sciences*, 464(2098):2669–2692, 2008.

[174] RV Craster, LM Joseph, and J Kaplunov. Long-wave asymptotic theories: the connection between functionally graded waveguides and periodic media. *Wave Motion*, 51(4):581–588, 2014.

[175] Jian-Bai Xia. Quantum waveguide theory for mesoscopic structures. *Physical Review B*, 45(7):3593, 1992.

[176] Pavel Exner and Hynek Kovarík. Magnetic strip waveguides. *Journal of Physics A: Mathematical and General*, 33(16):3297, 2000.

[177] Mubarack Ahmed, Gabriele Gradoni, Stephen Creagh, Chris Smartt, Steve Greedy, and Gregor Tanner. Transport of power through networks of cables using quantum graph theory. In *2019 International Symposium on Electromagnetic Compatibility - EMC EUROPE*, pages 820–824, 2019.

[178] S Molchanov and B Vainberg. Slowing down of the wave packets in quantum graphs. *Waves in Random and Complex Media*, 15(1):101–112, 2005.

[179] Boris Pavlov. Resonance quantum switch: matching domains. In *Surveys in analysis and operator theory*, volume 40, pages 127–157. Australian National University, Mathematical Sciences Institute, 2002.

[180] Boris Pavlov and Kieran Robert. Resonance optical switch: calculation of resonance eigenvalues. *Contemporary Mathematics*, 339:141–170, 2003.

[181] A. Drinko, F. M. Andrade, and D. Bazeia. Narrow peaks of full transmission in simple quantum graphs. *Physical Review Letters A*, 100:062117, Dec 2019.

[182] A. Drinko, F. M. Andrade, and D. Bazeia. Simple quantum graphs proposal for quantum devices. *The European Physical Journal Plus*, 135(6):451, 2020.

[183] Taksu Cheon. Reflectionless and equiscattering quantum graphs and their applications. *International Journal on Advances in Systems and Measurements Volume 5, Number 1 & 2, 2012*, 2012.

[184] Johannes Nokkala, Jyrki Piilo, and Ginestra Bianconi. Complex quantum networks: a topical review. *Journal of Physics A: Mathematical and Theoretical*, 2024.

[185] Vadim Kostrykin and Robert Schrader. Kirchhoff's rule for quantum wires.

ii: The inverse problem with possible applications to quantum computers. *Fortschritte der Physik: Progress of Physics*, 48(8):703–716, 2000.

[186] Xiyue Sissi Wang, Romolo Savo, Andreas Maeder, Fabian Kaufmann, Jost Kellner, Andrea Morandi, Stefan Rotter, Riccardo Sapienza, and Rachel Grange. Graph model for multiple scattering in lithium niobate on insulator integrated photonic networks. *Optics Express*, 31(25):42255–42270, 2023.

[187] Dhruv Saxena, Alexis Arnaudon, Oscar Cipolato, Michele Gaio, Alain Quentel, Sophia Yaliraki, Dario Pisignano, Andrea Camposeo, Mauricio Barahona, and Riccardo Sapienza. Sensitivity and spectral control of network lasers. *Nature Communications*, 13(1):6493, 2022.

[188] Michele Gaio, Dhruv Saxena, Jacopo Bertolotti, Dario Pisignano, Andrea Camposeo, and Riccardo Sapienza. A nanophotonic laser on a graph. *Nature communications*, 10(1):226, 2019.

[189] S Alexander. Superconductivity of networks. a percolation approach to the effects of disorder. *Physical Review B*, 27(3):1541, 1983.

[190] Jacob Rubinstein and Michelle Schatzman. Asymptotics for thin superconducting rings. *Journal de mathématiques pures et appliquées*, 77(8):801–820, 1998.

[191] Michael Aizenman, Robert Sims, and Simone Warzel. Fluctuation-based proof of the stability of ac spectra of. In *Quantum Graphs and Their Applications: Proceedings of an AMS-IMS-SIAM Joint Summer Research Conference on Quantum Graphs and Their Applications, June 19-23, 2005, Snowbird, Utah*, volume 415, page 1. American Mathematical Soc., 2006.

[192] Michael Aizenman, Robert Sims, and Simone Warzel. Absolutely continuous spectra of quantum tree graphs with weak disorder. *Communications in mathematical physics*, 264:371–389, 2006.

[193] Michael Aizenman, Robert Sims, and Simone Warzel. Stability of the absolutely continuous spectrum of random schrödinger operators on tree graphs. *Probability theory and related fields*, 136:363–394, 2006.

[194] Pavel Exner, Mario Helm, and Peter Stollmann. Localization on a quantum graph with a random potential on the edges. *Reviews in Mathematical Physics*, 19(09):923–939, 2007.

[195] Peter D Hislop and Olaf Post**. Anderson localization for radial tree-like random quantum graphs. *Waves in Random and Complex Media*, 19(2):216–261, 2009.

[196] G. Tanner. From quantum graphs to quantum random walks. In *Non-Linear Dynamics and Fundamental Interactions*, pages 69–87. Springer, 2006.

[197] Julia Kempe. Quantum random walks: an introductory overview. *Contemporary Physics*, 44(4):307–327, 2003.

[198] B. Hein and G. Tanner. Wave communication across regular lattices. *Physical Review Letters*, 103(26):260501, 2009.

[199] S. Gnutzmann and U. Smilansky. Quantum graphs: Applications to quantum chaos and universal spectral statistics. *Advances in Physics*, 55(5-6):527–625, 2006.

[200] Uzy Smilansky. Discrete graphs–a paradigm model for quantum chaos. In *Chaos*, pages 97–124. Springer, 2013.

[201] Michał Ławniczak, Oleh Hul, Szymon Bauch, Petr Seba, and Leszek Sirko. Experimental and numerical investigation of the reflection coefficient and the distributions of wigner's reaction matrix for irregular graphs with absorption. *Physical Review E*, 77(5):056210, 2008.

[202] Michał Ławniczak, Szymon Bauch, Oleh Hul, and Leszek Sirko. Experimental investigation of microwave networks simulating quantum chaotic systems: the role of direct processes. *Physica Scripta*, 2012(T147):014018, 2012.

[203] Oleh Hul, Szymon Bauch, Prot Pakoński, Nazar Savytskyy, Karol Życzkowski, and Leszek Sirko. Experimental simulation of quantum graphs by microwave networks. *Physical Review E*, 69(5):056205, 2004.

[204] Vasundhara Gadiyaram, Smitha Vishveshwara, and Saraswathi Vishveshwara. From quantum chemistry to networks in biology: a graph spectral approach to protein structure analyses. *Journal of Chemical Information and Modeling*, 59(5):1715–1727, 2019.

[205] N Kannan and S Vishveshwara. Identification of side-chain clusters in protein structures by a graph spectral method. *Journal of molecular biology*, 292(2):441–464, 1999.

[206] J Stanley Griffith. A free-electron theory of conjugated molecules. part 1.—polycyclic hydrocarbons. *Transactions of the Faraday Society*, 49:345–351, 1953.

[207] Pavel Exner. Bound states of infinite curved polymer chains. *Letters in Mathematical Physics*, 57(2):87–96, 2001.

[208] Delio Mugnolo. Gaussian estimates for a heat equation on a network. *arXiv preprint arXiv:1005.2070*, 2010.

[209] Natalie E Sheils and David A Smith. Heat equation on a network using the fokas method. *Journal of Physics A: Mathematical and Theoretical*, 48(33):335001, 2015.

[210] Pavel Exner, Milos Tater, and D Vaněk. A single-mode quantum transport

in serial-structure geometric scatterers. *Journal of Mathematical Physics*, 42(9):4050–4078, 2001.

[211] Peter Kuchment. Quantum graphs: II. some spectral properties of quantum and combinatorial graphs. *Journal of Physics A: Mathematical and General*, 38(22):4887–4900, may 2005.

[212] Bérangère Delourme, Sonia Fliss, Patrick Joly, and Elizaveta Vasilevskaya. Trapped modes in thin and infinite ladder like domains. part 1: existence results. *Asymptotic analysis*, 103(3):103–134, 2017.

[213] B. Heinand G. Tanner. Wave communication across regular lattices. *Physical review letters*, 103(26):260501, 2009.

[214] Bérangère Delourme and Sonia Fliss. Guided modes in a hexagonal periodic graph like domain. *arXiv preprint arXiv:2309.02023*, 2023.

[215] Alex Figotin and Peter Kuchment. Spectral properties of classical waves in high-contrast periodic media. *SIAM Journal on Applied Mathematics*, 58(2):683–702, 1998.

[216] Wally Axmann, Peter Kuchment, and Leonid Kunyansky. Asymptotic methods for thin high-contrast two-dimensional pbg materials. *Journal of Lightwave Technology*, 17(11):1996, 1999.

[217] Claudio Amovilli, Frederik E Leys, and Norman H March. Electronic energy spectrum of two-dimensional solids and a chain of c atoms from a quantum network model. *Journal of mathematical chemistry*, 36:93–112, 2004.

[218] Marzieh Baradaran and Pavel Exner. Cairo lattice with time-reversal non-invariant vertex couplings. *Journal of Physics A: Mathematical and Theoretical*, 2023.

[219] Peter Kuchment and Leonid Kunyansky. Differential operators on graphs and photonic crystals. *Advances in Computational Mathematics*, 16:263–290, 2002.

[220] Alex Figotin and Peter Kuchment. Band-gap structure of spectra of periodic dielectric and acoustic media. i. scalar model. *SIAM Journal on Applied Mathematics*, 56(1):68–88, 1996.

[221] Peter Kuchment and Olaf Post. On the spectra of carbon nano-structures. *arXiv preprint math-ph/0612021*, 2006.

[222] JE Avron, P Exner, and Y Last. Periodic schrödinger operators with large gaps and wannier-stark ladders. *Physical review letters*, 72(6):896, 1994.

[223] Jeffrey H Schenker and Michael Aizenman. The creation of spectral gaps by graph decoration. *Letters in Mathematical Physics*, 53:253–262, 2000.

[224] Pavel Exner, Shu Nakamura, and Yukihide Tadano. Continuum limit of the lattice quantum graph hamiltonian. *Letters in Mathematical Physics*, 112(4), aug 2022.

[225] Shu Nakamura and Yukihide Tadano. On a continuum limit of discrete schrödinger operators on square lattice. *Journal of Spectral Theory*, 11(1):355–367, 2021.

[226] Georgi S Medvedev. The nonlinear heat equation on dense graphs and graph limits. *SIAM Journal on Mathematical Analysis*, 46(4):2743–2766, 2014.

[227] T. Kottos and U. Smilansky. Quantum chaos on graphs. *Physical Review Letters*, 79:4794–4797, 1997.

[228] T. Kottos and U. Smilansky. Chaotic scattering on graphs. *Physical review letters*, 85(5):968, 2000.

[229] F. Barra and P. Gaspard. Transport and dynamics on open quantum graphs. *Phys. Rev. E*, 65:016205, Dec 2001.

[230] Tristan Lawrie, Sven Gnutzmann, and Gregor Tanner. Closed form expressions for the green's function of a quantum graph—a scattering approach. *Journal of Physics A: Mathematical and Theoretical*, 56(47):475202, 2023.

[231] Alexandre G M Schmidt, Bin Kang Cheng, and M G E da Luz. Green function approach for general quantum graphs. *Journal of Physics A: Mathematical and General*, 36(42):L545–L551, oct 2003.

[232] Yshai Avishai and Jean-Marc Luck. Quantum percolation and ballistic conductance on a lattice of wires. *Physical Review B*, 45(3):1074, 1992.

[233] RV Craster, Tryfon Antonakakis, Maria Makwana, and Sébastien Guenneau. Dangers of using the edges of the brillouin zone. *Physical Review B—Condensed Matter and Materials Physics*, 86(11):115130, 2012.

[234] Michael Renardy and Robert C Rogers. Distributions. *An Introduction to Partial Differential Equations*, pages 122–173, 2004.

[235] Eleftherios N Economou. *Green's functions in quantum physics*, volume 7. Springer Science & Business Media, 2006.

[236] Fabiano M. Andrade, A.G.M. Schmidt, E. Vicentini, B.K. Cheng, and M.G.E. da Luz. Green's function approach for quantum graphs: An overview. *Physics Reports*, 647:1–46, 2016.

[237] Fabiano M. Andrade and Simone Severini. Unitary equivalence between the green's function and schrödinger approaches for quantum graphs. *Physical Review A*, 98:062107, Dec 2018.

[238] Alison A. Silva, Fabiano M. Andrade, and Dionisio Bazeia. Average scattering entropy of quantum graphs. *Physical Review A*, 103:062208, Jun 2021.

[239] Eric J. Heller. Bound-state eigenfunctions of classically chaotic hamiltonian systems: Scars of periodic orbits. *Phys. Rev. Lett.*, 53:1515–1518, Oct 1984.

[240] Holger Schanz and Tsampikos Kottos. Scars on quantum networks ignore the lyapunov exponent. *Phys. Rev. Lett.*, 90:234101, Jun 2003.

[241] Sven Gnutzmann, Holger Schanz, and Uzy Smilansky. Topological resonances in scattering on networks (graphs). *Phys. Rev. Lett.*, 110:094101, Feb 2013.

[242] Yves Colin de Verdière and Françoise Truc. Topological resonances on quantum graphs. *Annales Henri Poincaré*, 19(5):1419–1438, 2018.

[243] Bertrand Georgeot and Richard E Prange. Exact and quasiclassical fredholm solutions of quantum billiards. *Physical review letters*, 74(15):2851, 1995.

[244] AA Maradudin, Paul Mazur, EW Montroll, and GH Weiss. Remarks on the vibrations of diatomic lattices. *Reviews of Modern Physics*, 30(1):175, 1958.

[245] AA Maradudin. Some effects of point defects on the vibrations of crystal lattices. *Reports on Progress in Physics*, 28(1):331, 1965.

[246] M Lawrence Glasser and I John Zucker. Extended watson integrals for the cubic lattices. *Proceedings of the National Academy of Sciences*, 74(5):1800–1801, 1977.

[247] Per-Gunnar Martinsson and Gregory J Rodin. Asymptotic expansions of lattice green's functions. *Proceedings of the Royal Society of London. Series A: Mathematical, Physical and Engineering Sciences*, 458(2027):2609–2622, 2002.

[248] CM Linton. The green's function for the two-dimensional helmholtz equation in periodic domains. *Journal of Engineering Mathematics*, 33:377–401, 1998.

[249] SK Chin, NA Nicorovici, and RC McPhedran. Green's function and lattice sums for electromagnetic scattering by a square array of cylinders. *Physical Review E*, 49(5):4590, 1994.

[250] AB Movchan, NA Nicorovici, and RC McPhedran. Green's tensors and lattice sums for electrostatics and elastodynamics. *Proceedings of the Royal Society of London. Series A: Mathematical, Physical and Engineering Sciences*, 453(1958):643–662, 1997.

[251] David Kapanadze. Exterior diffraction problems for two-dimensional square lattice. *Zeitschrift für angewandte Mathematik und Physik*, 69:1–17, 2018.

[252] Paul A Martin. Discrete scattering theory: Green's function for a square lattice. *Wave motion*, 43(7):619–629, 2006.

[253] Tristan Lawrie, Gregor Tanner, and Dimitrios Chronopoulos. A quantum graph approach to metamaterial design. *Scientific Reports*, 12(1):18006, 2022.

[254] TM Lawrie, TA Starkey, G Tanner, DB Moore, P Savage, and GJ Chaplain. Application of quantum graph theory to metamaterial design: Negative refraction of acoustic waveguide modes. *arXiv preprint arXiv:2409.07133*, 2024.

[255] Zixian Liang and Jensen Li. Extreme acoustic metamaterial by coiling up space. *Phys. Rev. Lett.*, 108:114301, Mar 2012.

[256] Antonin Coutant, Li-Yang Zheng, Vassos Achilleos, Olivier Richoux, Georgios Theocharis, and Vincent Pagneux. Topologically invisible defects in chiral mirror lattices. *Advanced Physics Research*, page 2300102, 2023.

[257] M. Born E. Wolf. *Principles of optics: electromagnetic theory of propagation, interference and diffraction of light*. Oxford, Pergamon Press, 1964.

[258] COMSOL Multiphysics® v. 6.2. *www.comsol.com/www.comsol.com/*. COMSOL AB, Stockholm, Sweden.

[259] Yangbo Xie, Adam Konneker, Bogdan-Ioan Popa, and Steven A Cummer. Tapered labyrinthine acoustic metamaterials for broadband impedance matching. *Applied Physics Letters*, 103(20), 2013.

[260] Pavel Exner and Petr Seba. Bound states in curved quantum waveguides. *Journal of Mathematical Physics*, 30(11):2574–2580, 1989.

[261] Noé Jiménez, Jean-Philippe Groby, and Vicent Romero-García. The transfer matrix method in acoustics: Modelling one-dimensional acoustic systems, phononic crystals and acoustic metamaterials. *Acoustic Waves in Periodic Structures, Metamaterials, and Porous Media: From Fundamentals to Industrial Applications*, pages 103–164, 2021.

[262] D. B. Moore, J. R. Sambles, A. P. Hibbins, T. A. Starkey, and G. J. Chaplain. Acoustic surface modes on metasurfaces with embedded next-nearest-neighbor coupling. *Phys. Rev. B*, 107:144110, Apr 2023.

[263] Gregory J Chaplain and Richard V Craster. Surface corrugated laminates as elastic grating couplers: Splitting of sv-and p-waves by selective diffraction. *Journal of Applied Physics*, 129(4), 2021.

[264] Chen Shen, Yangbo Xie, Ni Sui, Wenqi Wang, Steven A Cummer, and Yun Jing. Broadband acoustic hyperbolic metamaterial. *Physical review letters*, 115(25):254301, 2015.

[265] Simon Yves, Emanuele Galiffi, Xiang Ni, Enrico Maria Renzi, and Andrea Alù. Twist-induced hyperbolic shear metasurfaces. *arXiv preprint arXiv:2306.01775*, 2023.

[266] Farzad Zangeneth-Nejad, Dimitrios L. Sounas, Andrea Alù, and Fleury Romain. Analogue computing with metamaterials. *Nature Reviews Materials*, 6:207–225, 2021.

[267] L Wesemann, T Davis, and A Roberts. Meta-optical and thin film devices for all-optical information processing. *Applied Phytsics Reviews*, 8:031309, 2021.

[268] Alexandre Silva, Francesco Monticone, Giuseppe Castaldi, Vincenzo Galdi, Andrea Alù, and Nader Engheta. Performing mathematical operations with metamaterials. *Science*, 343:160–163, 2014.

[269] William P Wardley, Johannes W Goessling, and Martin Lopez-Garcia. Measuring photonics in photosynthesis: Combined micro-fourier image spectroscopy and pulse amplitude modulated chlorophyll fluorimetry at the micrometre-scale. *Biomimetics*, 7(3):107, 2022.

[270] Zhao Yu-Qian, Gui Wei-Hua, Chen Zhen-Cheng, Tang Jing-Tian, and Li Ling-Yun. Medical images edge detection based on mathematical morphology. In *2005 IEEE engineering in medicine and biology 27th annual conference*, pages 6492–6495. IEEE, 2006.

[271] R.J. Holyer and S.H. Peckinpaugh. Edge detection applied to satellite imagery of the oceans. *IEEE Transactions on Geoscience and Remote Sensing*, 27(1):46–56, 1989.

[272] Mamta Mittal, Amit Verma, Iqbaldeep Kaur, Bhavneet Kaur, Meenakshi Sharma, Lalit Mohan Goyal, Sudipta Roy, and Tai-Hoon Kim. An efficient edge detection approach to provide better edge connectivity for image analysis. *IEEE Access*, 7:33240–33255, 2019.

[273] Abdulhakam.AM. Assidiq, Othman O. Khalifa, Md. Rafiqul Islam, and Sheroz Khan. Real time lane detection for autonomous vehicles. In *2008 International Conference on Computer and Communication Engineering*, pages 82–88, 2008.

[274] John Canny. A computational approach to edge detection. *IEEE Transactions on Pattern Analysis and Machine Intelligence*, PAMI-8(6):679–698, 1986.

[275] L Brillouin. *Wave Propagation and Group Velocity*. Academic Press, New York, 1960.

[276] Yi Chen, Muamer Kadic, and Martin Wegener. Roton-like acoustical dispersion relations in 3d metamaterials. *Nature communications*, 12(1):3278, 2021.

[277] TM Lawrie, G Tanner, and GJ Chaplain. Engineering metamaterial interface scattering coefficients via quantum graph theory. *Acta Physica Polonica: A*, 144(6), 2023.

[278] Rafael C Gonzalez. *Digital image processing*. Pearson education india, 2009.